Ion implantation for figure correction of high-resolution x-ray telescope mirrors

By
Brandon D. Chalifoux

B.S. Mechanical Engineering
Rice University, 2008

Submitted to the Department of Mechanical Engineering
in partial fulfillment of the requirements for the degree of

Master of Science in Mechanical Engineering
at the
MASSACHUSETTS INSTITUTE OF TECHNOLOGY

September 2014

Signature redacted

Signature of Author.....
Department of Mechanical Engineering
August 22, 2014

Signature redacted

Certified by.....
Mark L. Schattenburg
Senior Research Scientist
Kavli Institute for Astrophysics and Space Research
Thesis Supervisor

Signature redacted

Accepted by.....
David E. Hardt
Professor of Mechanical Engineering
Chairman, Departmental Committee on Graduate Students

Ion implantation for figure correction of high-resolution x-ray telescope mirrors

by

Brandon D. Chalifoux

Submitted to the Department of Mechanical Engineering
On August 22nd, 2014, in partial fulfillment of the requirements for the degree of
Master of Science in Mechanical Engineering

Abstract

Fabricating mirrors for future high-resolution, large-aperture x-ray telescopes continues to challenge the x-ray astronomy instrumentation community. Building a large-aperture telescope requires thin, lightweight mirrors; due to the very low stiffness of thin mirrors, these are difficult to fabricate, coat, and mount, while achieving and maintaining the required surface figure accuracy. Ion implantation offers a potential solution for fabricating high-accuracy mirrors, by providing capability for fine figure correction of mirror substrates.

Ion implantation causes local sub-surface stress that is a function of ion fluence, which results in changes in curvature. In principle, implanting to cause the right amount of stress in the right locations on a substrate would allow correction of figure errors in the substrate. In addition, x-ray telescope mirrors must be mechanically stable over decades, and have low surface roughness. In this work, high-energy (150 keV – 1.5 MeV) ions were implanted into silicon and glass substrates, and the implications on figure correction, surface roughness, and surface figure stability studied.

Changes in curvature resulting from sub-surface stress were measured, to understand the magnitude of stress that can be applied, and the dependence of stress on ion fluence. Figure corrections of flat silicon substrates were made. To investigate effects on surface roughness, x-ray reflectivity studies were conducted on implanted samples. Stability in surface figure was studied using thermal cycling, and measurements after 1 year of storage. Finally, simulations were conducted for correction of conical substrates similar to what would be used in future x-ray observatories. The results presented in this work suggest that ion implantation is indeed a feasible method of figure correction of mirrors for high-resolution, large-aperture x-ray telescopes.

Acknowledgments

This work represents the enormous efforts of many people; in sum, orders of magnitude more important than my own. I am grateful to all of these people for their support, encouragement, and interest in me and my work. My adviser, Mark Schattenburg, provided continuous encouragement to try dumb ideas and make mistakes, while showing an unwavering commitment to my education. This is, of course, in addition to generating the idea to use ion implantation for this application in the first place! Ralf Heilmann provided valuable advice, encouragement, and learning opportunities. My other colleagues in the Space Nanotechnology Laboratory, Ed Sung, Dong Guan, Jay Fucetola, Alex Bruccoleri, and Martin Klingensmith provided valuable input for many aspects of this project. At MIT PSFC, the efforts of Dr. Graham Wright have been invaluable for developing experiments for *in-situ* curvature measurements, and I look forward to further collaboration.

Many members of the x-ray astronomy instrumentation community have provided valuable input, for which I am grateful. In particular, I'd like to acknowledge the input of Dr. Will Zhang, Dr. Steve O'Dell, Dr. Kai-Wing Chan, and many others at NASA Marshall Space Flight Center and NASA Goddard Space Flight Center. In addition, the funding that made this work possible was generously provided by NASA APRA grants NNX10AF59G and NNX14AE76G, as well as the MIT Kavli Institute Research Investment Fund, and the NSF Graduate Research Fellowship Program.

All of the faculty and staff I have worked with at MIT have been fantastic. I would like to highlight the efforts of: Mark Belanger in the Edgerton student shop; Bill Buckley and Gerry Wentworth in the LMP machine shop; Scott Speakman in the CMSE X-ray Diffraction SEF; and all of the MTL staff. I would also like to acknowledge the efforts of Brian Doherty and Mike Kroko at CuttingEdge Ions, LLC., for providing high-quality service and for patiently educating me about ion implantation equipment.

My family and friends deserve far more credit for this work than I; without their tireless efforts, I would not be where I am. There are too many people who have made life-changing impacts to name in even ten pages. My parents and grandparents, in particular, have always put the needs of me and my siblings above their own. My fiancée, Helen, has helped me be a person far better than I would be otherwise. Saben Murray, Mr. and Mrs. Murray, and Dan Trager, have provided more support and encouragement than anyone could believe.

Contents

Abstract 3

Acknowledgments 5

Contents 7

1 Introduction 13

1.1 Purpose 13

1.2 X-ray observatories: state of the art 13

1.3 X-ray mirror technology 15

1.3.1 Glass slumping 17

1.3.2 Reflective layer 19

1.3.3 Other figure correction techniques 20

2 Irradiation-induced Stress 21

2.1 Introduction 21

2.2 High energy ion-solid interactions 21

2.3 Ex-situ measurement of irradiation-induced stress 22

2.4 In-situ measurements 28

2.5 Irradiation-induced stress in silicon 30

2.5.1 Maximum integrated stress 31

2.5.2 Critical fluence for amorphization 34

2.6 Irradiation-induced stress in glass and silica 35

2.7 Design of in-situ curvature measurement device 37

2.7.1 Functional requirements 37

2.7.2 Optical design 39

2.7.3 Image processing and curvature calculation 40

2.7.4 Measurement of beam divergence angle 41

3 Figure correction of flat substrates 43

3.1 Introduction 43

3.2 Spherical curvature correction 43

3.3 Higher-order figure correction 47

3.3.1 Modeling 48

3.3.2 Masking process 51

3.3.3 Results 54
4 Roughness and relaxation studies of implanted substrates 55
4.1 Introduction *55*
4.2 Roughening of implanted substrates *55*
4.2.1 Background 56
4.2.2 Experimental procedure 57
4.2.3 Results 57
4.2.4 Conclusions regarding surface roughness 60
4.3 Stability of implanted glass and silicon substrates *60*
4.3.1 Thermal cycle testing of glass 61
4.3.2 Temporal relaxation measurements 63
4.4 Conclusions and future work *65*
5 Numerical studies of thin segmented x-ray telescope mirrors 67
5.1 Introduction *67*
5.2 Methodology *68*
5.2.1 Mirror geometry 68
5.2.2 Finite element model 70
5.2.3 Control script 72
5.2.4 Consideration of Legendre polynomial test functions 73
5.3 Results *74*
6 Conclusions and future work 79
Appendix A MATLAB/ADINA code for figure correction of flat substrates 81
A.1 ADINA substrate input batch file: SiDisk.in *81*
A.2 ADINA temperature input batch file: SiDiskTemps.in (abbreviated) *83*
A.3 MATLAB script: controlscript.m *83*
A.4 MATLAB function: ADINA_Init.m *86*
A.5 MATLAB function: ADINA_run.m *87*
A.6 MATLAB function: gen_tBatch.m *87*
Appendix B: MATLAB/ADINA code for figure correction of near-conical substrates 89
B.1 ADINA substrate input batch file: SiDisk.in *89*
B.2 MATLAB script: controlscript.m (abbreviated) *93*
B.3 Matlab script: FindLeastSquaresFit.m (abbreviated) *95*

Appendix C: LabView diagrams for *in-situ* curvature measurement device 97

C.1 LabView main front panel: Initialization *97*

C.2 LabView main front panel: Experimental Data *98*

References 99

Table of Figures

Figure 1.1 Wolter I telescope design illustration of the Chandra Observatory. Image from [1]. 14
Figure 1.2 With current technology, there is a tradeoff between effective area and angular resolution. The goal of this work is to achieve high resolution *and* large effective area, while keeping costs low. Image from [4]. 15
Figure 1.3 NuSTAR mirror assembly, consisting of ~10,000 slumped glass conical mirror segments with multilayer coatings. Images from [11]. 16
Figure 1.4 Module concept for large x-ray observatory optics assembly. Many mirror segments are assembled into a module and accurately co-aligned. The modules are then combined into a full optic assembly and again co-aligned. Images from [4]. 17
Figure 2.1 Illustration of the effect of implantation on flat substrate curvature. The pink layer represents the implanted ions. The pre-implant substrate is behind in light blue; the post-implant substrate is in purple in front. The change in curvature is greatly exaggerated here, for clarity. This example shows compressive stress; tensile stress would cause bending toward the ion beam. 23
Figure 2.2 Shack Hartmann Surface Metrology Tool (SHSMT) used for measuring substrates for ex-situ measurements. The tool measures the reflected wavefront from a surface using a lenslet array and CCD camera. Images from [22]. 25
Figure 2.3 Stress-Fluence for 150 keV Si+ implanted into silicon substrates. The stress falls off after a fluence of 8x 10^{15} ions/cm^2, at a maximum integrated stress of about 50 N/m. This stress is compressive. 26
Figure 2.4 Stress-Fluence for 150 keV Si+ and Al+ implanted into Schott D-263 glass substrates. The stress falls off after a fluence of 6x10^{14} ions/cm^2 at a maximum integrated stress of about 15 N/m. This stress is tensile. 27
Figure 2.5 Stress-Fluence for 150 keV Si+ and Ar+ implanted into BK-7 glass substrates. There is no obvious trend here, suggesting that BK-7 glass may not exhibit significant stress from ion implantation. 27
Figure 2.6 *In-situ* curvature measurement tool, based on [30]. A laser beam is split into 5 parallel beams, and reflected off of the sample to a camera. The spacing between beam centroids yields a measurement of curvature. 29
Figure 2.7 *In-situ* stress measurement results for silicon implanted into silicon. This stress is compressive. 30
Figure 2.8 Normalized nuclear damage distribution for 2 MeV Xe^+ (as used in [29]) and 150 keV Si^+ (as used in Section 2.3) implanted into silicon, calculated using SRIM. The damage thickness, δ, is shown as a dashed line for 2 MeV Xe^+, illustrating the physical interpretation of this measure. $E_{nuc,max}$ is shown as a black dot. 33
Figure 2.9 Maximum integrated stress plotted against damage thickness (Equation 2.3). Data from Chalifoux 2014 will be discussed in Section 2.4. 34
Figure 2.10 Fluence at which peak integrated stress occurs, as a function of ion mass 35
Figure 2.11 *In-situ* curvature measurement device, mounted on vacuum chamber of ion implanter. The laser and optics are shown at center, the window of the sample chamber is shown on the right, and the camera is on the left. 38
Figure 2.12 Optical design of in-situ curvature measurement device used in this thesis. The focal plane of Lens 1 is located distance δ left of the diffraction grating, which is in turn a distance f_2 to the left of Lens 2. The beam waist is imaged onto the CCD plane, and the centroids of these beams may be tracked using software. See Figure 2.6 for the experimental setup, which includes the sample. 39
Figure 2.13 Image of focal spots on CCD. The centroids of these spots are tracked throughout the experiment. 40
Figure 2.14 Experimental setup to measure beam divergence angle. The lens tube to the left emits 5 nearly-parallel beams. The camera is set up on the right, 835 mm away, and moved on a track ± 22.5 mm toward and away from the laser. 41
Figure 2.15 Results of parallelism measurement experiment, showing a divergence angle of ε = 0.736 mrad. 42

Figure 3.1 Surface maps of a corrected sample. The spherical curvature was reduced from 9 μm to -0.7 μm; a correction factor of 1.10. The residual surface error is primarily due to astigmatism and higher-order errors. 45
Figure 3.2 A histogram of the curvature before and after correction, showing that significant correction occurred. $\kappa pre = 0.0046\,m - 1$; $\kappa post = -0.0006\,m - 1 \pm 0.0013\,m - 1$ 45
Figure 3.3 A histogram of the curvature correction factor, an indication of the effectiveness of the spherical curvature correction process, shows that the process mean is 25% too high, but does follow a normal distribution. $C\kappa = 1.23$; $SC\kappa = 0.24$ 46
Figure 3.4 Change in shape of a silicon wafer after attempted astigmatism correction, showing a small change in figure but almost purely astigmatism. 48
Figure 3.5 Stress-response library. A test function is applied as a stress distribution (left columns), and this results in a shape change (right columns). Both the test functions and resulting shape change may be described well by Zernike polynomials, shown as stem plots next to the functions. 49
Figure 3.6 Finding the stress distribution that results in the best-fit figure involves solving a least-squares problem to fit the Zernike coefficients from the Stress-Response Library to the Zernike coefficients of the desired shape change. 50
Figure 3.7 Stress distribution required for astigmatism correction of a particular sample. High stress areas, in this case, are near the edges, while the center requires little stress. 51
Figure 3.8 A photomask is used to pattern photoresist spun on the substrate surface, in order to implant a non-uniform fluence distribution over the surface of the substrate. This allows correction of higher-order figure errors 53
Figure 4.1 Measurement of an X-ray reflectivity curve requires measuring grazing-incidence specular reflection of a sample, by moving both the source and detector each by θ. 57
Figure 4.2 X-ray reflectivity data and models for pre- and post-implant silicon wafer. The fluence was 2 x 10^{15} ions/cm^2, the implanted species was Si^+ 150 keV, and the beam current was 60 μA. 59
Figure 4.3 X-ray reflectivity data and models for pre- and post-implant D-263 wafer. The fluence was 2 x 10^{14} ions/cm^2, the implanted species was Si^+ 150 keV, and the beam current was 60 μA. 59
Figure 4.4 Illustration of sample temperature throughout thermal cycling experiments. Samples were measured after each thermal cycle to monitor changes in curvature. 62
Figure 4.5 Change in integrated stress after each bake cycle. The repeatability of the metrology is approximately 1 N/m. 62
Figure 4.6 Histogram of relaxation data for silicon and D-263 glass substrates, measured after 1 year. $\Delta S = 0.4\ \mathrm{N/m}$; $\sigma S = 2.2\ \mathrm{N/m}$, after excluding the 3 extreme outliers. 64
Figure 5.1 Important dimensions of mirror model. 69
Figure 5.2 Example of a mesh used in the finite element model. R = 200 mm in this image. 71
Figure 5.3 Plot of an influence function resulting from a 1 N/m stress applied at a single node. Also shown are the three constraints and the directions of translations that are constrained. 72
Figure 5.4 Desired change in figure for all simulations in this chapter. This is a sum of three Legendre polynomials. 73
Figure 5.5 Stress required to correct the figure shown in Figure 5.4, while keeping the maximum stress below 150 N/m. This is for a substrate radius of 200 mm 74
Figure 5.6 Residual slope error for a substrate with a radius of 200 mm and a stress limit of 150 N/m. The errors are concentrated at the edges. 75
Figure 5.7 Residual estimated HPD error for different substrate radii and different stress limits. The small radius of 200 mm is most difficult to correct 76
Figure 5.8 HPD reduction factor for different substrate radii and different stress limits. 77

1 Introduction

1.1 Purpose

The purpose of this thesis is to evaluate whether sub-surface stress arising from ion implantation is a plausible method of figure correction of thin x-ray telescope mirrors. Fabrication of high-resolution *and* lightweight x-ray telescope optics is a challenge that has eluded solution for decades, and there is considerable effort currently being expended to solve this problem. Ion implantation may be a plausible method of fine figure correction of thin optics, because high energy ions implanted into a substrate cause structural changes that result in near-surface stress and substrate bending. Figure errors can be corrected since ion implantation allows precise control of the magnitude and position of the stress. In short, the data in this thesis demonstrate that ion implantation is indeed a plausible method of figure correction in thin optics.

1.2 X-ray observatories: state of the art

Developing a high-resolution, large-aperture x-ray observatory is challenging because x-rays are strongly attenuated by most materials, including Earth's atmosphere; thus, x-ray observatories must be located outside the Earth's atmosphere, and reflective (rather than refractive) optics must be used.

A common optical design of modern x-ray telescopes is the Wolter I configuration, shown in Figure 1.1 [1]. X-rays from a celestial source enter the telescope, reflect off of a parabolic surface, then a hyperbolic surface, to a detector at the image plane. For x-rays, reflectivity is high only for very large angles of incidence (alternatively, small grazing angles). Typical grazing angles are ~1-2° for soft x-ray telescopes. In order to increase reflectivity at higher grazing angles, a reflective coating is applied to the mirror surface; for soft x-rays (<5 keV) this is typically a high-density material such as iridium, gold, etc.; for harder x-rays, multilayer coatings are used.

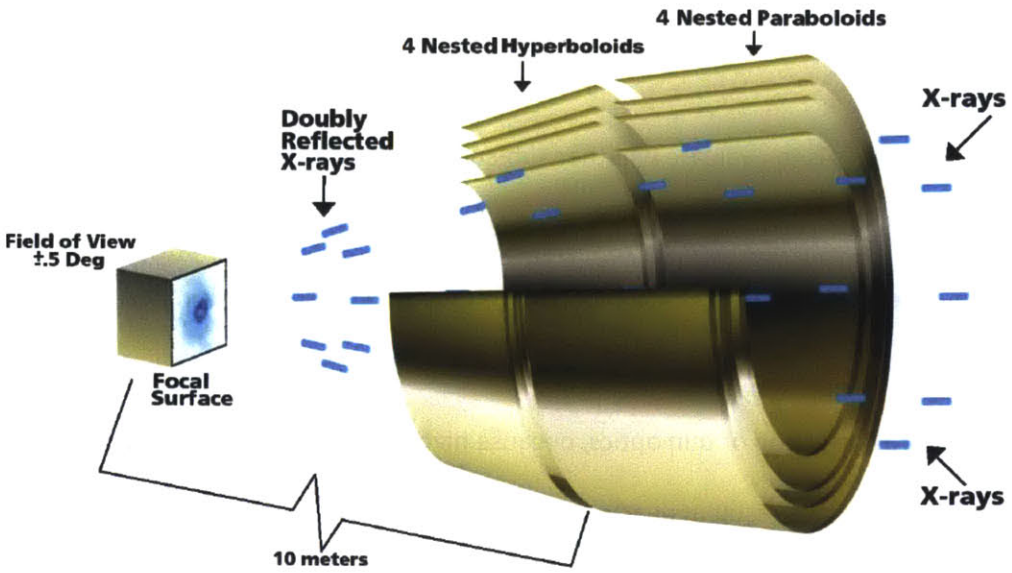

Figure 1.1 Wolter I telescope design illustration of the Chandra Observatory. Image from [1].

Since the grazing angle is small, the effective area is on the order of 1% of the actual mirror surface area. This presents manufacturing challenges. The Chandra Observatory [2], launched in 1999, utilized four monolithic mirror shells made from Zerodur®, a low thermal expansion glass ceramic. Each shell includes both parabolic and hyperbolic surfaces, and is approximately 25 mm thick. The shells were bored from solid ingots, ground to shape, and painstakingly polished by hand. The angular resolution of the Chandra observatory is better than 0.5 arc-second half-power diameter (HPD). Comparing this to prior and recent observatories, it is clear that Chandra's angular resolution is truly incredible. However, the cost of the mirrors was extremely high, estimated by [3] at $9.8 billion (2013 dollars) per square meter of effective area (A_{eff} = 800 cm^2 at 1 keV). For high-resolution telescopes with larger effective area, the fabrication processes used for Chandra are not feasible.

There has always been a tradeoff between high angular resolution, cost, and effective area. Figure 1.2 [4], demonstrates this tradeoff. The goal driving the present work is to generate technology to change the terms of this tradeoff; to build a telescope with high angular resolution, large effective area, and low cost.

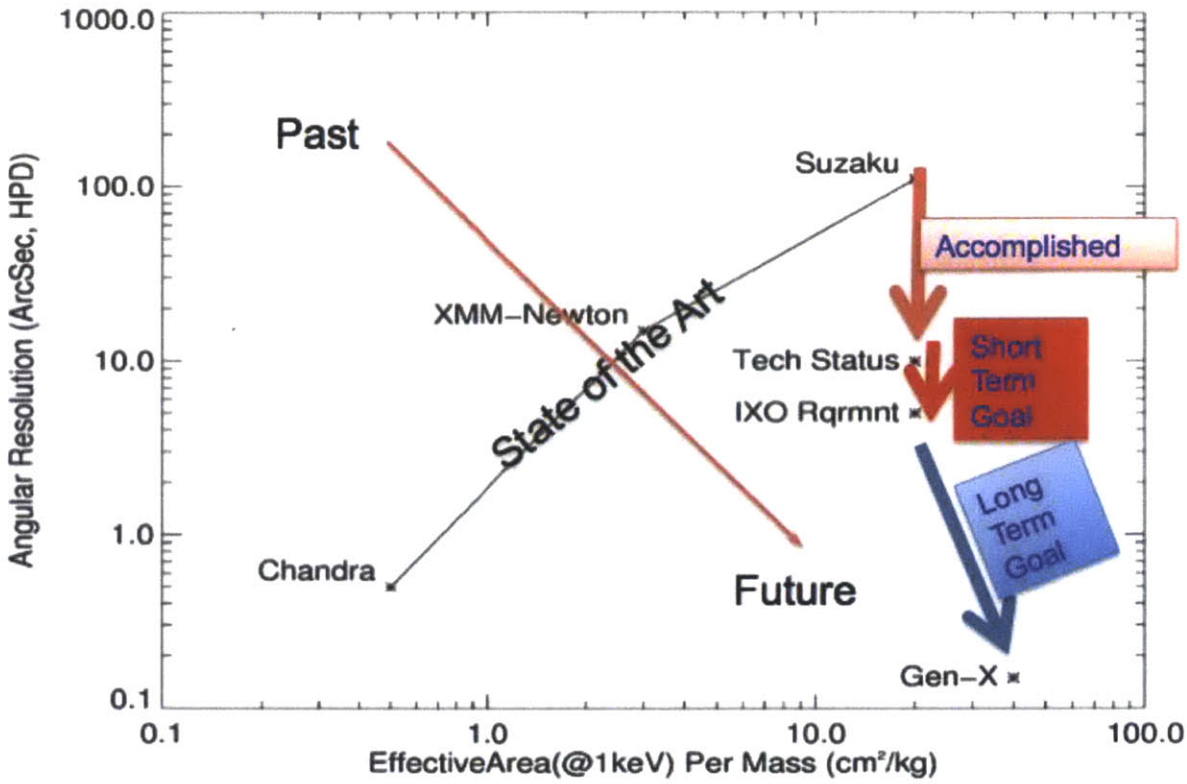

Figure 1.2 With current technology, there is a tradeoff between effective area and angular resolution. The goal of this work is to achieve high resolution *and* large effective area, while keeping costs low. Image from [4].

1.3 X-ray mirror technology

Developing a high-resolution x-ray telescope using thin optics is quite a challenge due to the very low stiffness of thin substrates. Grinding and polishing, as often used for shaping thick optics such as those used in the Chandra Observatory, cannot be used effectively on thin optics because the forces applied to the substrates introduce excessive deformation and errors. Novel methods of substrate fabrication must therefore be devised. Beyond substrate fabrication, thin substrates are strongly affected by the application of thin (~20 nm) stressed reflective layers. Mounting thin substrates is also challenging because even small forces cause significant deformation. For example, gravity sag may cause significant distortion in thin substrates, which then changes once in space.

There are primarily three fabrication technologies that have made significant progress toward high-resolution x-ray telescope optics: electroless nickel-cobalt replication [5]; silicon pore optics [6]; and

slumped glass [7][4]. Single-crystal silicon [8] may also be a viable substrate material. The Space Nanotechnology Laboratory (SNL) at MIT has focused on non-contact slumping of flat substrates [9][10], which will soon be extended to the fabrication of Wolter I-type mirror substrates.

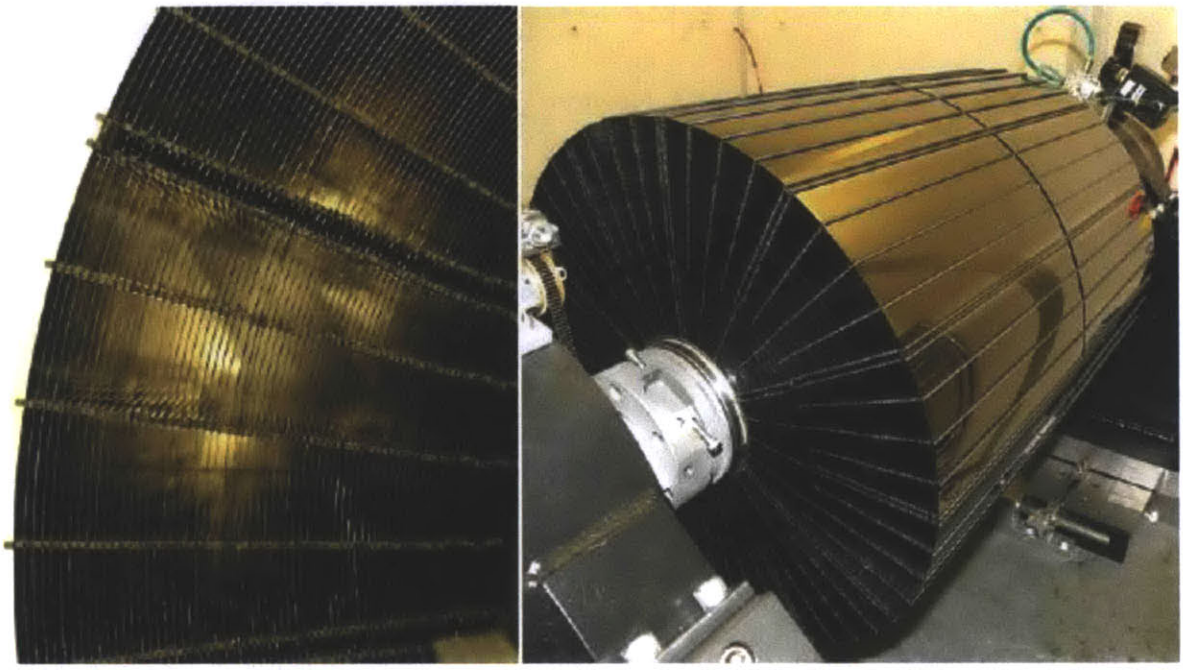

Figure 1.3 NuSTAR mirror assembly, consisting of ~10,000 slumped glass conical mirror segments with multilayer coatings. Images from [11].

One other important distinction between different technologies is whether mirror shells are each composed of a single element (such as in Figure 1.1), or azimuthal segments (such as in Figure 1.3). Full-shell mirrors are significantly stiffer than segmented mirrors, and require far fewer components that must be aligned. For large telescopes, however, full-shell mirrors are difficult to implement due to the large size of the mandrels required, and the amount of surface area that requires extremely precise polishing. Segmented mirrors, while much more challenging to coat, align, and mount without introducing unacceptable distortion, are a manageable size for large telescopes. A large telescope would consist of many modules of many carefully co-aligned mirror segments; the modules would then be carefully aligned to each other. Figure 1.4 [4] illustrates this concept. The technologies applicable to

segmented mirrors are Silicon Pore Optics, slumped glass, and single-crystal silicon mirrors. Ion implantation is best suited to segmented mirrors rather than to full-shell mirrors, and particularly to slumped glass and single-crystal silicon mirrors.

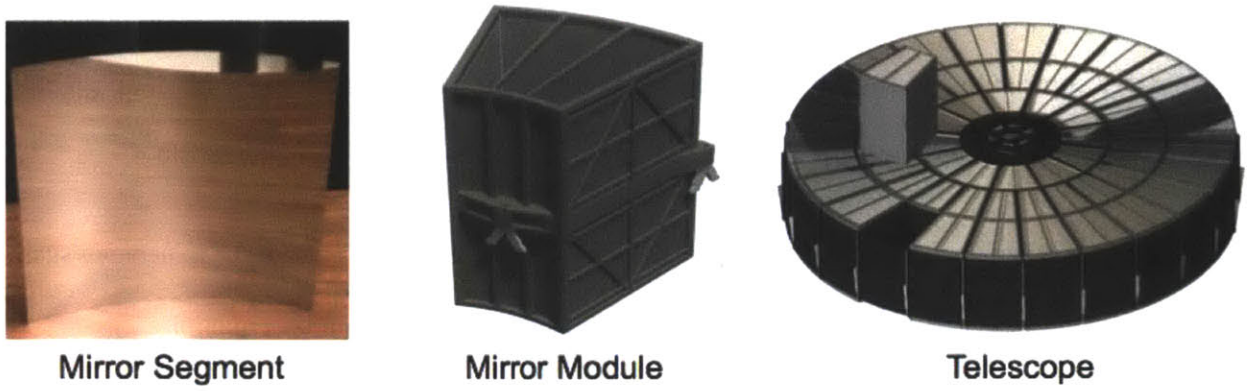

Figure 1.4 Module concept for large x-ray observatory optics assembly. Many mirror segments are assembled into a module and accurately co-aligned. The modules are then combined into a full optic assembly and again co-aligned. Images from [4].

There are three challenges that face all of these technologies: substrate fabrication, reflective layer coating, and mounting and alignment. One strategy is to fabricate substrates as accurately as possible, and to minimize the errors introduced by the other two processes. The work of this thesis concerns figure correction of thin slumped glass or silicon substrates, either before or after coating with a reflective layer, but likely before mounting.

1.3.1 Glass slumping

In glass slumping, a thin glass substrate is placed on a mandrel and heated to the softening point of the glass. The glass softens, and conforms to the mandrel, replicating its shape, and solidifies upon cooling. A release layer is required between the glass and the mandrel to avoid fusing the two. In contact slumping, this release layer is a powder [4] or thin film [12], and gravity is used to force the softened glass to replicate the mandrel. In non-contact slumping, a thin film of air is used instead of a release layer. This air film allows replication of the mandrel figure but prevents particulates from introducing mid spatial frequency errors in the glass, which is originally free of such errors. This distinction is

important for figure correction since low spatial frequency (figure) errors have lower curvature, so require less stress to correct.

Contact slumping

Zhang, et al. [13] have achieved impressive results with contact slumping, demonstrating mirrors with an estimated contribution to the half-power diameter (HPD) of the point spread function of only 6 arc seconds. These mirrors are the most accurate thin segmented optics currently demonstrated.

Contact glass slumping has a number of important drawbacks, however. First, in order to achieve such results, it was necessary to employ a 50 hour cooling cycle [12]. This is required to minimize temperature gradients in the glass and quartz mandrel as the glass solidifies; temperature gradients cause curl-up of the glass and replication errors due to the large difference in coefficients of thermal expansion between the glass and quartz mandrel. The second drawback is the requirement for a release layer, which introduces mid spatial-frequency errors in the glass. Without a release layer, the glass fuses to the quartz. A thin layer of Boron Nitride powder is applied to the quartz mandrels, which allows the glass to be removed after slumping. Unfortunately, the Boron Nitride tends to clump rather than remain as a uniform layer. This clumping, in addition to any dust particles on the mandrel before or after application of the release layer, causes the glass to exhibit dimples.

Non-contact slumping

Non-contact slumping replaces the release layer in contact slumping with a thin film of air ~5-50 μm thick. This both prevents sticking between the glass and mandrel, and avoids any mid-spatial frequency errors. Akilian [14], Husseini [15], and Sung [16] discuss this in detail. While non-contact slumping may not replicate the figure of the mandrel as well as contact slumping, due to non-uniform pressure in the air film, low-spatial frequency errors are easier to both measure and correct than higher-spatial

frequency errors. The goal with non-contact slumping at SNL is to achieve sufficient figure replication of mandrels without introducing mid- or high-spatial frequency errors; and to follow the slumping with figure correction using ion implantation.

1.3.2 Reflective layer

A reflective coating must be applied to mirror substrates to improve their x-ray reflectivity. Materials with high atomic numbers are preferred because they have a high electron density, which increases the reflectivity at higher grazing angles. With higher grazing angles, the telescope point-spread function is less sensitive to mirror figure errors, and less mirror area must be fabricated to achieve a given effective collecting area.

Iridium is an effective reflective layer for soft x-rays, and was employed in the Chandra Observatory [2], and is currently being investigated to coat thin substrates, with a film thickness of ~15 nm [17]. Even with such thin layers, stress is a significant concern. For harder x-rays (> 10 keV), multilayer coatings are necessary to provide sufficient reflectivity for a telescope. Multilayer coatings, such as those used in the NuSTAR observatory [18], have substantial intrinsic stress, which would unacceptably distort high-accuracy mirrors. Currently, thin optics for high-resolution x-ray telescopes are expected to have single-material coatings.

Since high energy ions penetrate the first tens of nanometers of substrate without many nuclear collisions with substrate atoms, it may be possible to perform figure correction after a coating layer has been applied, thus allowing correction of coating-induced figure errors. This application has not been investigated in this thesis.

1.3.3 Other figure correction techniques

One method of achieving high-accuracy thin substrates is to apply corrections after slumping or other fabrication methods, using actuators. O'Dell, et al. [19] describes several methods of thin optic adjustment currently under development. Given the tight space requirements, all methods use surface-parallel actuation, which changes the local curvature of the substrate. There are three primary methods, aside from ion implantation, currently under development: piezo-electric actuators, magneto-strictive actuators, and a differential deposition method.

The present work is concerned with using ion implantation as a method of figure correction, which has several significant advantages over other methods. First, no actuators are used on the mirrors, eliminating the need to have wires routed to tens of thousands of actuators. Second, no films are added to the mirrors, which would have intrinsic stress that then requires further correction. Third, ion implantation allows correction of both positive and negative curvature, by implanting on the front and back of the substrate.

2 Irradiation-induced Stress

2.1 Introduction

This chapter describes the stress induced by ion implantation, and how this may be applicable to figure correction. It is important to understand the magnitude and direction of the stress that can be imparted on a substrate, as well as the fluence required to achieve that stress. Fluence is defined as the number of implanted ions per unit area of the substrate. For all stress data in this chapter, negative stress is compressive and positive stress is tensile. The effect of a negative (compressive) stress is illustrated in Figure 2.1.

In order to extend the results of this chapter to process conditions not studied here, it is important to understand the effects that give rise to the stress generation. The data presented here has been compared with data from the literature, based on the 'damage thickness' (see Section 2.5.1), which suggests a way of increasing the maximum magnitude of integrated stress.

2.2 High energy ion-solid interactions

As energetic ions penetrate the surface of a substrate, they interact with the substrate atoms' electrons and nuclei. While the ion speed is high, the probability of having a nuclear collision with a substrate atom is small because of a shielding effect – the electrons of the substrate atoms shield their nuclei from the ions. Thus, when the ion initially enters the substrate, it loses energy primarily through electronic stopping, where the substrate electrons effectively apply a drag to the ion. As the ion slows, its probability of interacting with substrate nuclei increases and during these collisions, if enough energy is transferred to the substrate atom, it may cause displacement of the lattice atom. The displaced atom may have an excess of energy, and may cause a cascade of interactions. The implanted ion continues to lose energy through electronic and nuclear stopping, until it finally comes to rest at some depth [20].

Due to the large number of substrate atoms, this stopping process is effectively random. After implanting a large number of ions (typically the fluence is greater than 10^{12} ions/cm^2), the depth distribution of the implanted ions will be approximately Gaussian. The mean depth is called the projected range, R_p. The standard deviation of the distribution is called the projected straggle, ΔR_p. Due to the collision cascades generated, there is some lateral straggle as well, ΔR_{perp}. The projected range depends on implanted species and energy, as well as the substrate material.

The electronic and nuclear stopping power changes with depth into the substrate; electronic stopping is dominant at shallow depths, while nuclear stopping dominates as the ion slows, at larger depths. Electronic stopping primarily results in heating of the substrate, while nuclear stopping is responsible for creating damage to the substrate. This damage is often associated with some stress-generation processes, and likewise, nuclear stopping is thought to be responsible for stress-generation in both silicon and some glasses.

The physics of ion stopping in many materials, including electronic and nuclear stopping distributions and projected ranges, is well-understood. Several analytical relations have been developed, and for many cases, Monte Carlo simulations have proven accurate. A commonly used Monte Carlo simulation software is SRIM [21], and this is used in the present work as well.

What is less well-understood, however, is the process of generating stress as a result of ion implantation. The goal of the present work is to use stress generated by ion implantation to correct the figure of flat substrates, so it is critical to be capable of generating a wide range of stress with good repeatability.

2.3 *Ex-situ* measurement of irradiation-induced stress

Initial implantation experiments in this work used commercial ion implant services because of ready availability, and because of the expertise of service providers. The goal of these experiments was to

measure the stress-fluence relation of various substrates and ion species, in order to gain some understanding of how this may be used for figure correction. The initial experiments relied on *ex-situ* metrology because performing *in-situ* measurements in a commercial implanter would be difficult, and would be inappropriate for quickly gaining a basic understanding of the process. *Ex-situ* measurements of stress were performed as follows: the wafer curvatures were first measured using the SNL Shack-Hartmann Surface Metrology Tool [22] (SHSMT), and a low-stress thin optic mounting structure [23]; the wafers were then sent to Cutting Edge Ions, LLC. to be implanted at a specified ion fluence, flux, and energy; and finally, the wafers were returned to the SNL for a second curvature measurement. The implanted substrate is illustrated in Figure 2.1, and the SHSMT is shown in Figure 2.2.

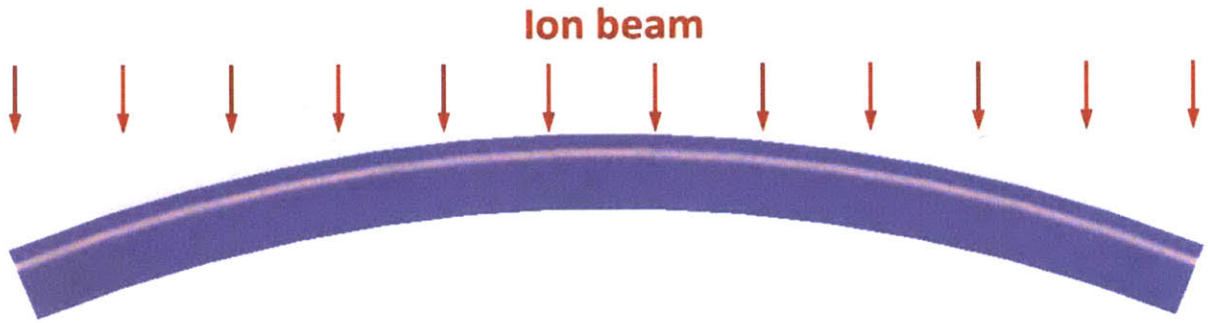

Figure 2.1 Illustration of the effect of implantation on flat substrate curvature. The pink layer represents the implanted ions. The pre-implant substrate is behind in light blue; the post-implant substrate is in purple in front. The change in curvature is greatly exaggerated here, for clarity. This example shows compressive stress; tensile stress would cause bending toward the ion beam.

Using commercial implanters adds some limitations, since the machines are designed for the integrated circuit industry, where process throughput and fluence uniformity are the key attributes of interest. Specifically, flat substrates must be used, ion energy is limited to <180 keV, and the ion fluence must be uniform. Given these limitations, flat wafers of silicon and glass were implanted with uniform fluence of various ion species, all at 150 keV ion energy and 60 μA beam current.

Integrated stress is calculated from measured changes in curvature of the implanted substrates before and after implantation. Stoney's equation is used [24], modified for plates,

$$S = \int_0^{t_i} \sigma_i(z)dz = \frac{Bh_s^2}{6}\Delta\kappa \qquad \textbf{Equation 2.1}$$

where S is the integrated stress, σ_i is the local stress (a function of depth, z) in the implanted layer, t_i is the thickness of the implanted layer, B is the biaxial elastic modulus of the substrate material[a], h_s is the thickness of the substrate, and $\Delta\kappa$ is the change in spherical curvature. The integrated stress is preferred over the local stress, because the implanted layer does not have a well-defined thickness, and the integrated stress is directly related to changes in curvature. Ultimately, changes in curvature are of interest for correcting figure errors in x-ray telescope mirrors. To give a sense of magnitudes, a stress of 1 N/m results in a P-V bow of 500 nm, on a 100 mm diameter, 400 μm thick, D-263 wafer.

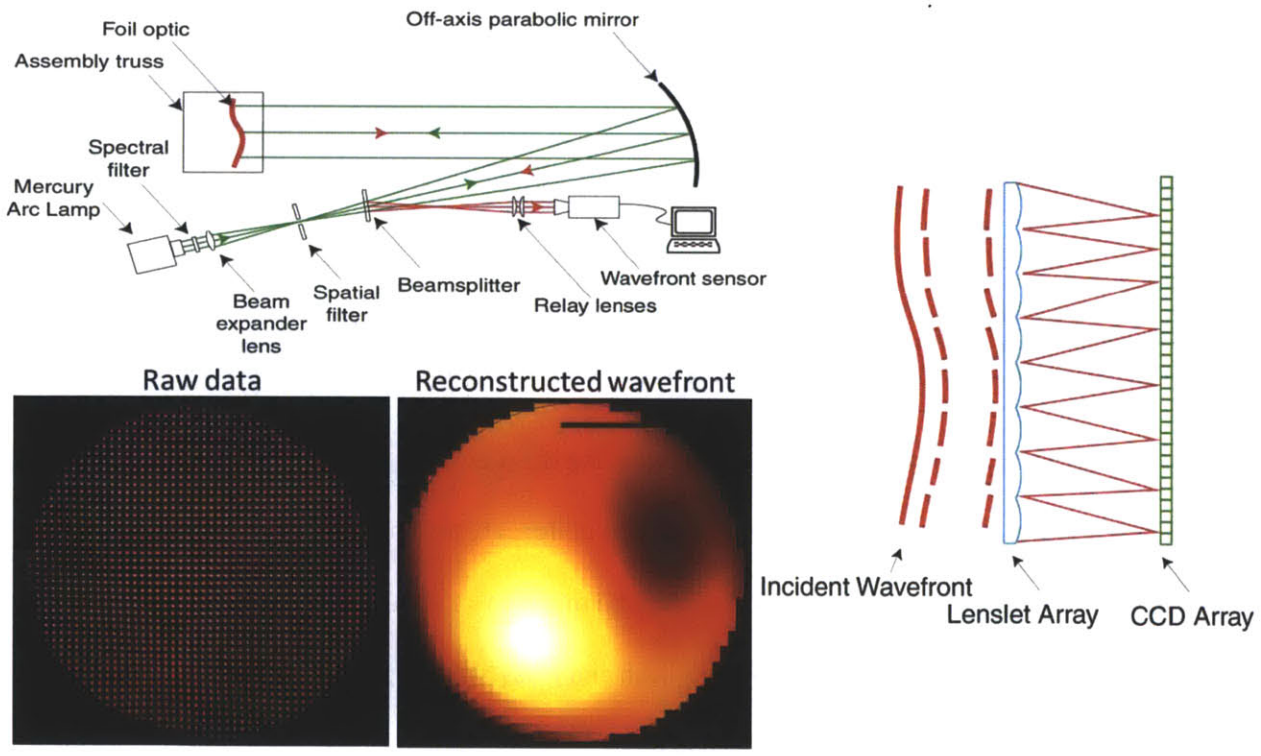

[a] Biaxial modulus for: <100> silicon substrates, B = 180.5 GPa [25]; D-263 substrates, B = 92.0 GPa [26]; and BK-7 substrates, B = 103.3 GPa [27, p. 7].

Figure 2.2 Shack Hartmann Surface Metrology Tool (SHSMT) used for measuring substrates for ex-situ measurements. The tool measures the reflected wavefront from a surface using a lenslet array and CCD camera. Images from [22].

Table 2.1 Summary of process parameters used in ion implantation experiments with *ex-situ* curvature measurements

Parameter	Value
Substrate material	<100> silicon, D-263 glass, BK-7 glass
Substrate diameter	100 mm
Substrate thickness	400 – 550 μm
Ion species	Si^+, B^+, Ar^+, Al^+
Ion energy	150 keV
Beam current	60 μA [4.75 x 10^{12} ions/cm^2sec]
Fluence	$10^{14} - 10^{16}$ ions/cm^2
Ion projected range[b]	208 nm
Ion projected straggle[1]	63 nm

Table 2.2 Summary of implanted samples used in ion implantation experiments with *ex-situ* curvature measurements

Substrate	Species	Number of samples
Silicon	Si+	36
Silicon	B+	5
BK-7	Si+	18
BK-7	Ar+	15
D-263T	Si+	24
D-263T	Al+	9
Total		107

All wafers were mounted to a 125 in^3 stainless steel block with three metal clips on the edges. No thermal control was implemented, although the ion flux was chosen to keep the surface temperature below 150 °C, based on the vendor's experience. The repeatability of the SHSMT integrated stress

[b] This value is for 150 keV Si^+ into silicon substrate, for illustration. The ion mass affects the projected range and straggle more than the difference between glass and silicon substrates. Heavier ions have lower projected range.

measurement is approximately 1 N/m over the typically week-long timeframe between the curvature measurements. Figure 2.3, Figure 2.4 and Figure 2.5 show the results of these experiments for various substrate materials and implant species. Each data point represents one sample. To maintain consistency with data from the literature, compressive stress in this thesis is positive, and tensile stress is negative. Discussion of these results is left to Section 2.5 for the silicon substrates and Section 2.6 for the glass substrates.

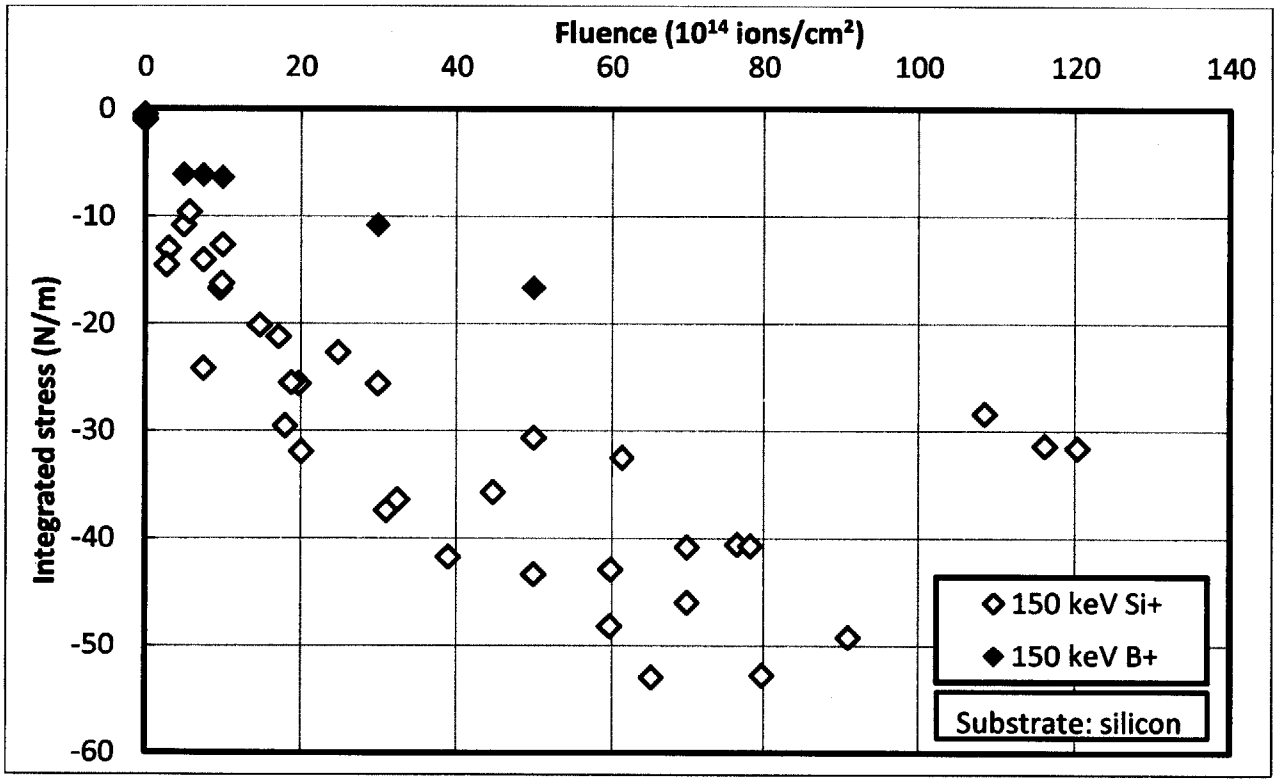

Figure 2.3 Stress-Fluence for 150 keV Si+ implanted into silicon substrates. The stress falls off after a fluence of 8x 10^{15} ions/cm^2, at a maximum integrated stress of about 50 N/m. This stress is compressive.

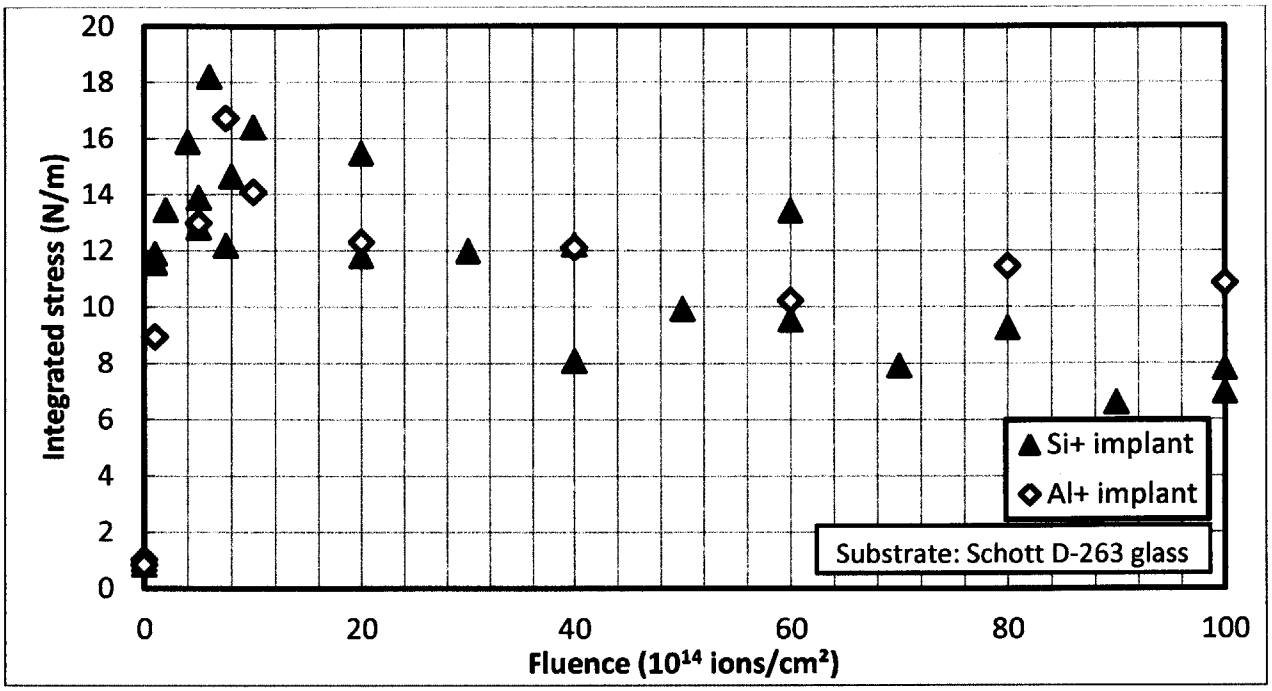

Figure 2.4 Stress-Fluence for 150 keV Si+ and Al+ implanted into Schott D-263 glass substrates. The stress falls off after a fluence of 6x10^{14} ions/cm^2 at a maximum integrated stress of about 15 N/m. This stress is tensile.

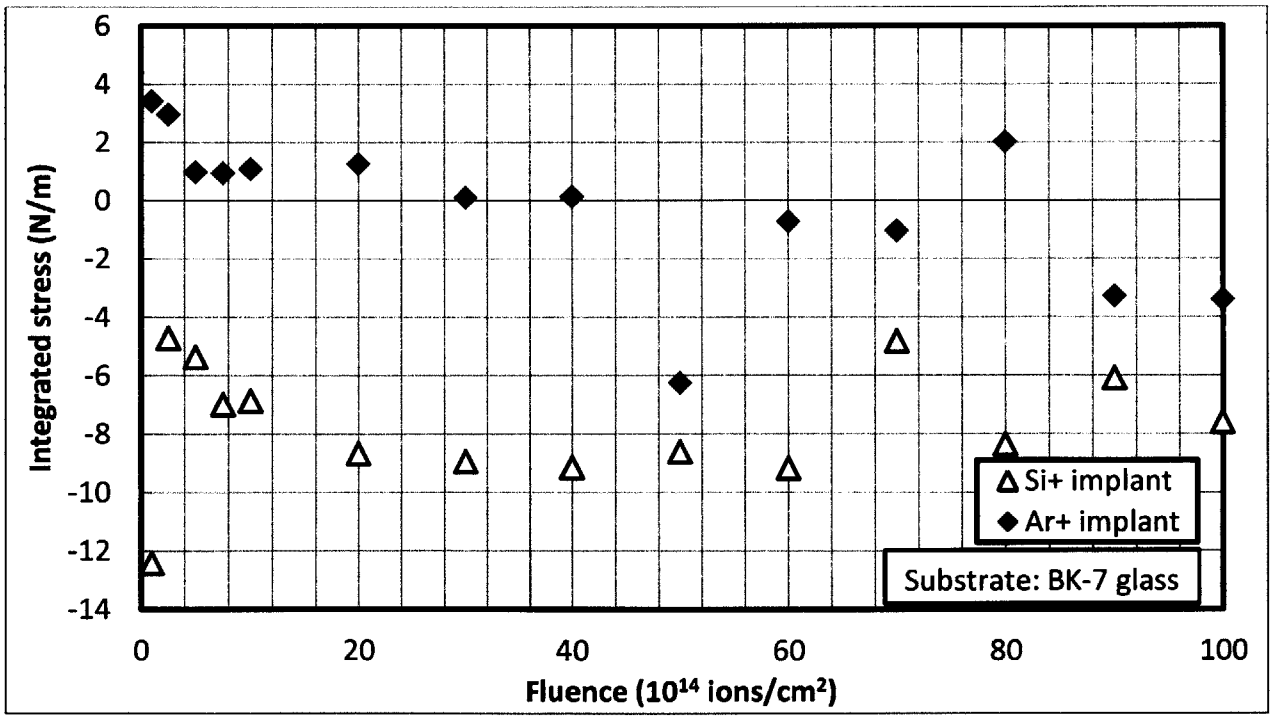

Figure 2.5 Stress-Fluence for 150 keV Si+ and Ar+ implanted into BK-7 glass substrates. There is no obvious trend here, suggesting that BK-7 glass may not exhibit significant stress from ion implantation.

2.4 *In-situ* measurements

In-situ stress measurements, where substrate curvature is measured as it is implanted, have been carried out extensively in the literature (e.g., [28][29][30]), and significantly more information may be gleaned from such experiments than from *ex-situ* measurements, at much lower cost. After experimentation with *ex-situ* measurements, we began using an on-campus ion accelerator, owned by Prof. Dennis Whyte's group in the MIT Plasma Science and Fusion Center (PSFC). This accelerator is a research-oriented tool, so developing a device to perform *in-situ* stress measurements is feasible. We developed such a device, and the details of its design are described in Section 2.7. The current section will focus on the experimental details and preliminary results.

The concept of the *in-situ* curvature measurements (from which stress may be calculated) is illustrated in Figure 2.6. This device is a variation on a system described by Floro, et al. [30]. In this system, a laser beam is split into 5 beams by a diffraction grating; these beams are then made nearly-parallel by a lens. The beams reflect off of the implanted substrate, to a CCD. The centroids of the beams are tracked, and from the measured spacing between beams, the curvature of the substrate may be calculated.

$$\Delta\kappa = \frac{D - D_i}{2L(D_i - \varepsilon L)} \qquad \textbf{Equation 2.2}$$

where $\Delta\kappa$ is the change in curvature, D is the measured average spacing between beams, D_i is the pre-implant measured average spacing between beams, L is the distance from the sample to the CCD, and ε is the divergence angle between beams impinging on the sample. The divergence angle between beams, ε, is measured in the laboratory prior to installation. This procedure is described in Section 2.7.4. From the measured change in curvature, the integrated stress may be calculated from Equation 2.1.

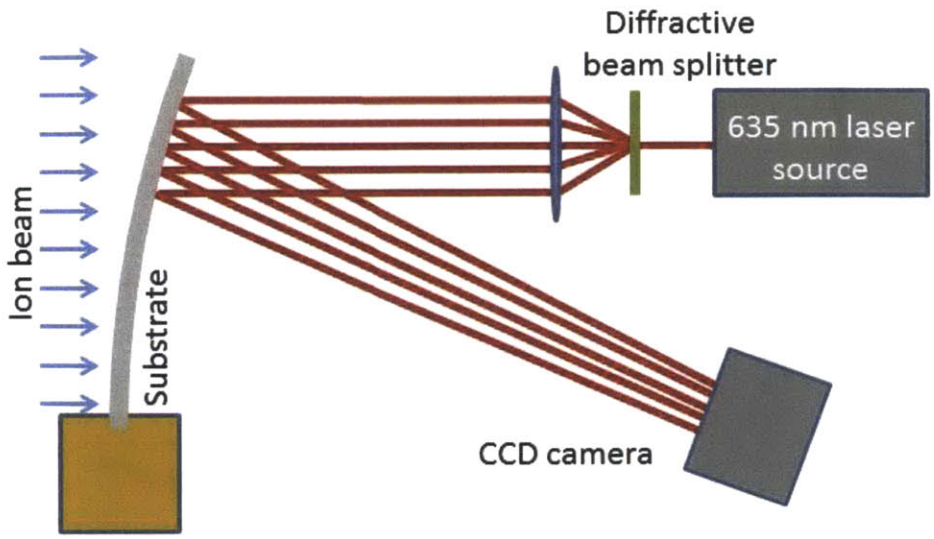

Figure 2.6 *In-situ* curvature measurement tool, based on [30]. A laser beam is split into 5 parallel beams, and reflected off of the sample to a camera. The spacing between beam centroids yields a measurement of curvature.

The initial results agree with data from the literature, as described in Section 2.5.1 and 2.5.2. An initially-increasing compressive stress is generated until a peak stress is achieved, after which the stress falls. There are several major differences between these data and the *ex-situ* measurements. First, the integrated stress is significantly higher than the *ex-situ* measurements; this is likely due to the higher ion energy used, as described in Section 2.5.1. Second, the critical fluence at which the stress reaches a maximum is significantly lower than for the *ex-situ* measurements. As shown in Section 2.5.2, the *in-situ* agrees well with data from the literature.

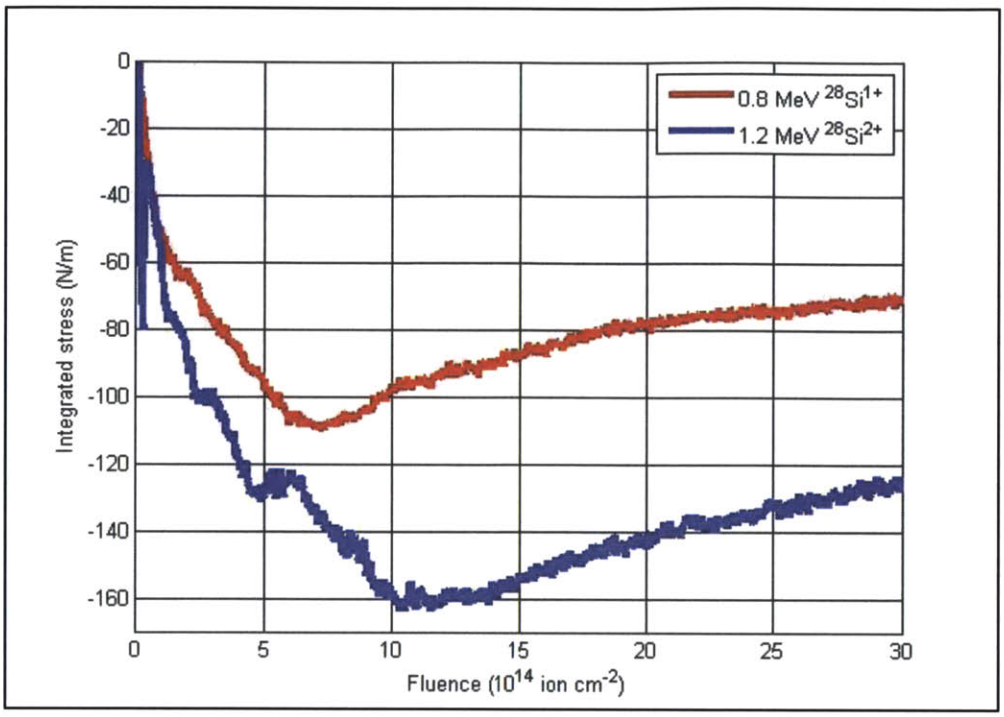

Figure 2.7 *In-situ* stress measurement results for silicon implanted into silicon. This stress is compressive.

2.5 Irradiation-induced stress in silicon

As crystalline silicon is implanted with high-energy ions, the near-surface implanted layer exhibits first an increase in compressive stress, followed by a relaxation of the implanted stress, and finally a non-zero equilibrium stress. This behavior has been demonstrated previously [29], [31]–[36]. At low fluence, the primary mechanism for irradiation-induced stress generation in crystalline silicon is damage to the crystal lattice [29]. As the lattice becomes more disordered due to nuclear collisions between the implanted ions and substrate atoms, it becomes amorphized. Since amorphous silicon is less dense than crystalline silicon, the implanted layer expands, while being restrained by the bulk of the substrate. Thus, this damaged layer exhibits a compressive stress. Once sufficient damage is imparted to cause amorphization, the stressed amorphous layer exhibits radiation-enhanced viscous flow and an anisotropic stress generation mechanism [37]. This will be further described in Section 2.6.

Similar behavior may be observed in the data shown in Figure 2.3, the *ex-situ* stress measurements. Integrated stress, always compressive, increases monotonically with increasing fluence, until saturation

at fluence of around 8 x 10^{15} ions/cm^2 and integrated stress of 50 N/m. As fluence is increased further, integrated stress appears to decrease rapidly. Beyond this similarity, there are some notable differences between this data and those available in the literature. First, the magnitude of the peak stress is higher than some other studies and lower than others (Section 2.5.1). Second, the saturation fluence is significantly higher than any other available data, and there appears to be significant variation in stress for a given fluence (Section 2.5.2).

Understanding the mechanisms that determine the stress-fluence relation, especially at low fluence, is important to guide further efforts to correct figure errors in substrates. Ideally, a large integrated stress at low fluence could be generated with good repeatability and controllability.

2.5.1 Maximum integrated stress

As crystalline silicon is implanted, the implanted ions experience nuclear collisions with the lattice atoms, causing damage to the substrate. The vast majority of this damage is self-annealed during the implant, due to local heating and the low activation energy of many defects. The damage that is not quickly annealed accumulates with increasing fluence. At a sufficiently high level of damage, there is no longer any long-range order, and the silicon is said to be amorphous. Amorphization appears to mark the upper limit on stress [29], likely because amorphous silicon experiences irradiation-enhanced viscous flow, which tends to relieve the stress.

Lattice damage is distributed unevenly, with the peak near the projected range of the ions, and falling off rapidly beyond R_p. Amorphization occurs first at the peak of the damage accumulation, and likewise this will be the first location of relaxation; increasing fluence beyond this level will only serve to decrease the integrated stress. At this fluence, the total integrated damage will define the peak integrated stress; therefore, the *breadth* of the damage distribution should be important in determining the maximum achievable integrated stress for a given ion species and energy.

To illustrate this, data from the literature may be compared on the basis of a measure of breadth of the implants' damage distributions, as calculated by SRIM. An example of some damage distributions are shown in Figure 2.8. A measure of the breadth of the damage distribution is the total damage relative to the peak damage, called here the 'damage thickness,'

$$\delta = \frac{\int_0^{t_i} E_{nuc} dz}{E_{nuc,max}} \qquad \textbf{Equation 2.3}$$

where δ (in nm) is the damage thickness; E_{nuc} (in eV/nm-ion) is the energy deposition rate into nuclear collisions, as a function of depth, z; and t_i (nm) is the thickness of the implanted layer. $E_{nuc,max}$ is shown in Figure 2.8 as a black circle, and represents the maximum rate of energy deposition into nuclear collisions. As illustrated in Figure 2.7, the compressive stress in silicon increases until reaching a maximum integrated stress, after which point it exhibits relaxation. Prior to reaching the point of maximum integrated stress, the silicon is being damaged and expanding, forming pockets of amorphous silicon. Eventually, a thin, continuous, buried amorphous layer is formed, which seems to correspond with the onset of relaxation [29], [37]. This thin amorphous layer will occur at the depth of maximum nuclear energy deposition. Thus, if the magnitude of the compressive integrated stress is related to the total integrated damage induced prior to the creation of this thin amorphous layer, then the magnitude of the compressive integrated stress should also be related to the damage thickness in Equation 2.3. The damage thickness may also be thought of as equivalent to a slab of equally-damaged silicon, with width δ and magnitude equal to the maximum nuclear energy deposition, to the of amorphization. This concept is also illustrated in Figure 2.8 as dashed lines.

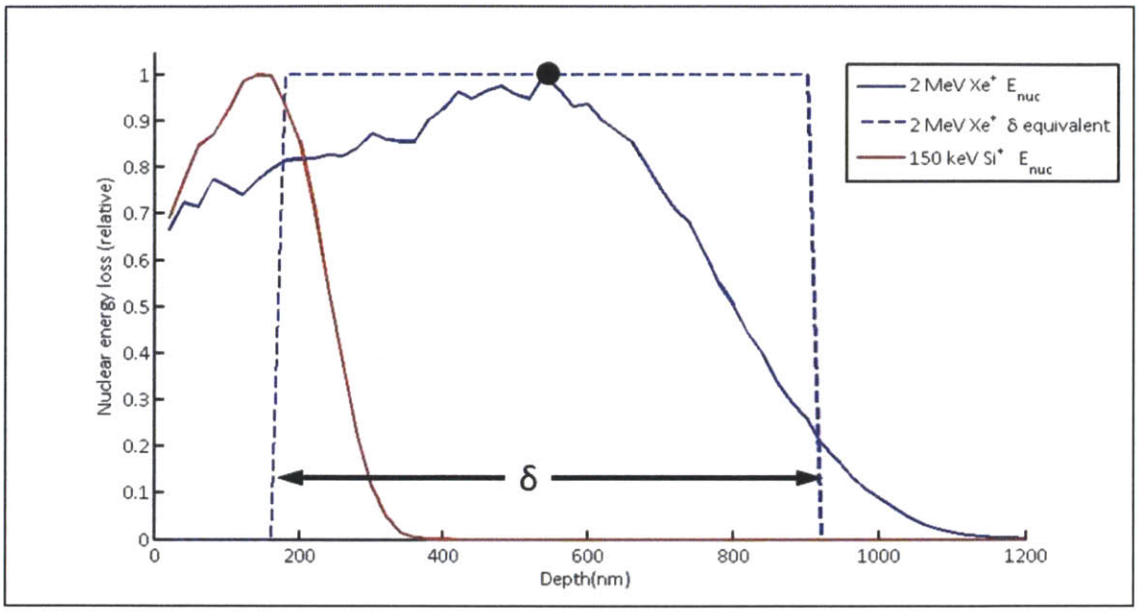

Figure 2.8 Normalized nuclear damage distribution for 2 MeV Xe^+ (as used in [29]) and 150 keV Si^+ (as used in Section 2.3) implanted into silicon, calculated using SRIM. The damage thickness, δ, is shown as a dashed line for 2 MeV Xe^+, illustrating the physical interpretation of this measure. $E_{nuc,max}$ is shown as a black dot.

The damage thickness appears to be a good predictor of maximum integrated stress in silicon. Figure 2.9 shows the maximum integrated stress as a function of damage thickness for a wide variety of implant species and energy from several sources in the literature [29], [31]–[36], as well as from this work. It is apparent that the damage thickness describes the maximum integrated stress fairly well, even though there are likely more complex contributors to stress than this simple model suggests. The effects of viscious relaxation and anisotropic stress generation mechanisms are ignored, and this may explain some of the spread in the data shown in Figure 2.9.

This suggests that an increase in maximum integrated stress may be expected from implants with a higher damage thickness. The damage thickness is typically close to the projected range; deep implants result in larger damage thickness. Thus, high energy implants should increase the maximum integrated stress, and likewise light ions should increase the maximum integrated stress. However, lighter ions require higher fluence to reach amorphization, as shown in Figure 2.10 and discussed in Section 2.5.2.

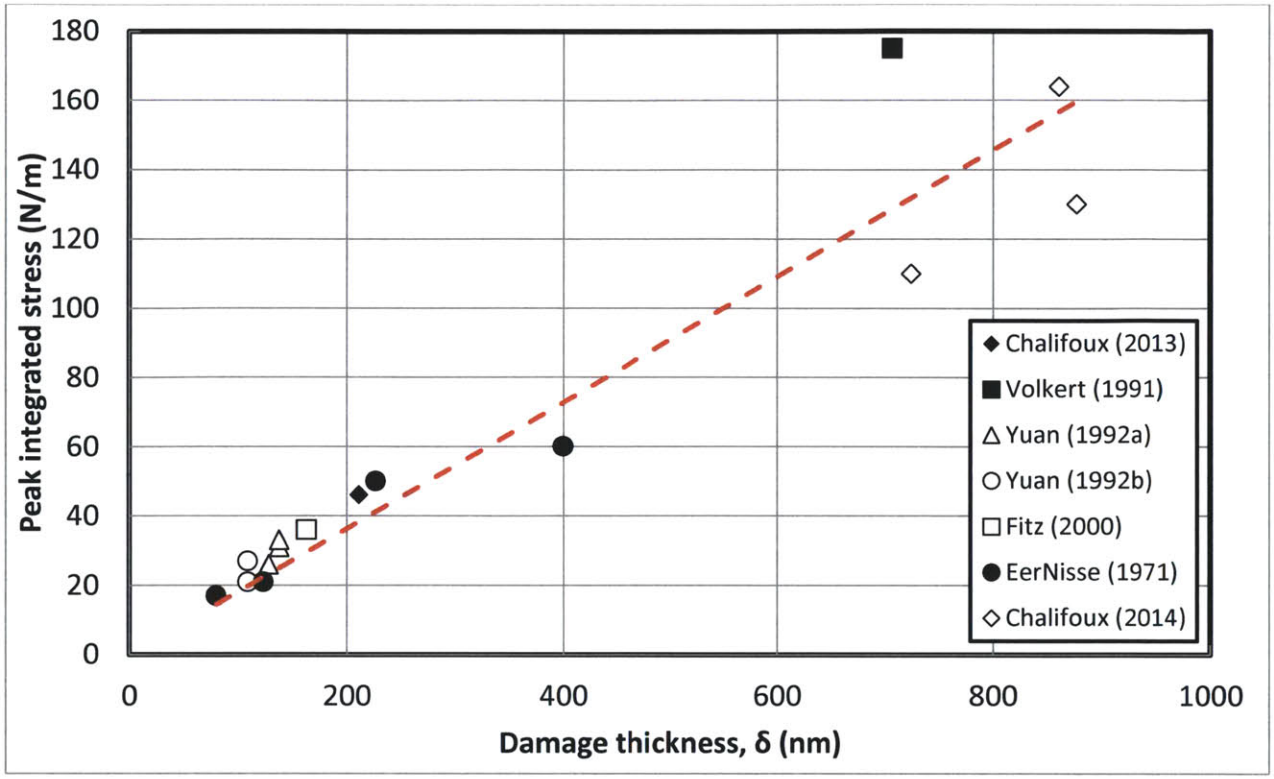

Figure 2.9 Maximum integrated stress plotted against damage thickness (Equation 2.3). Data from Chalifoux 2014 will be discussed in Section 2.4.

2.5.2 Critical fluence for amorphization

The fluence required to reach amorphization in silicon is better understood than the maximum integrated stress, because amorphization is more relevant to the manufacture of integrated circuits. There are several theories explaining why amorphization occurs and at what fluence. One early theory was proposed by Morehead and Crowder [38], and is based on the assumption that each ion generates a thermal spike and an amorphous region in a region surrounding the ion track. As the ion comes to rest, some amorphous silicon near the outside of the track recrystallizes, while the core remains amorphous. The ion mass and target temperature primarily determine the diameter of the ion track and amount of recrystallization, respectively. A higher substrate temperature requires a higher fluence to create an amorphous layer. The Morehead and Crowder (MC) model is simplistic, but it has been successful at predicting amorphization fluence.

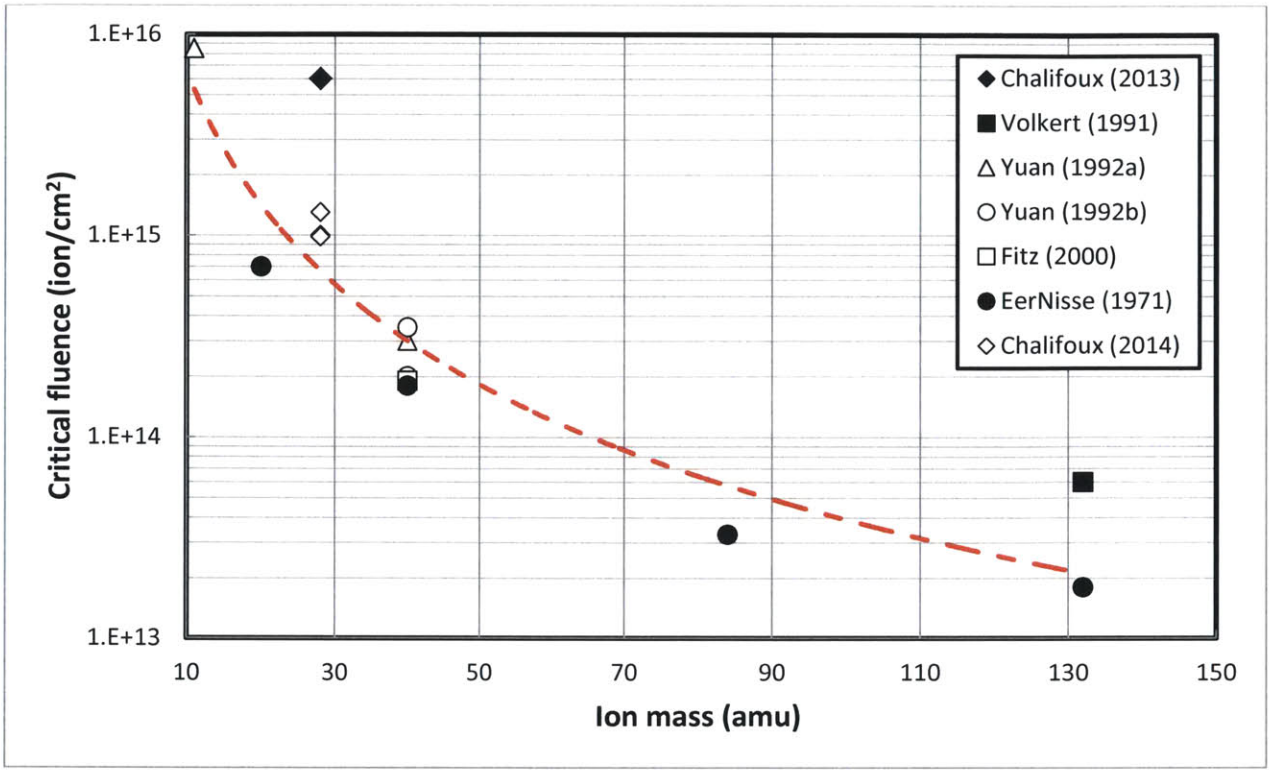

Figure 2.10 Fluence at which peak integrated stress occurs, as a function of ion mass

The MC model suggests that for light ion implants near room temperature, the amorphization fluence is very sensitive to temperature. Thus, the fact that the substrates measured *ex-situ* in the present work were not temperature-controlled and were likely near 150 °C suggests that temperature variations between samples could cause significant variability in the damage produced by a given fluence, and therefore the stress generated by a given fluence. Since ion implantation is executed in high vacuum, around 10^{-6} Torr, cooling of the substrate is through radiation and conduction only. Many factors, such as the surface condition of the mounting block or the initial bow of the wafer, could influence conductive heat transfer, which would result in different temperatures. The high implant temperature, and the low mass of Si+, may also explain the unusually-high critical fluence.

2.6 Irradiation-induced stress in glass and silica

Glass and amorphous silica differ from silicon in that they are amorphous rather than crystalline. The expansion resulting from lattice damage does not occur in glass and silica, but another mechanism is

observed: compaction [39]. At low fluence, there is a density increase in the implanted layer, resulting in a tensile stress. This mechanism saturates once a density increase of 2-3% occurs, then other mechanisms dominate, such as radiation-enhanced viscous relaxation, and an anisotropic stress generation mechanism driven by thermal spikes [40]. Radiation-enhanced viscous relaxation is a phenomenon where the substrate behaves very similarly to a fluid, with a flow proportional to the stress state and inversely proportional to a viscosity. However, the 'flow rate' is a function of ion flux rather than time, hence the term 'radiation-enhanced'. The anisotropic stress generation mechanism may arise because of thermal spikes [41], where amorphous material in the ion track is rapidly melted while surrounding material expands. When the melted material subsequently freezes and contracts, the final result is a net contraction parallel to the ion track, and expansion perpendicular to the ion track.

Glass and silica exhibit qualitatively similar behavior, with a few differences. Amorphous silica is compositionally simpler and less varied than glass, so much literature has focused on the behavior of silica under ion irradiation (e.g., [37], [39], [40]). Borosilicate glass is typically composed of primarily SiO_2, but has significant amounts of B_2O_3 and Al_2O_3, and typically either alkali (e.g., Na_2O, K_2O) or alkaline earth (e.g., CaO, MgO) components [42]. Previous researchers have studied irradiation effects on various borosilicate glasses [43], and have found that there is a strong dependence of stress on composition. The glass types of interest to x-ray telescopes are manufactured as display glass: they have very low surface roughness, are made in thin sheets, and have high stiffness-to-density ratios. One important feature is that these glasses are made with very low alkali content (e.g., 20 ppm for Schott D-263).

Since glass composition is expected to have a significant impact on the behavior under irradiation, it is important to study the specific glass being used. Schott D-263 is studied in this work because it is commonly used in slumping [4]. The *ex-situ* measurements of integrated stress as a function of fluence

of 150 keV Si+ and 150 keV Al+ is shown in Figure 2.4. Results of *in-situ* integrated stress measurements are not yet available. These *ex-situ* integrated stress measurements are qualitatively similar to those shown in the literature: an initial tensile stress followed by relaxation toward an equilibrium stress. However, the magnitude of the measured integrated stress is very low; Arnold [43] shows a maximum integrated stress of 200 N/m, while the data in Figure 2.4 shows a maximum stress less than 20 N/m. It is also clear from Figure 2.5 that BK-7 glass exhibits very little integrated stress under ion implantation.

For both D-263 and BK-7 glass, there are several possible explanations for the low magnitude of maximum integrated stress. One may be due to heating during implantation, since the thermal conductivity of glass is relatively low. Another explanation may be due to chemistry, as this has been shown to have a strong effect on stress. Yet another possible cause is the implants used here are relatively high energy using light ions, which may cause a high level of relaxation that counters any densification or other stress generation mechanisms.

2.7 Design of *in-situ* curvature measurement device

In-situ measurements of curvature allow the collection of real-time stress data, which provides a rapid and reliable method to understand the evolution of stress as a function of fluence. Data such as that shown in Figure 2.3, Figure 2.4 and Figure 2.5 may be obtained in a fraction of the time and cost as *ex-situ* measurements, allowing the exploration of many more parameters than was previously possible. *In-situ* measurement of curvature or deflection is not new, but requires access to equipment. Until recently, such equipment was not available to us, so *ex-situ* measurements were necessary; now, working with Dr. Dennis Whyte's group at MIT PFSC, we have been able to design, build, install, and test an *in-situ* curvature measurement device, based in principle on [30].

2.7.1 Functional requirements

The functional requirements of this device are listed in Table 2.3. These requirements are derived from expected magnitudes of integrated stress. The device meets all requirements. The resolution is taken as

twice the standard deviation of curvature measurements, averaged over 1-second intervals. With this averaging, the resolution is measured as 1×10^{-4} m^{-1}. With no averaging, the measured resolution is 8×10^{-4} m^{-1}. The difference is thought to be largely due to vibration.

Table 2.3 Functional requirements of curvature measurement tool

	Requirement	Achieved metric	Comments on requirement
Curvature resolution	2×10^{-4} m^{-1}	1×10^{-4} m^{-1}	Equivalent to 1 N/m for 400 μm thick silicon beam
Curvature range	± 0.07 m^{-1}	> 0.11 m^{-1}	Equivalent to ±500 N/m for 500 μm thick silicon beam
Beam spacing at CCD	< 2.5 mm	2.02 mm	Limited by available CCD sensor (8.6 mm x 6.9 mm; 11.0 mm diag.)
Mounting	8" CF flange		Flange size of existing chamber
View port diameter	1.5"		Available window diameter

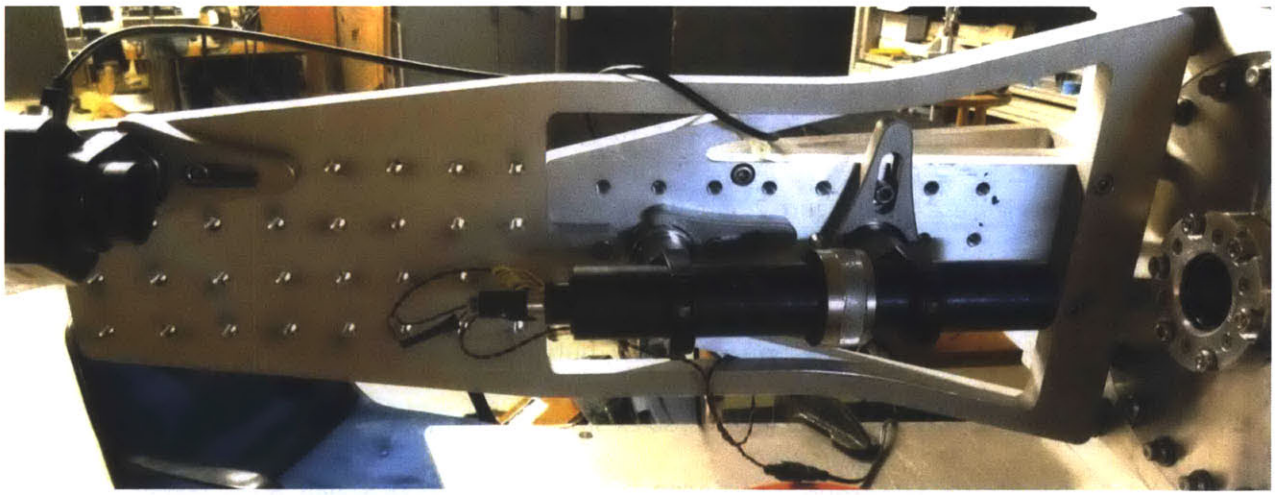

Figure 2.11 *In-situ* curvature measurement device, mounted on vacuum chamber of ion implanter. The laser and optics are shown at center, the window of the sample chamber is shown on the right, and the camera is on the left.

2.7.2 Optical design

Schematically, the experimental setup is shown in Figure 2.6. A photo of the as-built curvature measurement device is shown in Figure 2.11, and the optical design is illustrated in Figure 2.12. Important parameters of the system are listed in

Table 2.4. The diode laser (635 nm, 1 mW output) is focused by Lens 1, to a point just before the diffraction grating, such that Lens 2 will create a magnified image of the focal spot on the CCD plane. The diffraction grating is placed close to the focal plane left of Lens 2. This diffraction grating (HoloEye DE 263) has non-uniform spacing, resulting in 5 diffracted orders of nearly equal intensity and all other orders highly attenuated. These diffracted orders diverge from one another by about 25 mrad until reaching Lens 2, where they are steered to become nearly parallel. Lens 2 also serves to image the beam waist from Lens 1 onto the CCD plane, after the beams reflect off of the sample. The distance δ between the diffraction grating and the Lens 1 focal plane is determined by the distance to the CCD plane, and is adjusted using a focusing ring.

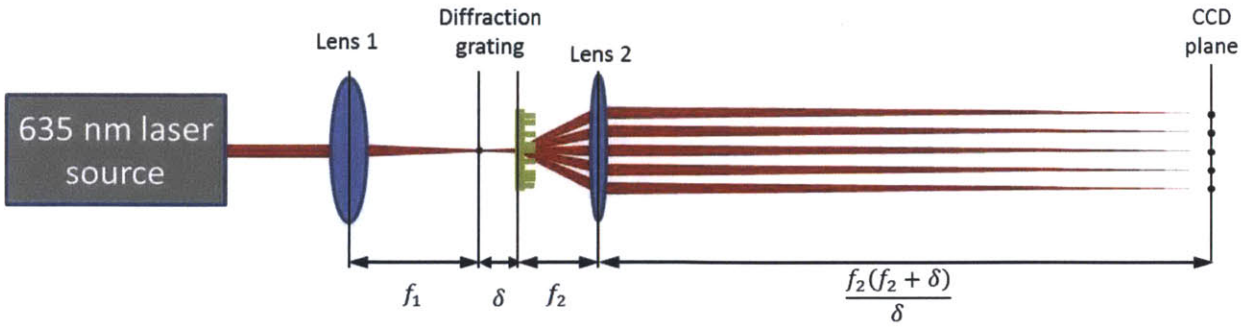

Figure 2.12 Optical design of in-situ curvature measurement device used in this thesis. The focal plane of Lens 1 is located distance δ left of the diffraction grating, which is in turn a distance f_2 to the left of Lens 2. The beam waist is imaged onto the CCD plane, and the centroids of these beams may be tracked using software. See Figure 2.6 for the experimental setup, which includes the sample.

Table 2.4 Important dimensions of as-built curvature measurement device

f_1	75 mm
f_2	50 mm
δ	2 – 5 mm
Distance, sample to CCD	665 mm
Lateral distance between beams	2.02 mm
Parallelism of beams, ε	0.736 mrad

2.7.3 Image processing and curvature calculation

Images from the camera (Sumix SMX-150-C) are captured using LabView (see Appendix C), and the centroids of each spot are calculated and tracked throughout the experiment. An example image is shown in Figure 2.13; the camera is rotated such that the focal spots span the diagonal to give sufficient sensor width.

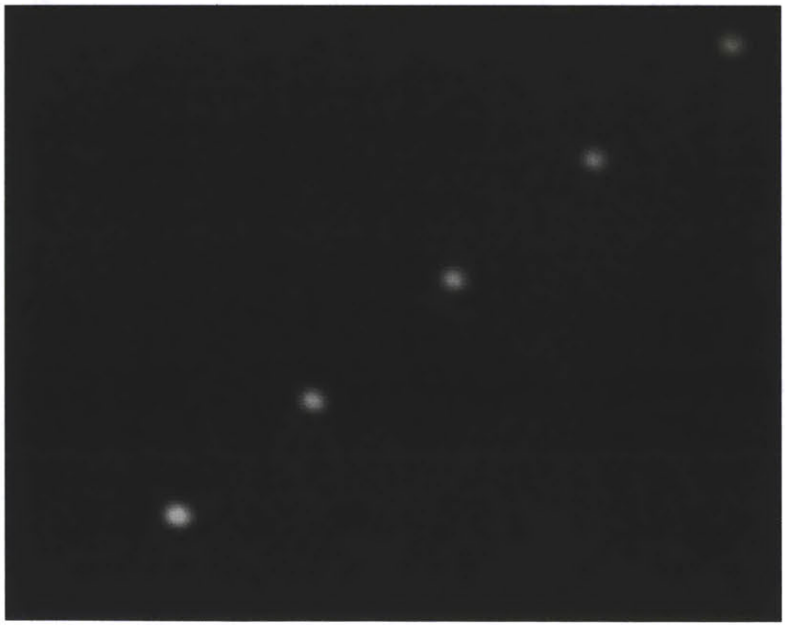

Figure 2.13 Image of focal spots on CCD. The centroids of these spots are tracked throughout the experiment.

Prior to implantation, the initial focal spot centroids are recorded and averaged, upon which all stress and curvature calculations will be based. The ion beam is then brought to the surface of the sample and

scanned, and the focal spot centroids, as well as raw images, are recorded. The curvature may be calculated from Equation 2.2, and the integrated stress may be calculated from Equation 2.1.

2.7.4 Measurement of beam divergence angle

Since the diffraction grating is not exactly a distance f_2 away from Lens 2, there is a parallelism error between adjacent beams. Beam non-parallelism has a large effect on the curvature measurement; if the divergence angle between adjacent beams is ignored, the error may be as high as 50%, as determined by Equation 2.4.

$$\frac{\Delta\kappa_{actual}}{\Delta\kappa_{\varepsilon=0}} = \frac{1}{1 - \varepsilon L/D_i} \qquad \text{Equation 2.4}$$

where κ_{actual} is the true curvature, $\kappa_{\varepsilon=0}$ is the curvature if the divergence angle, ε, is assumed to be zero, L is the distance from the sample to CCD, and D_i is the measured initial distance between beams on the CCD. With such a significant effect on the curvature measurement, it is important to measure the beam divergence angle accurately.

The experimental setup shown in Figure 2.14 was used to measure the beam divergence angle. The laser beam centroids are measured on a camera located 835 mm away from the lens tube. The camera is moved in 2.5 mm increments over a total distance of ±22.5 mm (with a position uncertainty of about 4 μm), and the focal spot centroids are averaged over 40 seconds at each position. The results of the final as-built device are shown in Figure 2.15, showing a divergence of $\varepsilon = 0.736 \pm 0.04$ mrad.

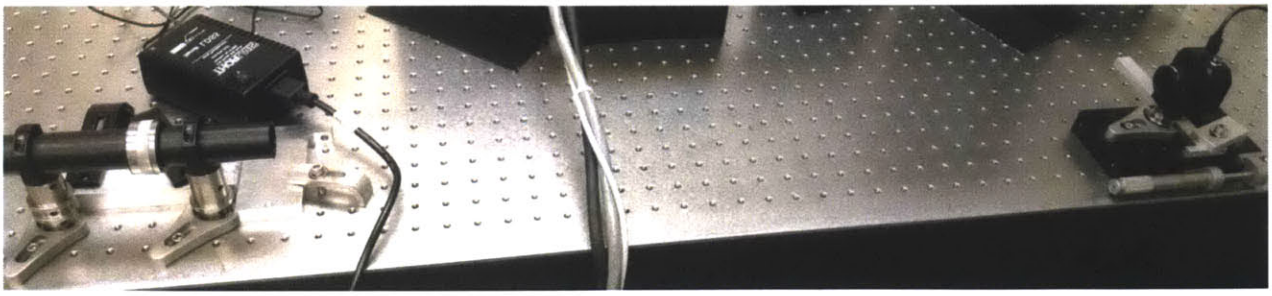

Figure 2.14 Experimental setup to measure beam divergence angle. The lens tube to the left emits 5 nearly-parallel beams. The camera is set up on the right, 835 mm away, and moved on a track ± 22.5 mm toward and away from the laser.

It should be noted here that although the curvature measurement accuracy is quite sensitive to beam parallelism, temperature measurements on the order of ±2 °C (a typical lab environment) are expected to change the parallelism about ±1.2 μrad, which results in an error in the quantity $\frac{\Delta\kappa_{actual}}{\Delta\kappa_{\varepsilon=0}}$ of less than ±0.1%. The uncertainty in the parallelism measurement is approximately ±40 μrad, yielding an uncertainty in $\frac{\Delta\kappa_{actual}}{\Delta\kappa_{\varepsilon=0}}$ of about ±2.5%.

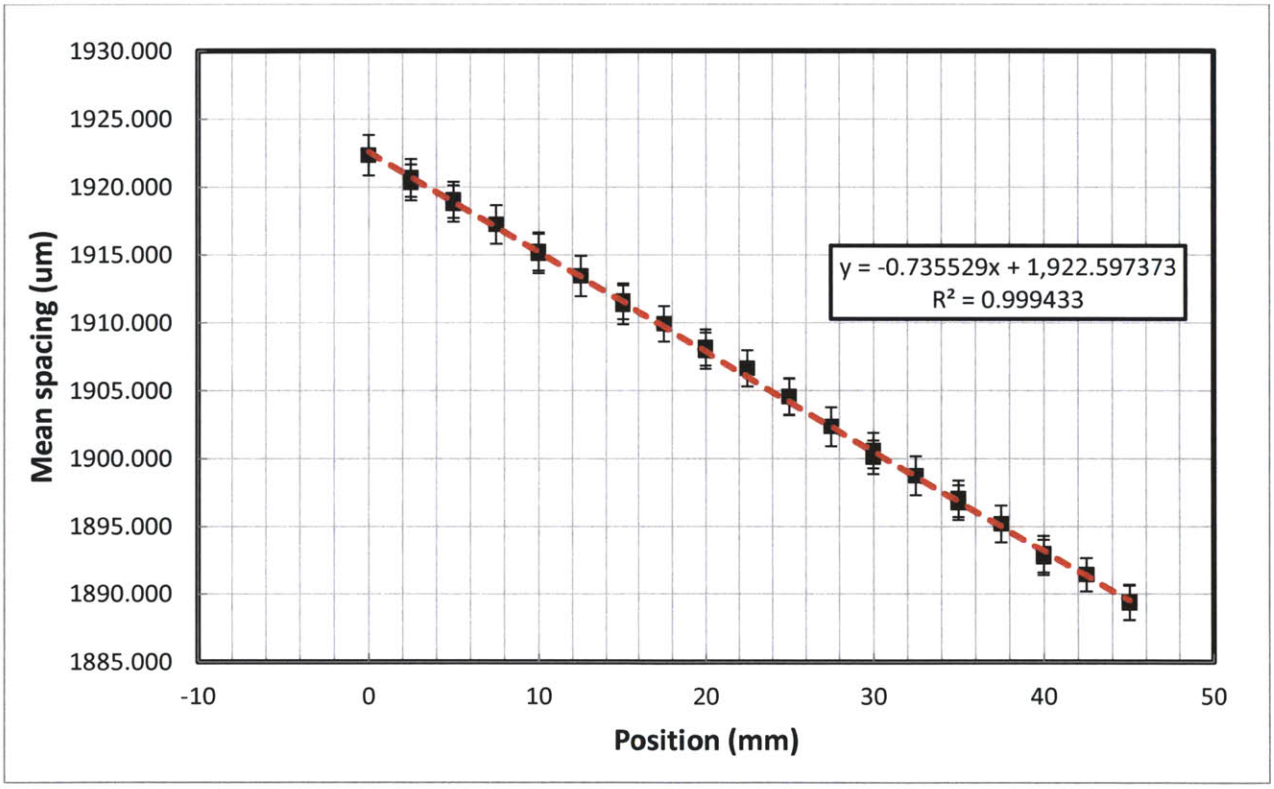

Figure 2.15 Results of parallelism measurement experiment, showing a divergence angle of ε = 0.736 mrad.

3 Figure correction of flat substrates

3.1 Introduction

The purpose of this thesis is to evaluate the feasibility of correcting figure errors in thin mirror substrates using ion implantation. Correcting non-flat substrates requires substantial investment in both metrology and implantation tools and techniques. Correcting flat substrates, however, is feasible with existing tools. This section describes efforts at using a commercial ion implanter to correct figure errors in flat silicon wafers. Silicon wafers are chosen rather than glass for two reasons: silicon exhibits a higher maximum integrated stress under the implantation conditions used in Section 2.3; and silicon is compatible with all standard semiconductor fabrication equipment.

3.2 Spherical curvature correction

Figure correction of spherical curvature error is the simplest case, since a uniform fluence distribution changes spherical curvature without affecting other shape components. In fact, it is this spherical curvature that was used to measure stress in the *ex-situ* measurements described in section 2.2. Using Stoney's equation [24], we may calculate the integrated stress required to eliminate a given spherical curvature.

$$S = \frac{B h_s^2 \kappa}{6} \qquad \text{Equation 3.1}$$

where S is the integrated stress, B is the biaxial modulus of elasticity of <100> silicon (180.5 GPa), h_s is the substrate thickness, and κ is the spherical curvature.

Using a 2nd order polynomial fit to the stress data of Section 2.3, the stress –fluence relationship may be estimated as

$$\phi = 3.47 \times 10^{12}\ S^2 + 6.96 \times 10^{12}\ S \qquad \text{Equation 3.2}$$

where S is given in units of N/m, and φ in units of ions/cm^2. As a purely empirical relation, the units of the coefficients in Equation 3.2 are specific to the units of S and φ. From Equation 3.1 and Equation 3.2, we calculated the fluence that was expected to eliminate the spherical curvature, and 22 silicon wafers[c] were implanted with this intention, using the parameters in Table 3.1. An example of a corrected wafer is shown in Figure 3.1. Histograms of the curvature before and after one cycle of correction are shown in Figure 3.2.

A sensible measure of successful curvature correction is the correction factor: the ratio between the actual change in curvature and the desired change in curvature,

$$C_\kappa = \frac{\Delta\kappa_{measured}}{\Delta\kappa_{destred}} \qquad \textbf{Equation 3.3}$$

The correction factor is a useful measure of how well-controlled the process is. Figure 3.3 shows a histogram of the correction factor.

Table 3.1 Spherical figure correction implant parameters

Substrate	Silicon <100>
Implant species	Si^+
Implant energy	150 keV
Implant flux	4.75 x 10^{12} ion/cm^2/sec
Substrate thickness	404 – 525 μm

[c] One of these samples was a very strong outlier and has been excluded from this analysis, as its correction factor, 0.28, is 4 standard deviations below the mean of the other 21 samples. This appears to be an error, either in measurement or ion fluence, but the cause has not been determined with certainty.

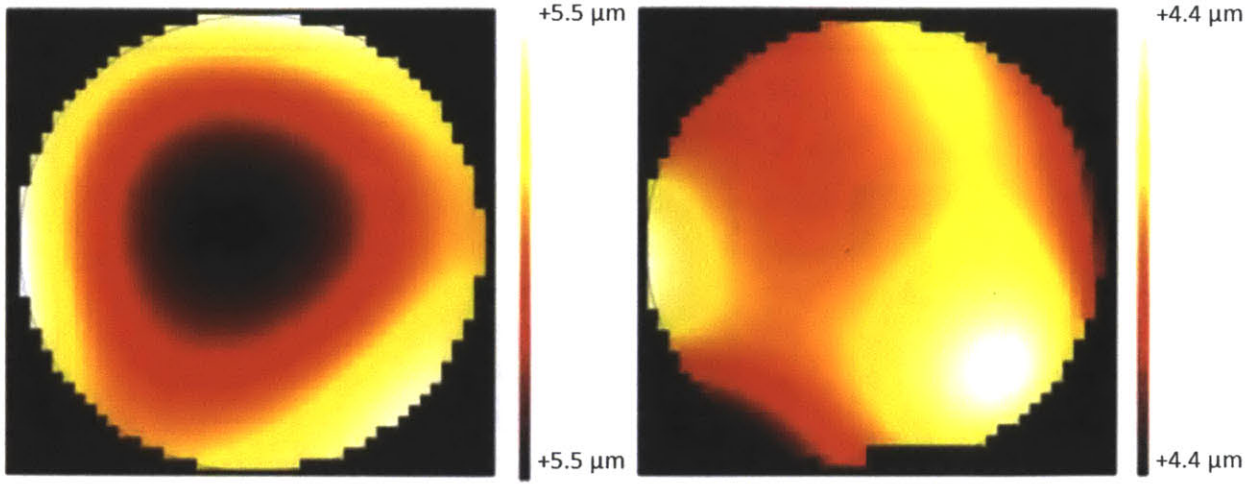

Figure 3.1 Surface maps of a corrected sample. The spherical curvature was reduced from 9 µm to -0.7 µm; a correction factor of 1.10. The residual surface error is primarily due to astigmatism and higher-order errors.

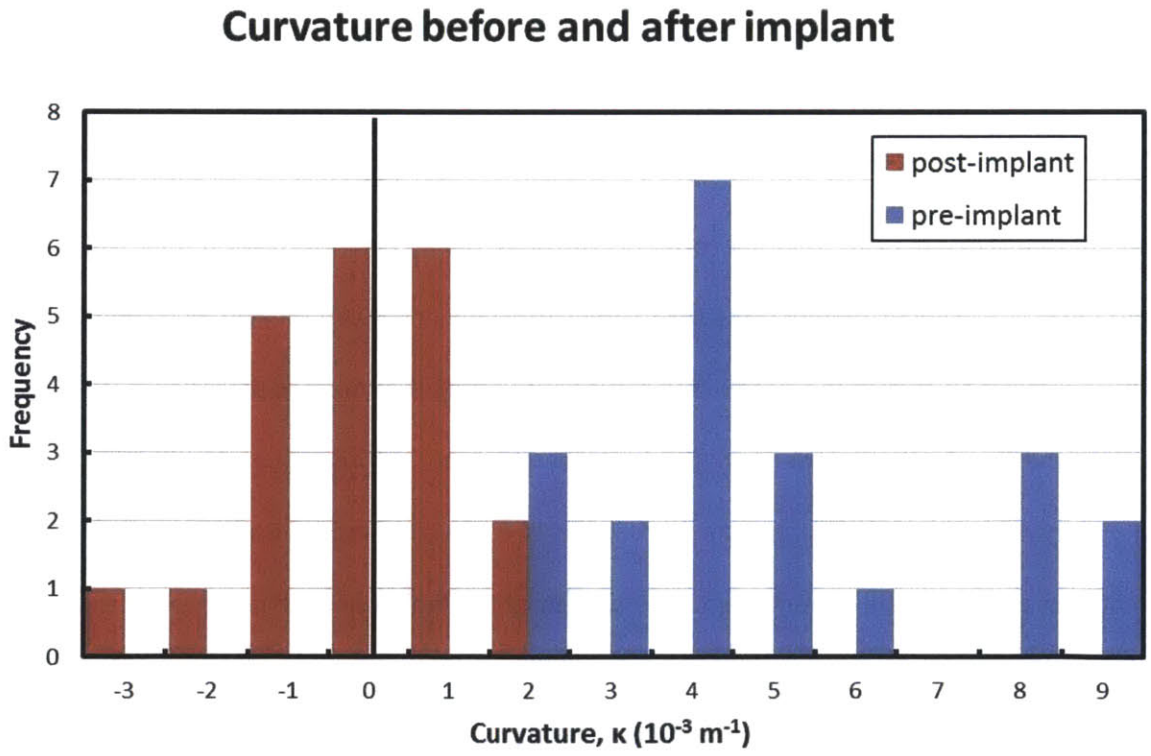

Figure 3.2 A histogram of the curvature before and after correction, showing that significant correction occurred. $\overline{\kappa_{pre}} = 0.0046\ m^{-1}$; $\overline{\kappa_{post}} = -0.0006\ m^{-1} \pm 0.0013\ m^{-1}$

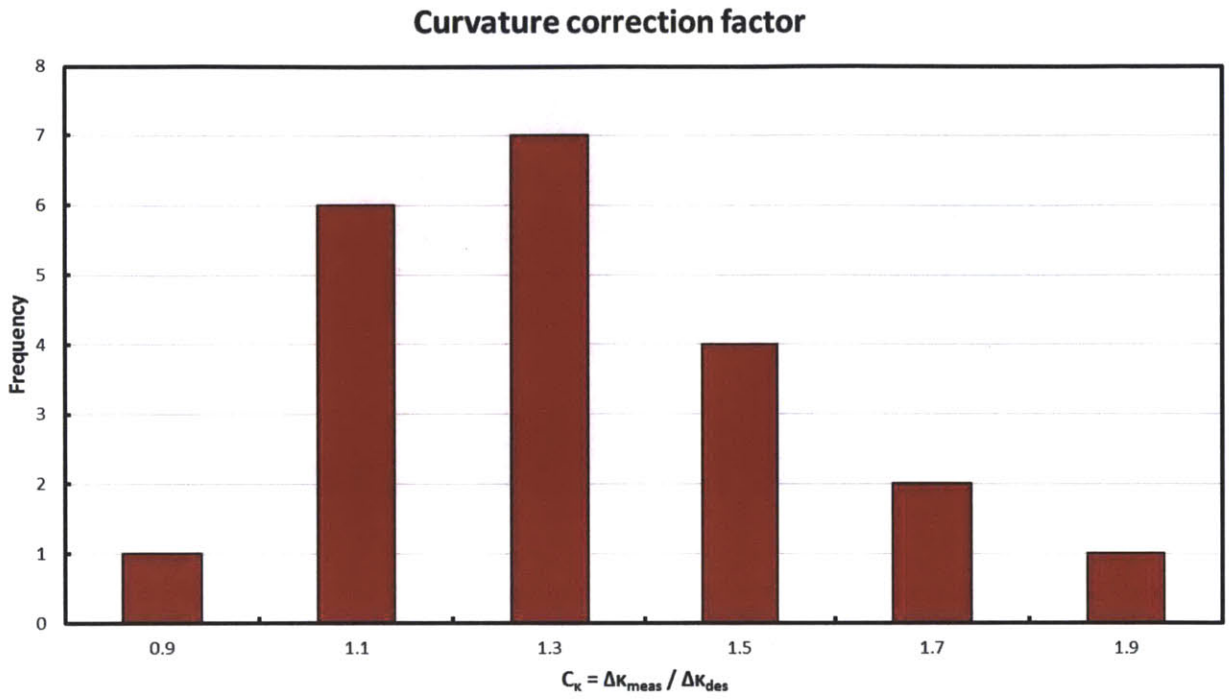

Figure 3.3 A histogram of the curvature correction factor, an indication of the effectiveness of the spherical curvature correction process, shows that the process mean is 25% too high, but does follow a normal distribution. $\overline{C_\kappa} = 1.23$; $S_{C_\kappa} = 0.24$

It is apparent that the spherical curvature correction process follows a normal distribution. The estimated mean is 1.23, indicating that the calculated correction stress was, on average, 23% too high. This would be simple to correct in a production setting. The estimated standard deviation is 0.24, implying that the process is not under very good control. This is not surprising, considering the sensitivity of many semiconductor fabrication processes to equipment and environmental conditions. The significant variation in the correction factor also highlights a limitation with using commercial implant services, where the process is difficult to fine-tune because we have no access to the equipment or the process details. For this reason, and the non-trivial expense that would be required, no attempt was made to better control the spherical curvature correction process.

This work shows that spherical curvature may be corrected in silicon wafers, but better process control is critical for practical correction. Since the process may be repeated until the desired level of residual

error is achieved, poor process control only increases the number of iterations required, and degrades the practical limit of correction. Better process control may be achieved through a better understanding of the causes of variation, such as: substrate temperature; thickness uncertainty; fluence uniformity and uncertainty. Understanding these factors will be part of the purpose of *in-situ* curvature measurements (Section 2.4).

3.3 Higher-order figure correction

Correction of higher-order figure errors, such as astigmatism or coma, is significantly more challenging than correcting spherical curvature error; and it is obvious from Figure 3.1 that removing spherical curvature only is insufficient for figure correction. For this work, correcting higher-order figure errors is especially challenging due to the limitation that commercial ion implanters can only implant a uniform fluence distribution. A method of masking samples is devised that allows the implantation of a non-uniform fluence distribution using a commercial ion implanter; and a method is devised for calculating the best-fit fluence distribution for correcting a given figure error.

One silicon wafer was implanted with a non-uniform fluence distribution, with the intention of correcting the astigmatism error. While the resulting change in surface shape, shown in Figure 3.4, is entirely astigmatism error, as expected, the magnitude is very small due to the low fluence used. Only one wafer was implanted in this way, because the masking method is very time-consuming. The method of fluence distribution calculation is useful background for correction of non-flat optics (Chapter 5).

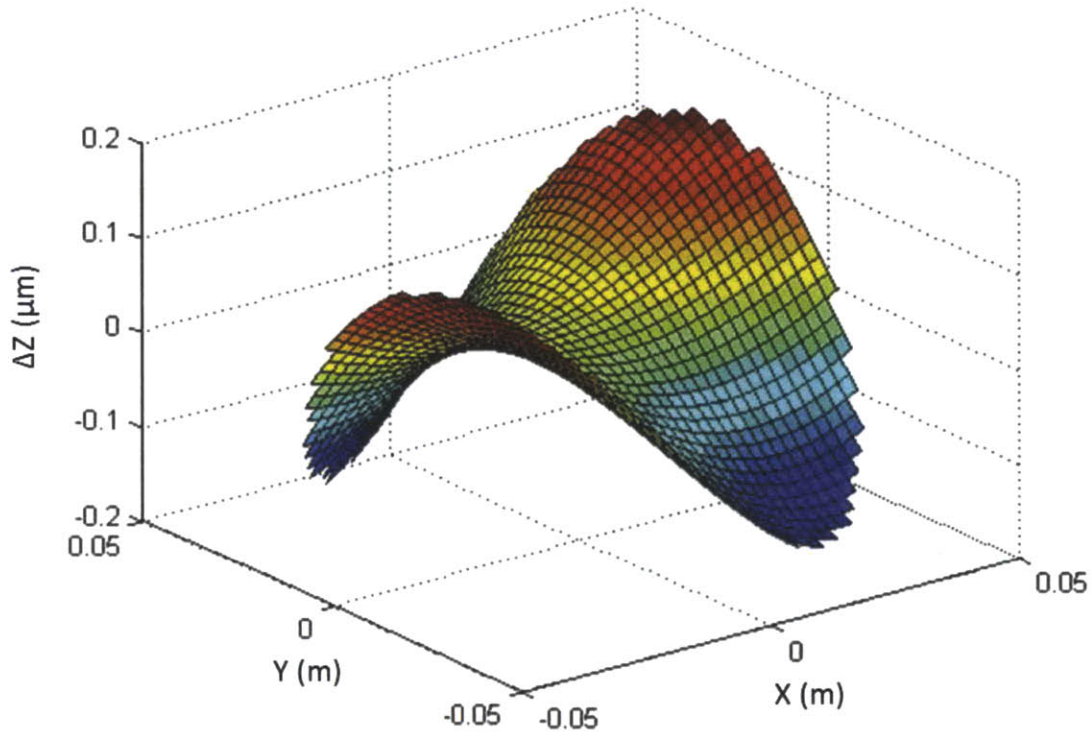

Figure 3.4 Change in shape of a silicon wafer after attempted astigmatism correction, showing a small change in figure but almost purely astigmatism.

3.3.1 Modeling

The goal of this modeling is to calculate the stress distribution over the surface of the wafer that most closely results in the desired change in figure. For example, Figure 3.4 shows a change in the astigmatism component of surface figure; in order to achieve this change in figure, a non-uniform stress distribution must be applied. The model described here allows calculation of this required stress distribution.

While calculating the shape change resulting from a given fluence distribution is a matter of developing a realistic FEA model, calculating the fluence distribution required to impart a desired change in shape (the inverse problem) is even more challenging. There are numerous methods to solve this inverse problem, including using influence functions [44] and finding the linear combination of influence

function magnitudes that results in the best fit shape (in a least-squares sense, for example). In this work, a slightly different method is used, where influence functions are replaced by Zernike polynomials. Zernike polynomials are chosen as test functions because the figure error of a flat silicon or glass wafer may typically be described very well with only about 14 Zernike polynomials.

The first step in solving the inverse problem, of calculating the ion fluence or stress distribution that results in the best shape change, is to build a library of deformed shapes resulting from applied stresses, where the applied stress distributions are described by Zernike polynomials. This is illustrated in Figure 3.5.

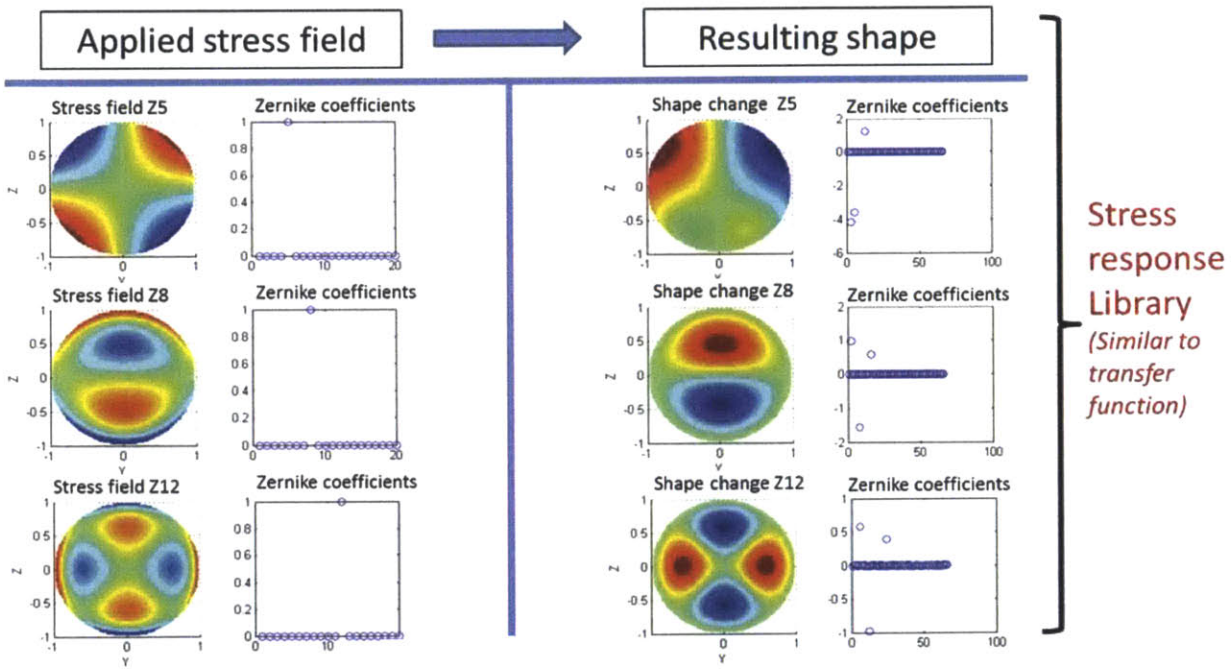

Figure 3.5 Stress-response library. A test function is applied as a stress distribution (left columns), and this results in a shape change (right columns). Both the test functions and resulting shape change may be described well by Zernike polynomials, shown as stem plots next to the functions.

A commercial finite element package, ADINA, is used to model the change in shape resulting from a given stress distribution input. The resulting shape change is automatically recorded by a MATLAB script, and the next stress input passed to ADINA. This is repeated until all test functions have been applied

sequentially, and their resulting shape changes recorded. Since the shape changes may be described quite well with Zernike polynomials, only the Zernike coefficients are recorded from each test function. The sets of coefficients describing each shape resulting from a test function input are then assembled into a single matrix, the Stress-Response Library.

Once the Stress-Response Library is assembled, finding the best-fit stress distribution is a matter of finding a linear combination of Stress-Response Library columns that result in the closest response to the desired shape change. This may be solved by a least-squares fit, shown in Figure 3.6. The magnitude of the error in the Zernike coefficients is minimized by multiplying the pseudoinverse of the stress-response library matrix by the desired Zernike coefficient vector.

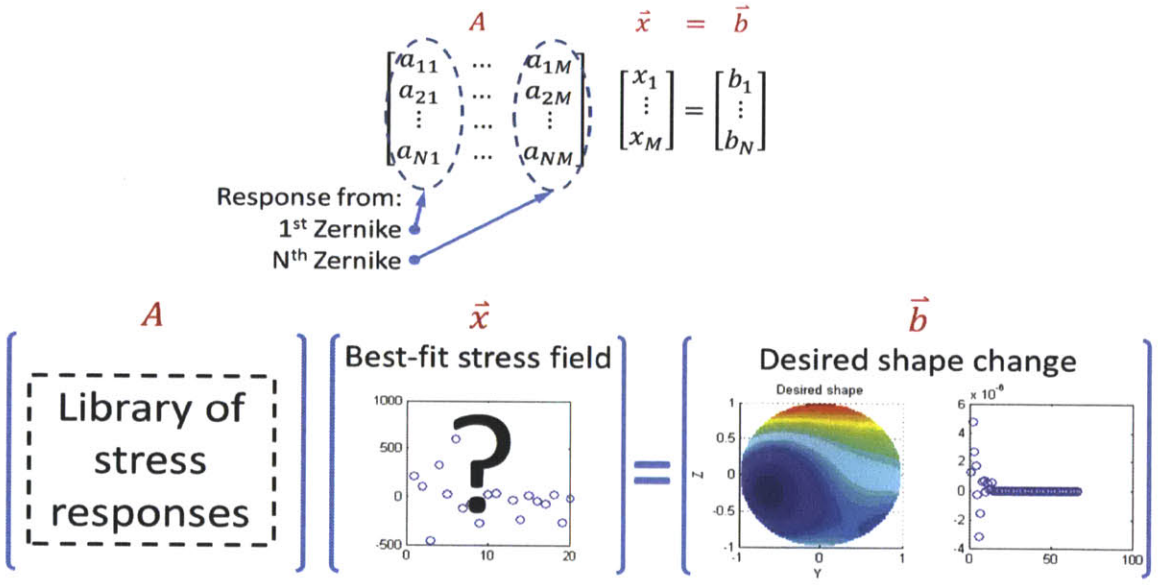

Figure 3.6 Finding the stress distribution that results in the best-fit figure involves solving a least-squares problem to fit the Zernike coefficients from the Stress-Response Library to the Zernike coefficients of the desired shape change.

As an example, Figure 3.7 shows the stress distribution required to correct astigmatism in a particular silicon wafer. For any astigmatism error, this distribution would be the same as in Figure 3.7, but rotated to match the orientation of the astigmatism for that particular sample. This simplifies correction of astigmatism in Section 3.3.2 by requiring only one photomask.

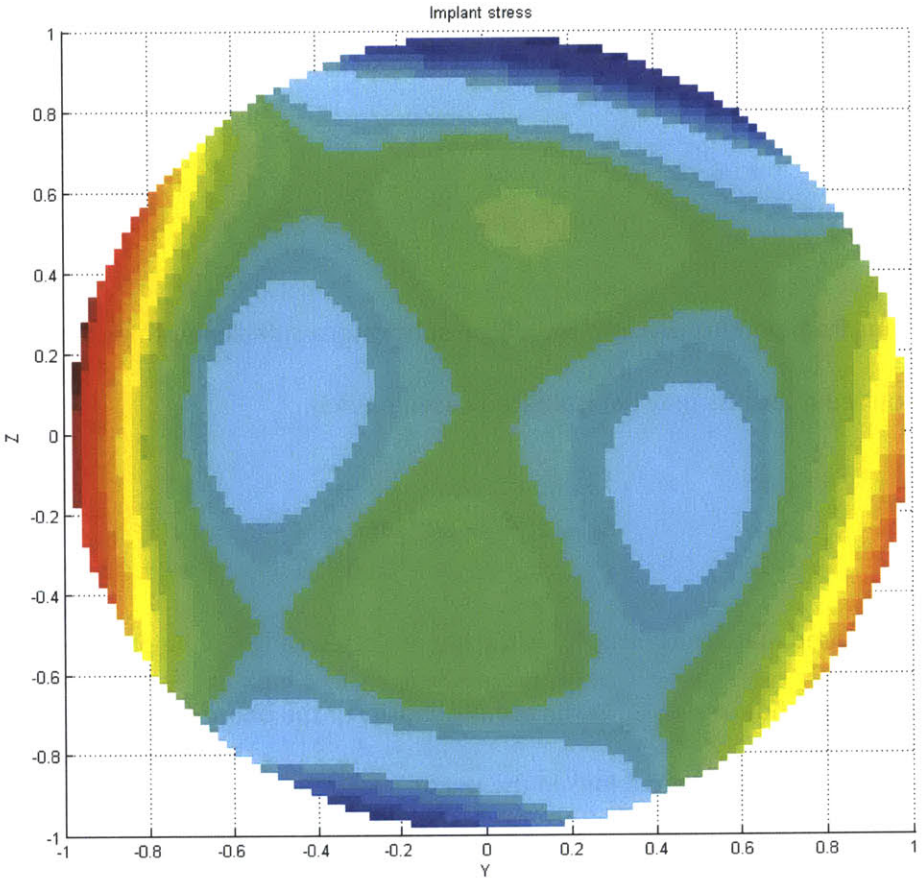

Figure 3.7 Stress distribution required for astigmatism correction of a particular sample. High stress areas, in this case, are near the edges, while the center requires little stress.

3.3.2 Masking process

A photoresist mask was used to apply a non-uniform fluence distribution to a silicon substrate. A contact mask was used because commercial ion implanters are set up to apply a uniform fluence over the surface of a wafer.

The preparation for masking a wafer is time-consuming, but not particularly complex. First, the wafer is measured, using the SNL Shack Hartmann Metrology System to determine the magnitude and alignment of the astigmatism error. The wafer is then coated with a positive photoresist on both sides, and soft-baked. The photoresist is then exposed on both sides using contact photolithography with the same contact mask in the proper orientation. The exposure is followed by development to dissolve exposed

photoresist. The wafer is then hard-baked at 250 °C to harden the photoresist in preparation for implanting. Finally, the masked wafer is implanted on both sides with an identical fluence. Details of the process are described below.

Photoresist thickness

In order to stop ions from penetrating into the silicon substrate, a sufficiently-thick photoresist layer is required. This required thickness may be estimated based on [45],

$$t_{mask} \geq R_p^* + \Delta R_p^* \sqrt{2 \ln \frac{C_p^*}{C_B}} \qquad \text{Equation 3.4}$$

where t_{mask} is the required mask thickness, R_p^* is the ion projected range in the photoresist, ΔR_p^* is the projected straggle in the photoresist, C_p^* is the atomic density of the photoresist and C_B is the desired background concentration of implanted ions in the silicon substrate (e.g., $C_B = 10^{15}$ ion/cm^3 corresponds to a fluence of ~10^{11} ion/cm^2). From Equation 3.4, using values obtained from SRIM, it was determined that a photoresist thickness $t_{mask} \geq 0.5$ μm is required to stop the ions. The standard photoresist available in the Microsystems Technology Laboratory (MTL) at MIT is OCG-825, and is typically spun-on at a thickness of 1 μm. Thus, a photoresist thickness of 1 μm was chosen.

Photomask generation

A 5" chrome-on-glass contact photomask was purchased, with the pattern shown in Figure 3.8. The pattern consists of 0-500 μm squares arranged on a grid, with 500 μm spacing, covering the surface. The size of each chrome square (shown in black and pink in the images on the right side of Figure 3.8) is calculated from the Matlab script described in Section 3.3.1, and a DXF file is generated with squares marking where chrome should remain on the photomask. This file was then sent to a company for the photomask to be written.

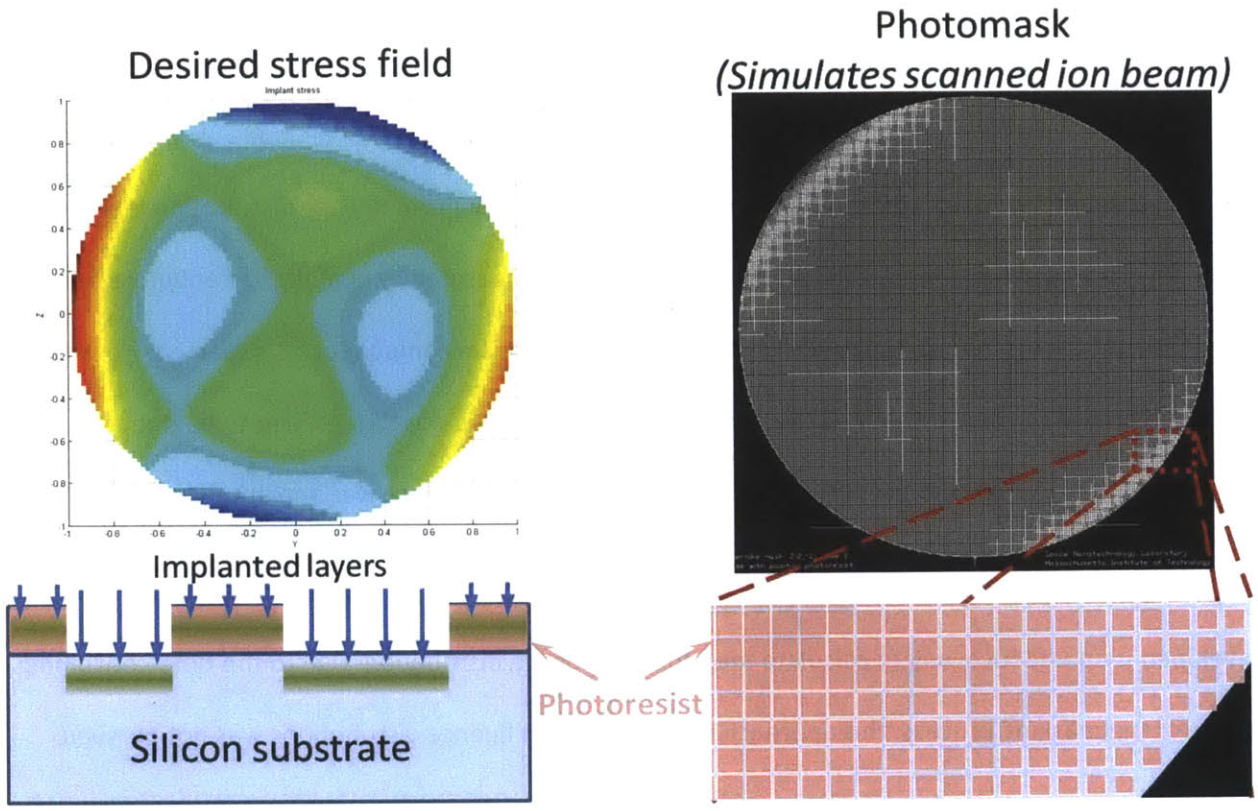

Figure 3.8 A photomask is used to pattern photoresist spun on the substrate surface, in order to implant a non-uniform fluence distribution over the surface of the substrate. This allows correction of higher-order figure errors

Substrate alignment

One challenge with this process is aligning the substrate properly to correct the astigmatism error. The astigmatism error does not necessarily align with the flat of the wafer, so the alignment features on the contact lithography tool were removed to allow rotation of the wafer relative to the mask. The accuracy of the rotation is estimated to be ±2°, as this was done using a protractor with a poor reference edge.

In addition to rotating the wafer, since the entire wafer is exposed, alignment of the photomask to be concentric with the wafer was a challenge. It was possible to see the wafer edges through the uncovered sections of the photomask, and concentricity to within 100 µm was achieved.

With significant additional work, proper alignment of the wafer to the photomask could be achieved, but this was not considered a worthwhile use of time at this stage.

3.3.3 Results

The final result of the one wafer that was implanted with a non-uniform fluence distribution is shown in Figure 3.4. This figure shows the difference between surface measurements of the wafer before and after implanting. The change in figure is entirely in the astigmatism component, as expected. However, the magnitude of the shape change is far smaller than desired. This was determined to be due to a mistake in the implanted fluence; only about 10% of the required fluence was implanted.

This result demonstrates that correction on higher-order figure errors is feasible, and that the model developed is an effective way to calculate the required fluence distribution. Due to the time-consuming nature of the masking process, this approach for non-uniform fluence distributions was not pursued further.

4 Roughness and relaxation studies of implanted substrates

4.1 Introduction

X-ray telescope mirrors must have low roughness over length scales similar to the wavelength of light being reflected ($\lambda \sim 0.5 - 5$ nm), in order to maintain high reflectivity. Both glass and silicon substrates have very smooth surfaces, with RMS roughness typically 1 nm or smaller. It is therefore important that ion implantation does not significantly roughen the surface. The first part of this chapter describes studies to evaluate whether surface roughness is altered by ion implantation, using x-ray reflectivity of hard x-rays to measure roughness.

It is also critical that the figure of x-ray telescope mirrors is stable over many years. It is unknown whether ion implanted substrates are stable over long periods of time, but this is a critical requirement for ion implantation to be used as a figure correction process. The second part of this chapter describes various experiments to evaluate the stability of ion-implanted glass and silicon substrates.

4.2 Roughening of implanted substrates

As high-energy ions move through a substrate, they interact with the atoms in the substrate, either through electronic or nuclear energy deposition. While the ions have a high velocity, most energy loss is through electronic energy deposition. Thus, near the surface, the substrate atoms are expected to be largely unaffected by the implanted ions; so roughness is expected to be minimally-affected. This is critical for correcting figure errors in x-ray telescope mirrors, because it is necessary to implant on both sides of the mirror. Any roughness introduced will be transferred to the reflective layer, reducing x-ray reflectivity. Therefore, to evaluate the effect, if any, of ion implantation on surface roughness, we measured surface roughness of several silicon and glass substrates, using x-ray reflectivity, before and after implantation. The results show a minimal effect on roughness.

Some investigators have observed both roughening and smoothening effects in irradiated silica [46][47], molybdenum [48], platinum films [49], and others. These effects are attributed to either viscous relaxation near the surface or material ejection from ion tracks near the surface.

For these studies, we measured x-ray reflectivity curves for samples before and after 150 keV Si+ ion implantation with fluence that would be realistically used for figure correction. The results are summarized in Table 4.1, and typical results are shown in Figure 4.2 and Figure 4.3.

4.2.1 Background

For x-rays, the real part of the refractive index is less than 1, typically by a few parts per million. Thus, at small grazing angles (i.e., large angles of incidence) below a critical grazing angle θ_c, total external reflection occurs. As the grazing angle is increased beyond θ_c, reflectivity falls rapidly. Surface roughness on the same length scale as the incident x-ray wavelength will reduce the specular reflectivity further, both above and below the critical angle. For samples with thin films, such as silicon with a thin native oxide layer, interference effects are also observed. The X-ray beam partially transmits through thin surface films, and reflects off of interfaces, resulting in interference fringes as the angle of incidence is changed.

X-ray reflectivity curves are obtained using a goniometer, with a well-collimated incident x-ray beam. The grazing incidence angle and the detector angle are increased in small increments and the specular reflectivity is measured. This goniometer setup is illustrated in Figure 4.1. The reflectivity data is fit to a model that includes many fit parameters. These include electron density, layer thickness, and interface roughness, for each layer present; as well as system parameters such as background counts and 2θ offset.

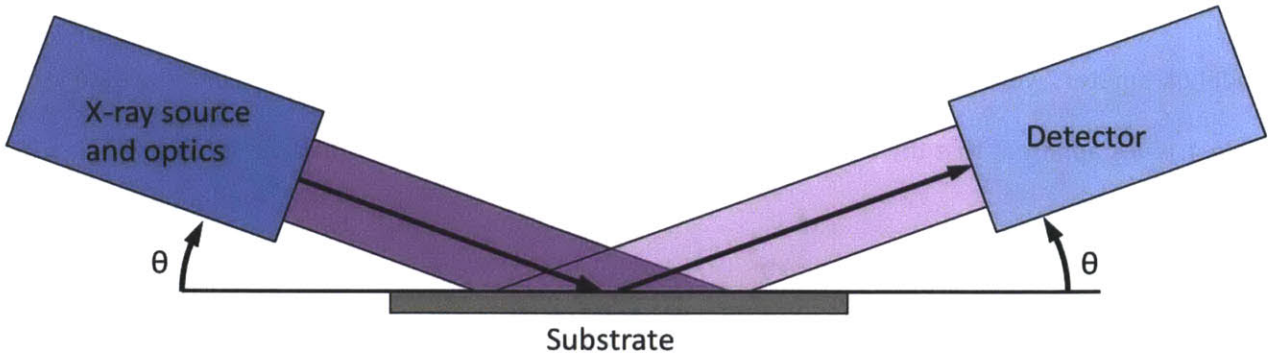

Figure 4.1 Measurement of an X-ray reflectivity curve requires measuring grazing-incidence specular reflection of a sample, by moving both the source and detector each by θ.

4.2.2 Experimental procedure

Samples were prepared for x-ray reflectivity measurement by cleaning in a solution of 3 H_2SO_4: 1 H_2O_2 for 10 minutes, to remove any organic layers that would interfere with the reflectivity measurements. This cleaning was performed, and the samples kept sealed in plastic wafer carriers, within hours prior to reflectivity measurement.

The sample being measured was then placed on the measurement stage of a Rigaku SmartLab Multipurpose Diffractometer, with a Cu Kα x-ray source (λ=1.54 Å, 9 kW rotating anode). The sample height and tilt was then set using a mostly-automated procedure. Finally, a 2-theta scan, where the grazing incidence angle and detector angle are simultaneously scanned, was started to collect reflectivity data from 2θ = 0° (parallel to surface) to 8°. The sample was then sent out for ion implantation. After implantation, the sample was once again cleaned as before, and shortly thereafter measured.

4.2.3 Results

There was little effect on surface roughness measured by x-ray reflectivity. An example pair of reflectivity curves for silicon before and after implantation, with models for 5 Å and 6 Å RMS roughness, is shown in Figure 4.2. In these models for silicon, the model parameters were: substrate roughness, native SiO_2 layer thickness (~1 nm), SiO_2 roughness, and background level. A similar pair of curves for D-

263, with models for 3 Å and 4 Å RMS roughness, is shown in Figure 4.3. In the models for glass, the model parameters were the roughness and background level only. From these figures, and the data in Table 4.1, it is apparent that the change in roughness was significantly lower than 1 Å for both substrates.

Table 4.1 Summary of results for all samples measured in this study. The silicon roughness values are only estimates, due to the poor correspondence between the model and data; however, all three silicon samples appeared nearly identical before and after ion implantation, similar to Figure 4.2.

Sample name	Implanted fluence (Si^+/cm^2)	Stress (N/m)	$\sigma_{pre\text{-}implant}$ (Å)	$\sigma_{post\text{-}implant}$ (Å)	$\Delta\sigma$ (Å)
G25	control	1.0	3.36	3.42	+0.06
G31	1×10^{14}	11.6	3.20	3.38	+0.18
G32	2×10^{14}	13.4	3.26	3.48	+0.22
Si34	control	-0.5	5 – 6	5 – 6	< 1
Si36	2.01×10^{15}	-31.9	5 – 6	5 – 6	< 1
Si43	6.14×10^{15}	-32.5	5 – 6	5 – 6	< 1

Models for silicon with 1-2 nm SiO_2 do not fit the experimental data very well. The reason for this is not yet understood, but may be due to density changes near the surface since the crystalline silicon there is becoming amorphous silicon, which has a density about 3% lower than crystalline silicon [29]. There is also uncertainty of the thickness of the native oxide layer, as well as the presence of any organic layers. Regardless of the quality of fit, it is clear from the models shown that the change in roughness of our samples is almost undetectable and significantly less than 1 Å. All three silicon samples showed very similar behavior.

The models for D-263 reflectivity fit the data better than for silicon, but there is uncertainty in the near-surface glass density before and after implantation, the exact composition of the glass, and the presence of any organic contamination layers. However, once again, it is clear from Figure 4.2 that the change in roughness is significantly less than 1 Å.

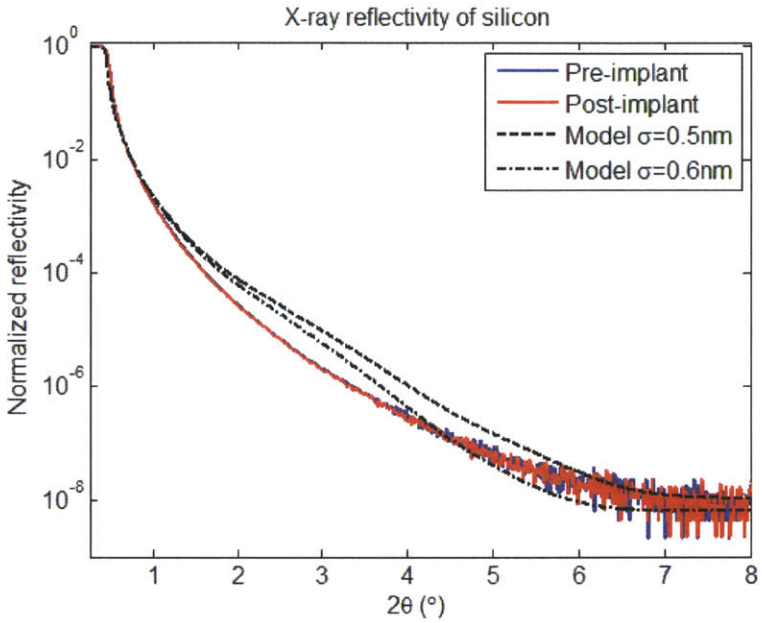

Figure 4.2 X-ray reflectivity data and models for pre- and post-implant silicon wafer. The fluence was 2 x 10^{15} ions/cm^2, the implanted species was Si^+ 150 keV, and the beam current was 60 µA.

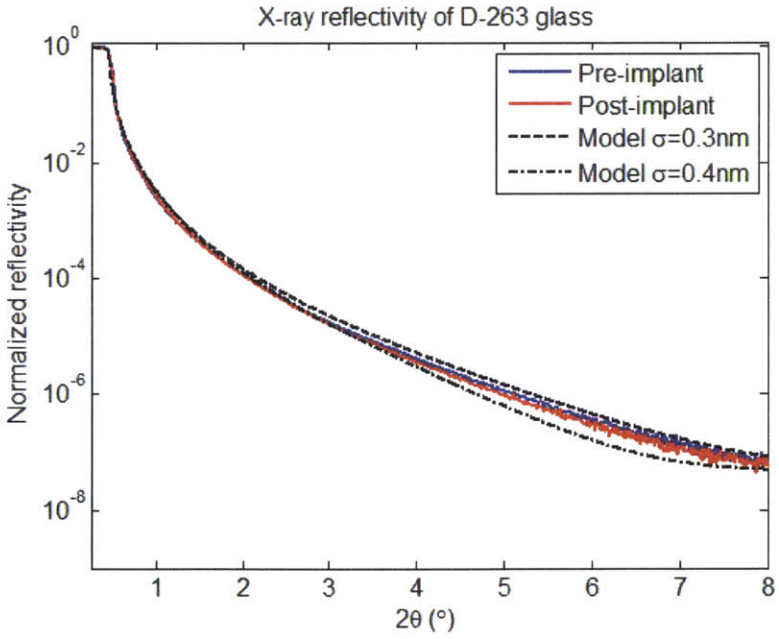

Figure 4.3 X-ray reflectivity data and models for pre- and post-implant D-263 wafer. The fluence was 2 x 10^{14} ions/cm^2, the implanted species was Si^+ 150 keV, and the beam current was 60 µA.

4.2.4 Conclusions regarding surface roughness

From these data, we have determined that roughness is not significantly increased by ion implantation of both types of substrates with 150 keV Si^+ to fluences that are relevant to figure correction. As further research is conducted with higher ion energy, surface reflective layers, and other changes to implantation parameters, samples should be monitored for changes in surface roughness, as it is possible that the small changes presented here are unique to these particular conditions.

While x-ray reflectivity measurements are a useful check on surface roughness, an alternative method of measurement is atomic force microscopy (AFM). AFM is sensitive to surface cleanliness, and does not measure an average surface roughness over a very large area (typically < 10 x 10 μm). However, AFM gives a more direct measure of surface roughness, and is capable of providing a power spectral density (which specular x-ray reflectivity measurements do not provide), which may provide more useful information for x-ray telescope mirrors.

4.3 Stability of implanted glass and silicon substrates

It is important that implanted substrates be stable over long time periods. The Chandra Observatory was launched in 1999, and it continues to produce high-resolution images 15 years later. Without 15 years to wait for relaxation data, we chose an alternative method: raise the temperature of the implanted samples for 4 hours each at successively higher temperatures, and measure the curvature before and after each bake cycle. These thermal testing data, shown in Figure 4.4, suggest that no relaxation in excess of the repeatability of the Shack-Hartmann Surface Metrology Tool (SHSMT) occurred. We also measured samples after 1 year of storage in a normal laboratory environment. Again, the measured relaxation, shown as a histogram in Figure 4.5, is very small and is not significant in comparison to the measurement repeatability. These data in no way conclusively prove that relaxation is not an issue to be concerned with; continued monitoring of existing and future samples is certainly warranted, perhaps with more robust long-term metrology procedures. Recent results from other investigators [50], [51]

show relaxation of glass at room temperature over long periods, so continued monitoring is definitely warranted.

4.3.1 Thermal cycle testing of glass

Many relaxation processes, including relaxation of glasses [52], follow Arrhenius' equation, which describes an exponential relationship between temperature and reaction rate (in this case, the relaxation rate),

$$\frac{K_1}{K_0} = e^{\frac{-E_a}{R}\left(\frac{1}{T_1}-\frac{1}{T_0}\right)} \qquad \text{Equation 4.1}$$

where K_0 and K_1 are the relaxation rates at temperatures T_0 and T_1, R is the universal gas constant, and E_a is the activation energy associated with the relaxation process. E_a is unknown for implanted substrates, but may be similar to relaxation in tempered glass, where E_a has been measured to be 300-500 kJ/mol [53].Choosing T_0 = 293 K, T_1 = 343 K, and E_a = 300 kJ/mol, $K_1/K_2 > 10^8$. Thus, exposure to 70 °C for 4 hours corresponds to > 60,000 years, and is sufficient to establish long-term stability of the implanted glass.

The experimental procedure was to measure a set of implanted D-263 glass wafers; heat the wafers in an oven for 4 hours at 40, 50, 60, or 70 °C; re-measure; re-heat, and repeat. This process is illustrated in Figure 4.4. In addition to the glass samples, one silicon sample was tested at temperatures up to 250 °C, and experienced less than 0.5 N/m for all temperatures tested. For this experiment, the measured quantity was the radius of curvature, measured using the SHSMT. The repeatability of this instrument at the time was approximately 1 N/m.

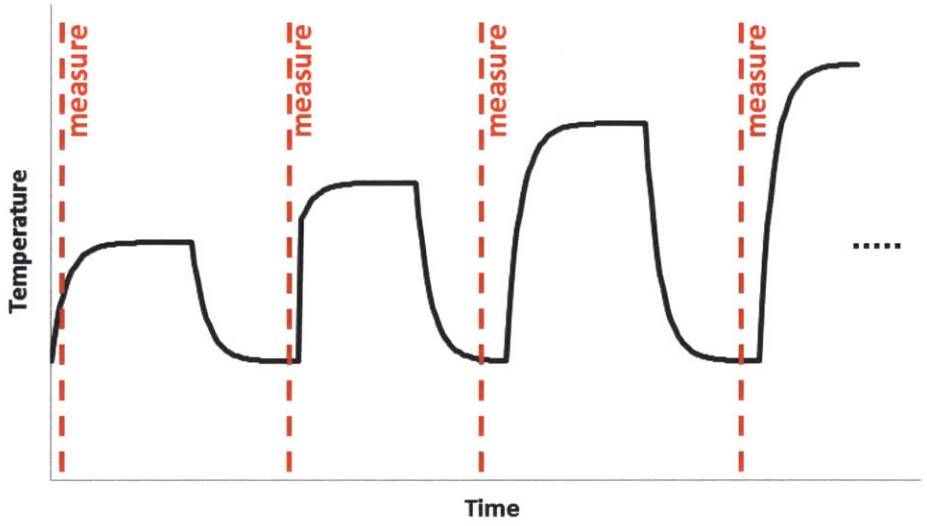

Figure 4.4 Illustration of sample temperature throughout thermal cycling experiments. Samples were measured after each thermal cycle to monitor changes in curvature.

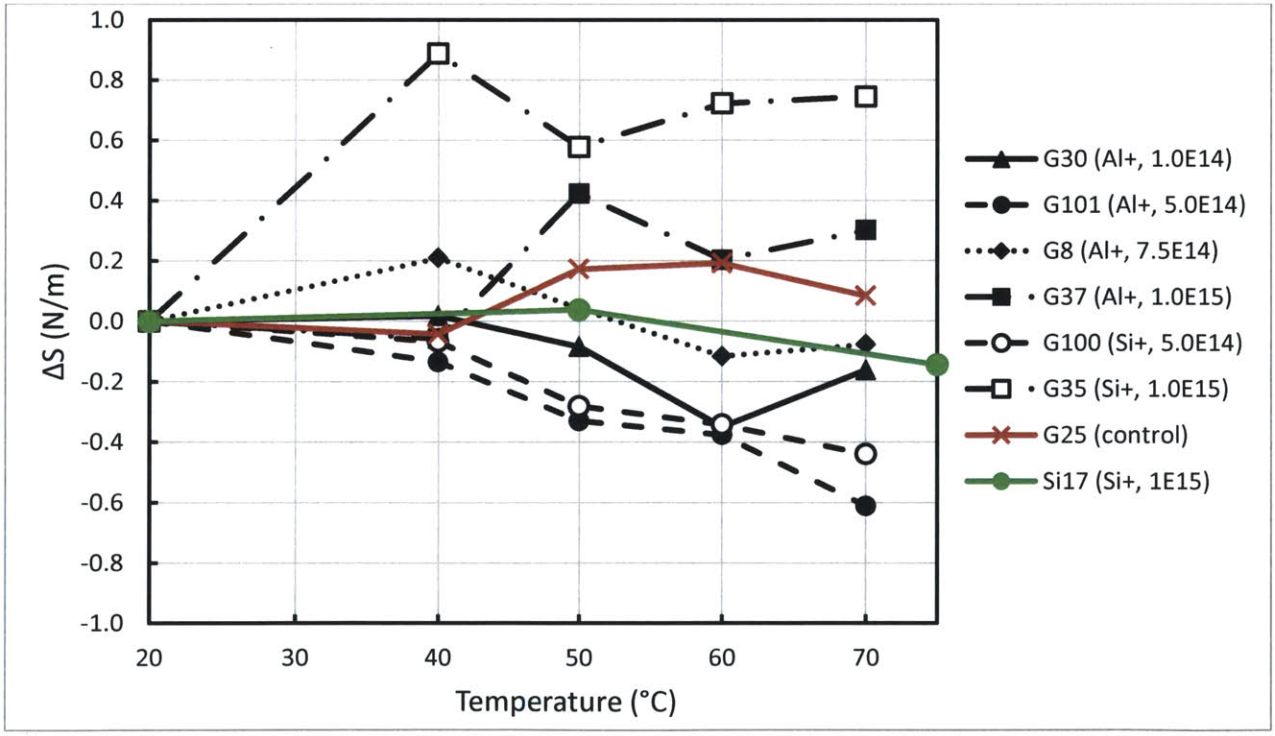

Figure 4.5 Change in integrated stress after each bake cycle. The repeatability of the metrology is approximately 1 N/m.

The results of this experiment are shown in Figure 4.5. Any of the wafers may have experienced changes in curvature for any individual sample. However, these changes were within the repeatability of the

metrology tool at the time; and while some samples experienced changes in curvature consistent with relaxation (ΔS positive in Figure 4.5), others experienced the opposite change in curvature.

These results inform us that ion implanted glass or silicon samples do not relax more than 1 N/m when thermally cycled up to 70 °C. Whether this is sufficiently-low relaxation for x-ray telescope mirrors depends on the telescope design and targeted resolution; for high-resolution mirrors, more accurate measurements should be conducted. These results do demonstrate that implanted glass and silicon wafers are robust to elevated temperatures.

4.3.2 Temporal relaxation measurements

A more direct measurement of relaxation of implanted glass and silicon would be to measure samples over time. Samples implanted between December 2012 and August 2013 were measured after implantation, and again in August 2014. These measurements are unfortunately difficult to accurately perform, due to changes—such as re-alignments, repairs and upgrades—that occur with the metrology tool (the SHSMT). However, the results give some valuable insight and suggest that small relaxation in some samples may occur; but again, this relaxation is small in comparison to the variation in the measurements.

The curvature of each of the samples analyzed here was measured with the SHSMT after the samples were implanted, with fluences ranging from 10^{14} to 10^{16} ions/cm^2. The samples were then stored for more than one year in wafer carriers or wafer boats, in a room where temperature was held to 25 °C ± 2 °C. The samples' curvature was then measured again, using the SHSMT.

The results of this experiment are shown in Figure 4.6, for both silicon and glass samples. Table 4.2 lists the average and standard deviation of the change in integrated stress for both materials, after excluding three extreme outliers, which will be discussed shortly. Positive ΔS indicates relaxation. The average

relaxation is about 25% of the standard deviation of the samples, suggesting that there is no significant relaxation.

Table 4.2 Summary of changes in integrated stress measured after 1 year of storage. Positive ΔS indicates relaxation.

	Silicon[d]	D-263	All
Number of samples	12 [9 + 3 outliers]	12	24 [21 + 3 outliers]
Average ΔS (N/m)	-0.5	+1.27	+0.4
Standard deviation of ΔS (N/m)	2.2	1.8	2.2

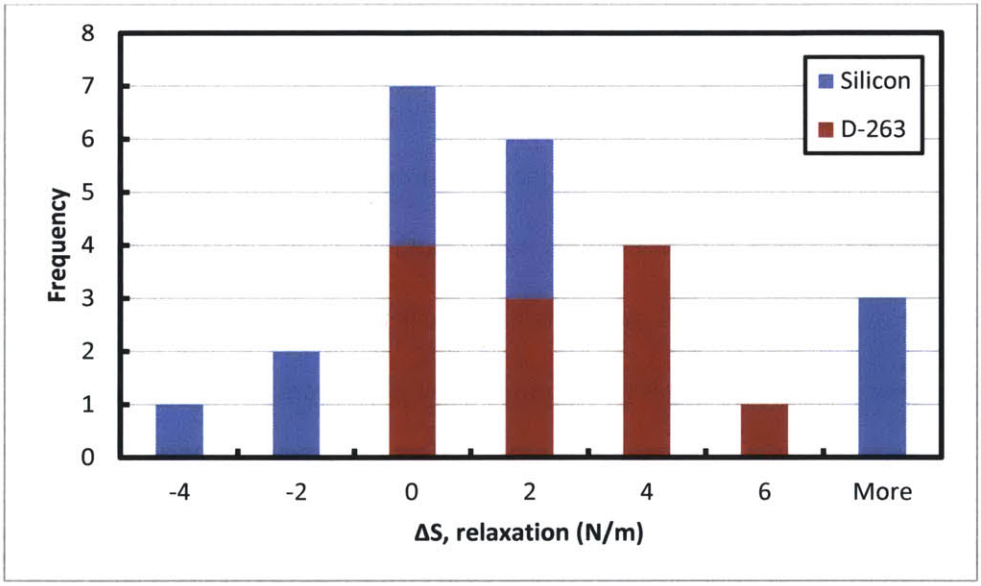

Figure 4.6 Histogram of relaxation data for silicon and D-263 glass substrates, measured after 1 year. $\overline{\Delta S} = 0.4$ N/m; $\sigma_S = 2.2$ N/m, after excluding the 3 extreme outliers.

Three silicon samples were excluded from this analysis. These samples had been implanted in excess of the critical fluence (~8 x 10^{15} ions/cm^2), and they were the only samples to exhibit substantial relaxation. These samples' attributes are shown in Table 4.3; it is clear that these are extreme outliers to the remainder of the data. It is interesting that these samples exhibited such dramatic relaxation, as the

[d] This data excludes 3 outliers, which were implanted with fluence exceeding the critical fluence; these samples experienced very high relaxation, over 4 standard deviations higher than the mean of the remaining samples.

implanted regions of these samples are mostly composed of amorphous silicon [29], while the other samples probably do not contain a continuous amorphous layer. This is valuable information, since it may indicate that avoiding fully-amorphized silicon may reduce the risk of relaxation.

Table 4.3 Details of outlier samples that were implanted with a fluence beyond 8 x 10^{15} ion/cm^2, which corresponds approximately to the fluence at which integrated stress in Figure 2.3 began to decrease.

Sample	1	2	3
Implant date	1/7/2013	11/26/2012	11/26/2012
Implant fluence (Si^+/cm^2)	0.91 x 10^{16}	1.1 x 10^{16}	1.2 x 10^{16}
Implant integrated stress, S_0 (N/m)	-53.0	-28.4	-31.4
Relaxation, ΔS	+11.1	+25	+14.9

4.4 Conclusions and future work

The data presented in Sections 4.2 and 4.3 demonstrate that both surface roughness and relaxation of implanted glass and silicon samples show results that are acceptable for thin x-ray telescope mirrors. Both of these issues should be monitored throughout future work; although they may be time-consuming measurements to make, they are critically-important for the success of this technology.

Roughness is not significantly altered in bare silicon or D-263 glass substrates, as demonstrated by x-ray reflectivity measurements. This technique has a certain appeal due to the use of x-rays, but relies on models to determine roughness. Soft x-ray reflectivity measurements would be ideal, but equipment is not readily available. Atomic Force Microscopy (AFM) may be a good alternative to obtain the power spectral density of the implanted surfaces; however, obtaining accurate results with AFM is non-trivial for such smooth surfaces. X-ray reflectivity measurements are useful as a monitoring tool for roughening.

Relaxation should continue to be monitored in existing implanted glass and silicon samples, to ascertain any trends in relaxation measurements. As we might use implant conditions different from those used for the existing samples, relaxation should continue to be monitored for a variety of implant conditions.

5 Numerical studies of thin segmented x-ray telescope mirrors

5.1 Introduction

In the previous chapters, we demonstrated figure correction of thin, flat substrates. Two questions remain regarding the feasibility of using ion implantation for correction of thin segmented x-ray telescope mirrors:

1. Can thin segmented x-ray telescope mirrors be corrected using surface stress?
2. Can ion implantation impart enough stress to effectively correct figure errors?

This chapter is concerned with answering these two questions. Of course, many other important questions remain, such as: how does uncertainty in the applied stress distribution affect correction effectiveness? How does ion beam size affect our ability to correct figure errors? Such questions, however, are questions of engineering rather than questions fundamental to the feasibility of using ion implantation for figure correction.

The two questions addressed in this chapter are more critical: if significant figure correction using surface stress were impossible, there would be no sense in further pursuing ion implantation for this purpose; likewise, if the magnitude of stress required for significant figure correction were orders of magnitude higher than our experiments suggest are possible, then ion implantation would not be a viable solution in the near future. Fortunately, the answer to both of the above questions is yes! Ion implantation is a plausible method of figure correction for thin segmented x-ray telescope optics.

Segmented X-ray telescope mirrors have a nearly cylindrical shape, such as in Figure 5.1, with a significantly different stiffness in the axial and radial directions of the optic. In this chapter, numerical studies of correction of representative conical thin segmented mirrors are presented. It will be shown that significant correction may be achieved using ion implantation, reducing the simulated figure error of the representative mirror from 6 arc second Half-Power Diameter (HPD) to approximately 1.5 arc

second Half-power diameter (HPD), a reduction factor of about 4:1. This is in agreement with figure correction simulations in the literature [44]. In addition, such a correction requires a maximum stress of only about 150 N/m, a stress that is achievable with silicon substrates (e.g., Section 2.4 and [29]), thermal oxide on silicon (e.g., Section 2.4 and [40]), and glass[e] [43]. For this work, a total of three mirror corrections were simulated, as a demonstration of important features and the methodology.

5.2 Methodology

Correction of segmented x-ray telescope optics was simulated by finding influence functions for a unit integrated stress at each location on the optic surface, using ADINA finite element software coupled with Matlab. These influence function were collected in Matlab, and the required stress distribution was calculated using constrained least squares to match the influence functions to a desired shape change. This methodology shares similarities with [44]. Using this method, the effect of the limit of applied integrated stress on the residual figure errors was studied.

5.2.1 Mirror geometry

Concepts for x-ray observatory optics using thin segmented mirrors typically employ tens to hundreds of modules each consisting of tens to hundreds of mirror pairs. Each pair includes one primary (typically parabolic) and one secondary (typically hyperbolic) mirror, coaxially-aligned to one another. This concept is illustrated in Figure 1.4. The minimum radius is typically no smaller than 200 mm, and the maximum radius typically extends no larger than about 1500 mm. A typical mirror length along the optical axis is 200 mm. A typical focal length is 10 meters. Figure 5.1 illustrates the important parameters used in the simulations in this chapter, and Table 5.1 summarizes these dimensions.

[e] Regrettably, this has not been demonstrated in this thesis.

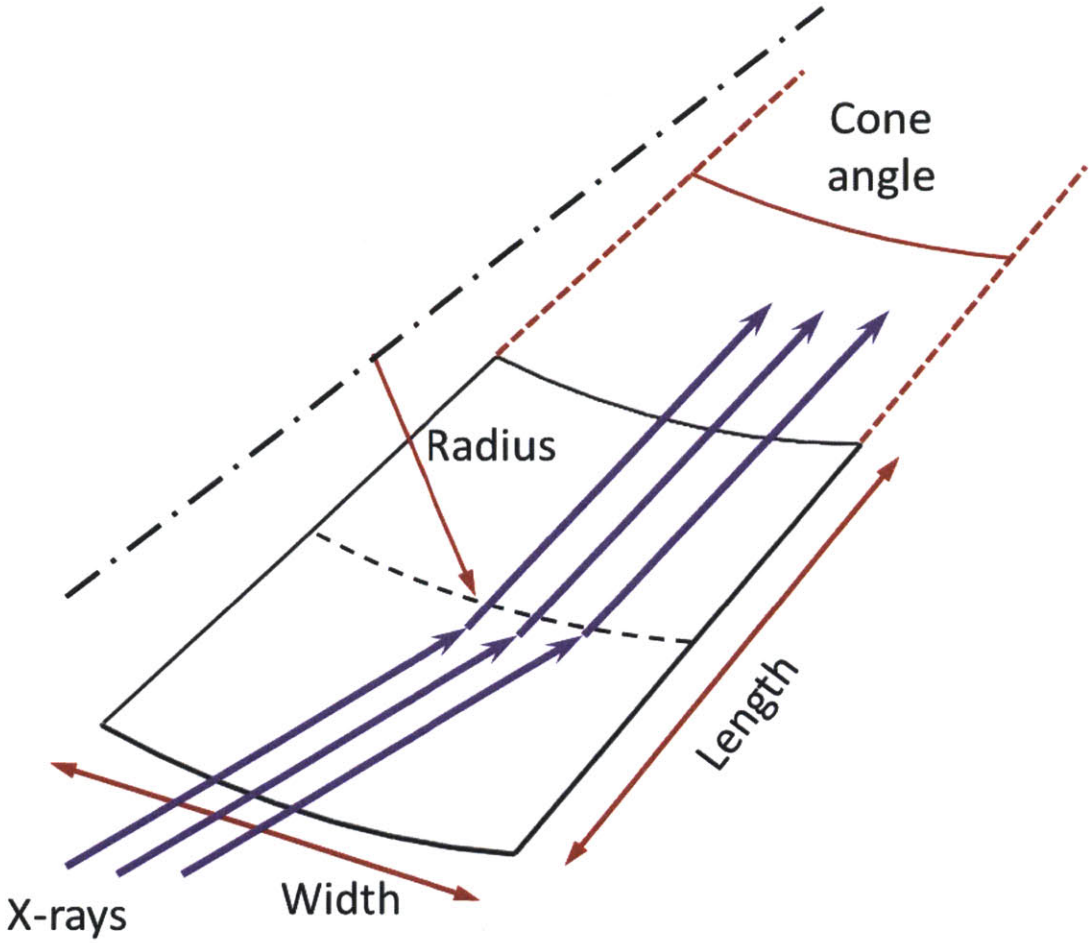

Figure 5.1 Important dimensions of mirror model.

Table 5.1 Important dimensions of the modeled substrates

Radius	200 mm; 500 mm; 1000 mm
Mirror length	200 mm
Mirror width (arc length)	200 mm
Cone angle	15 mrad
Mirror thickness	400 μm
Mirror material	D-263 glass
Elastic modulus	72.9 GPa
Poisson's ratio	0.208

5.2.2 Finite element model

ADINA is used as the finite element code in this work. This program makes interfacing between Matlab and the finite element simulation relatively simple, resulting in a very flexible simulation system.

For this work, the parabolic or hyperbolic prescriptions, which deviate by only a few microns from a conical figure, are neglected. Thus, a conical mirror shape is used. Since the thickness of the plate is small relative to the width or length of the mirror, shell elements are used in the finite element mesh. In addition, since deflections are also on the order of 1 micron, the model assumes small deflections. This is warranted since deflections are much smaller than the thickness of the mirror [54].

As a result of assuming small deflections, the model is assumed to be linear. Thus, a change in mirror shape induced by surface stress is identical (only opposite in sign) to an elimination of that same surface shape. This greatly simplifies the simulations since the mirror model only needs to be a perfect conical shape, and shape corrections may be defined later, after influence functions have been generated.

In order to simulate the growth or contraction of a stressed surface layer, a second shell, offset from the substrate, is bound to the substrate surface. This 'stressed layer' shell, with a fixed thickness of 1 μm, is given a coefficient of thermal expansion such that a temperature change of 1 Kelvin results in a stress of 1 N/m. Thus, only the temperature of this layer needs to be changed to apply stresses to the surface. For simplicity in modeling, negative stresses applied to this layer are taken as equivalent to positive stresses applied to the opposite surface of the substrate.

A rectangular mesh, 81 x 41 elements of 4-node shell elements, shown in Figure 5.2, is used to describe both the substrate and the stressed layer. Each element therefore represents about a 2.5 mm x 5 mm area. A kinematic set of boundary conditions (Kelvin type II constraints [55]) is used to allow free deformation of the mirror, while constraining all 6 degrees of rigid-body motion. Any set of 6 non-redundant constraints could be used here.

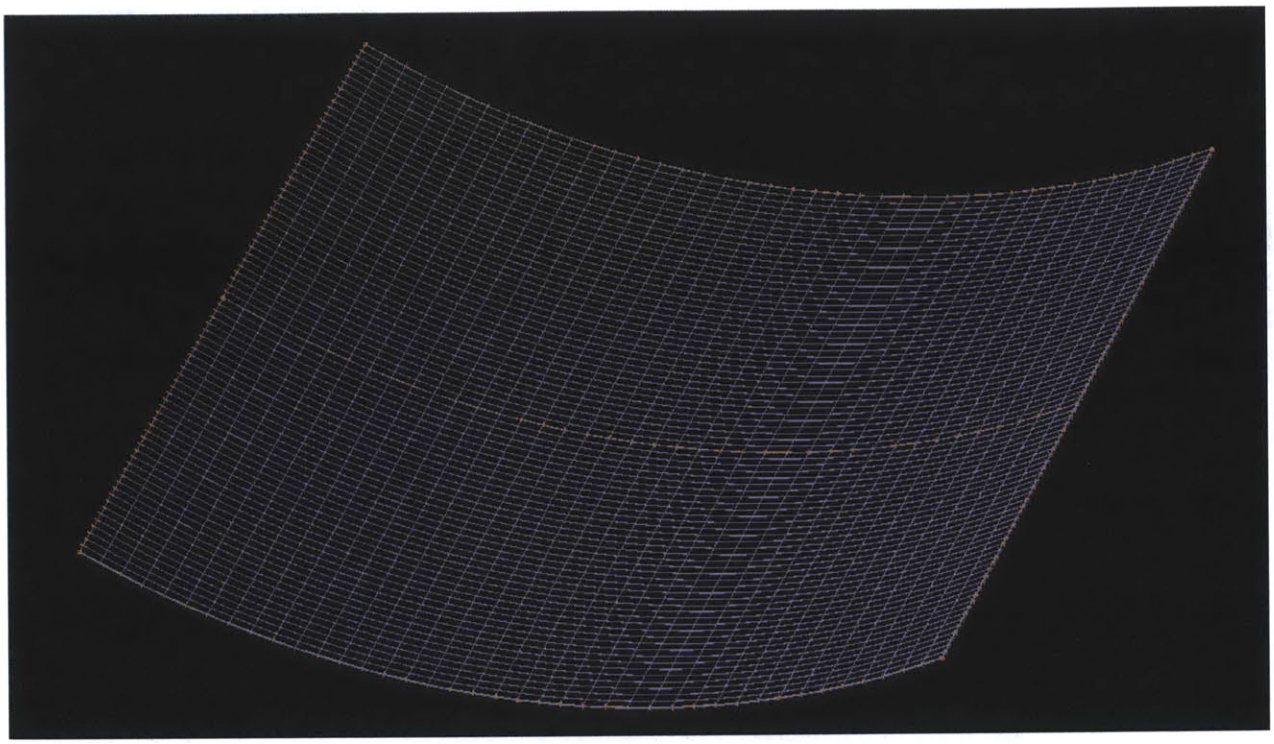

Figure 5.2 Example of a mesh used in the finite element model. R = 200 mm in this image.

To apply stress to the surface of the substrate, the stressed layer shell temperature is changed at the desired nodes, through the use of a batch file edited by Matlab and called by ADINA. For example, to measure an influence function, a batch file is created by a Matlab script where the temperature of a single node is set to 1 K (corresponding to 1 N/m). The batch file is read by ADINA, and the simulation is run, resulting in the deflection from that one node stress. Example batch files are included in Appendices A.2 and B.1. An example influence function is shown in Figure 5.3.

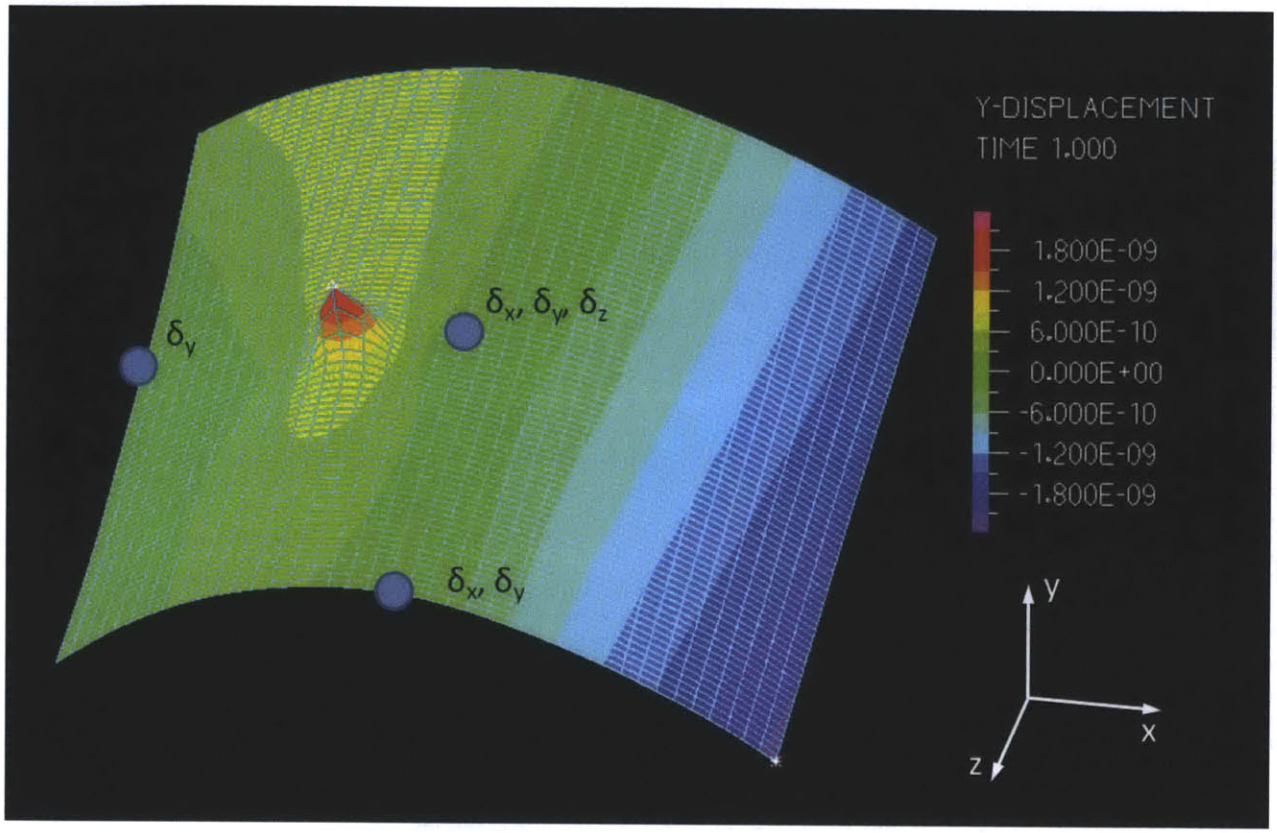

Figure 5.3 Plot of an influence function resulting from a 1 N/m stress applied at a single node. Also shown are the three constraints and the directions of translations that are constrained.

5.2.3 Control script

Matlab was used to control the large set of simulations run by ADINA, and to solve the constrained least squares problem to find the stress distribution resulting in the lowest figure error. The Matlab functions used are included in Appendix B.

Matlab was also used to define the desired figure change. In this work, the figure change consists of the sum of three Legendre polynomials. Legendre polynomials are convenient descriptors of figure errors for near-cylindrical mirrors [56], in part due to orthogonality between any two Legendre polynomials over a rectangular area. The desired shape change for all work in this chapter is shown in Figure 5.4. It is important to note that the boundary conditions of the desired shape change must be modified to match those of the finite element model. This figure change was chosen because it represents a change in curvature along the axial (Z) direction, which is expected to be most challenging.

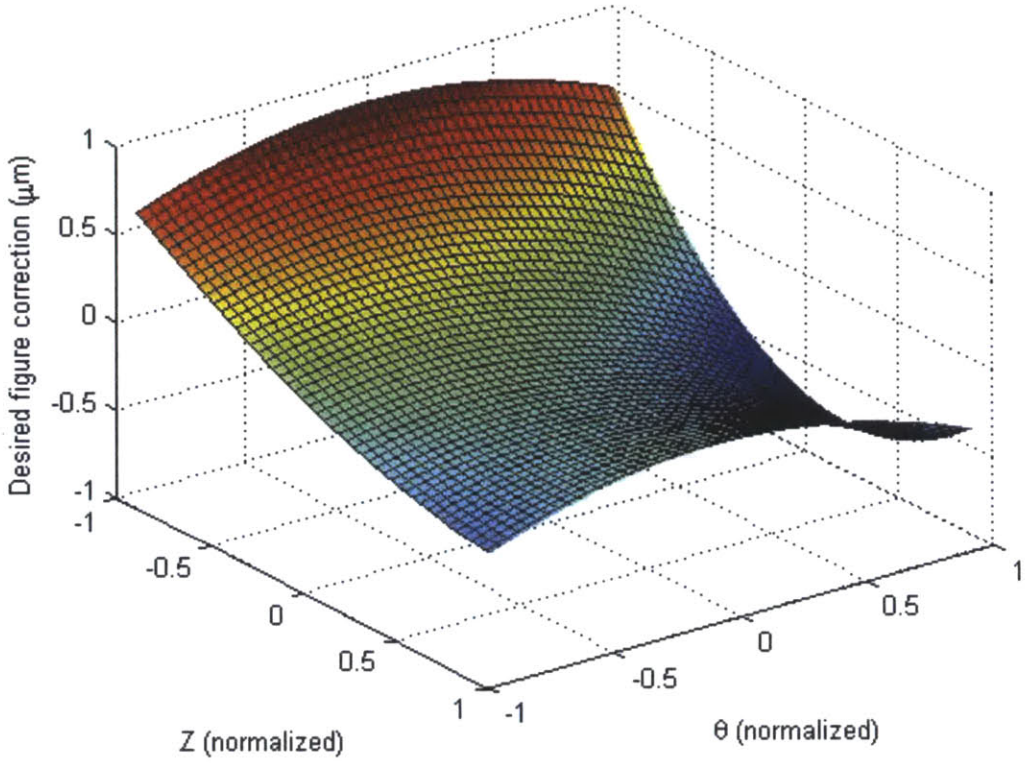

Figure 5.4 Desired change in figure for all simulations in this chapter. This is a sum of three Legendre polynomials.

5.2.4 Consideration of Legendre polynomial test functions

In Section 3.3.1, Zernike polynomials were successfully used to rapidly simulate correction of flat optics. Zernike polynomials do not exhibit orthogonality over a rectangular pupil, so they are inappropriate for near-cylindrical optics. Legendre polynomials were originally considered as a replacement to the Zernike polynomials as test functions. However, using Legendre polynomials resulted in very incomplete figure correction, where the RMS slope error was reduced no more than 20%, even using almost 100 Legendre polynomials as test functions.

Instead, influence functions from stress at each individual node (which requires about 3300 finite element simulations, compared to 100 simulations as required by the Legendre polynomial approach), resulted in much more effective correction of the optics. Thus, the Legendre polynomial approach was abandoned.

5.3 Results

Significant improvement in figure may be achieved with simulated ion implantation, even when imposing constraints on the maximum stress that can be applied. An example of the stress distribution required to correct the figure error in Figure 5.4, with a constraint on the maximum stress as 150 N/m, is shown in Figure 5.5. This particular example is for a substrate radius of 200 mm, and the correction is from an estimated half-power diameter (HPD) of 6 arc seconds to 3.5 arcseconds, a reduction factor of about 2:1. This radius is one of the most challenging to correct.The residual slope error of this same substrate is plotted in Figure 5.6, and shows that the residual error is concentrated at the edges. This is also where the highest stress is required.

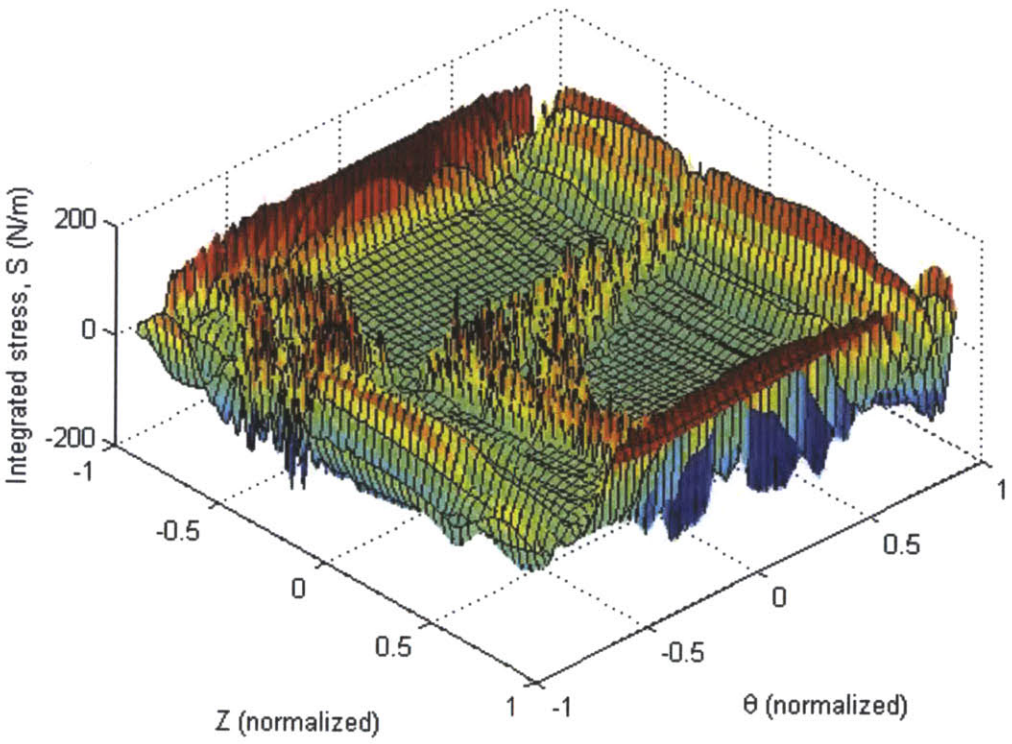

Figure 5.5 Stress required to correct the figure shown in Figure 5.4, while keeping the maximum stress below 150 N/m. This is for a substrate radius of 200 mm

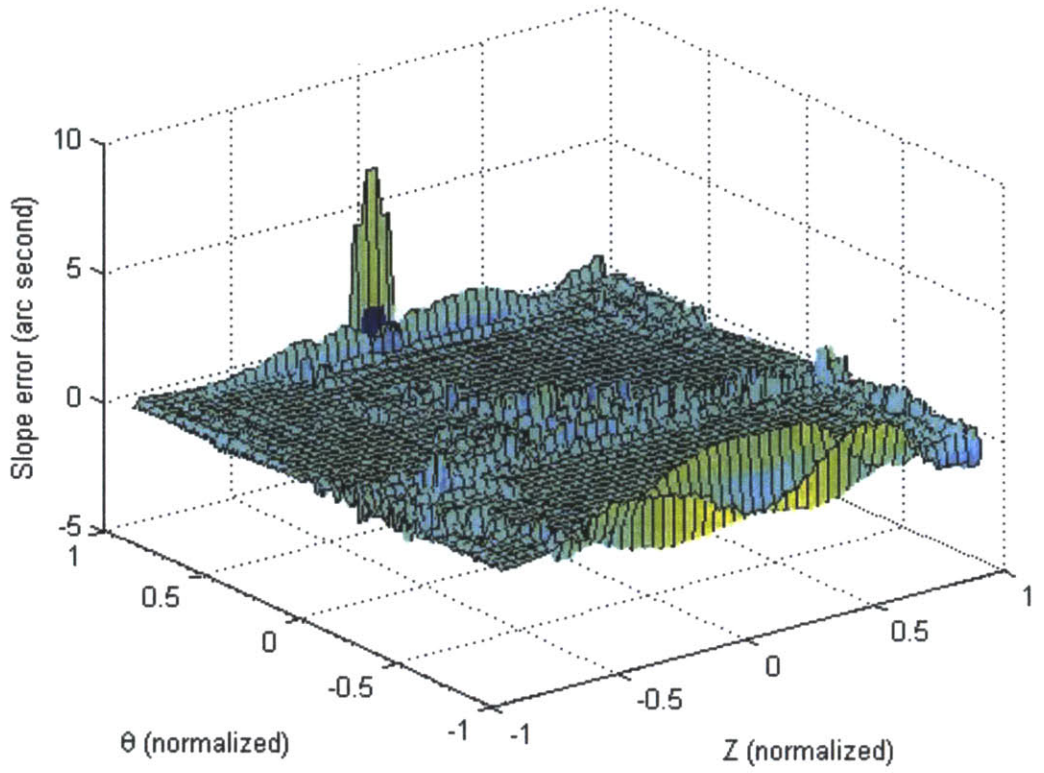

Figure 5.6 Residual slope error for a substrate with a radius of 200 mm and a stress limit of 150 N/m. The errors are concentrated at the edges.

One of the most important results is the residual half-power diameter (HPD) of the point spread function of a telescope's optics. Accurately calculating the HPD requires detailed knowledge of both reflecting surfaces' figure and alignment, and requires ray tracing. This is impractical for this study, as well as for error budgeting. Instead, an approximation is used here, as in [57], to give a sense of how much of an impact on HPD ion implantation may have.

$$HPD \approx 3.84 * \varepsilon\theta_{RMS} \qquad \textbf{Equation 5.1}$$

Here, $\varepsilon\theta_{RMS}$ is the root mean square of the slope error of the surface. This approximation assumes that: slope errors follow a Gaussian distribution; the primary and secondary mirror errors are uncorrelated; and azimuthal errors are relatively unimportant. Figure 5.7 shows the residual HPD for the three substrate radii studied, at all integrated stress limits studied. This figure shows that the most challenging

substrates to correct are those with the smallest radius. Ion implantation may significantly reduce HPD for large radius substrates. Figure 5.8 shows the same information but in terms of the HPD reduction factor. Again, for the larger-radius substrates, the correction is quite significant, but for the small-radius substrate it is not great. The HPD reduction factor appears to drop when the stress constraint is high. This may be a result of the large element size used in this study, or it may highlight a necessity to choose a more robust optimization algorithm. However, the trend in residual HPD shown in Figure 5.7 is clear, and this is sufficient for our current purpose.

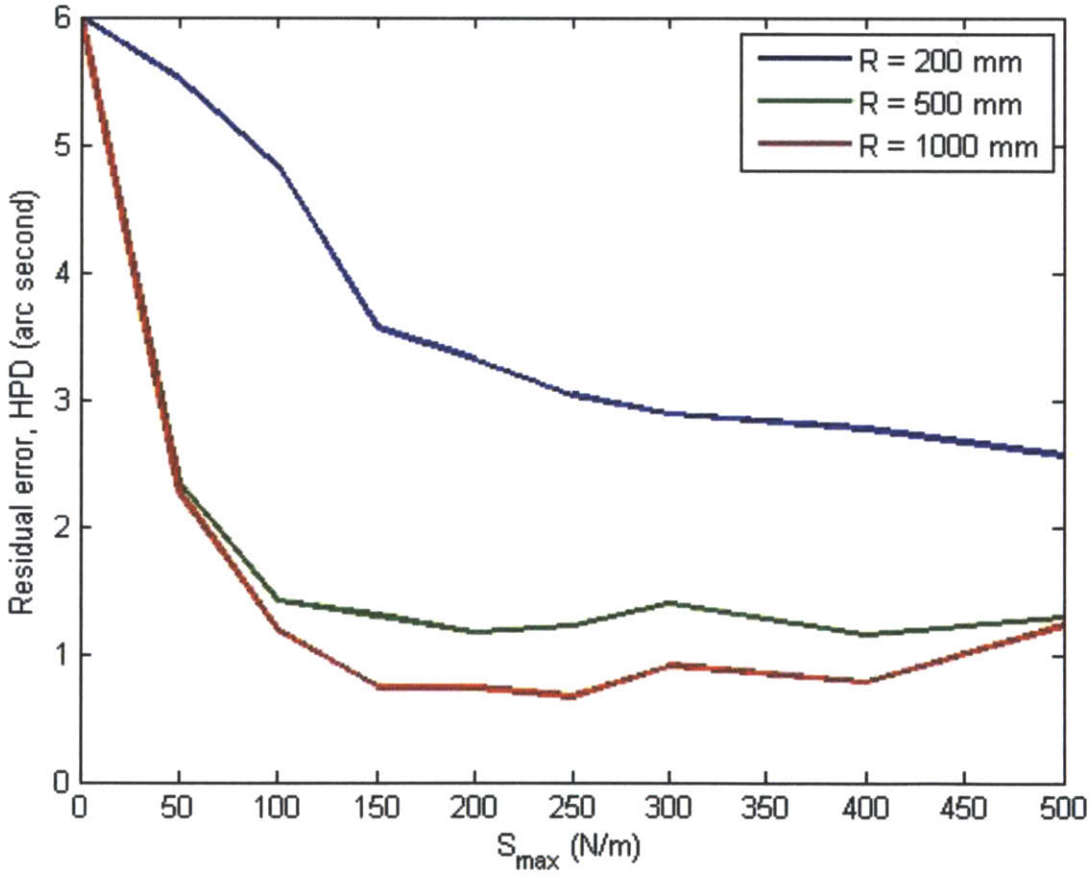

Figure 5.7 Residual estimated HPD error for different substrate radii and different stress limits. The small radius of 200 mm is most difficult to correct.

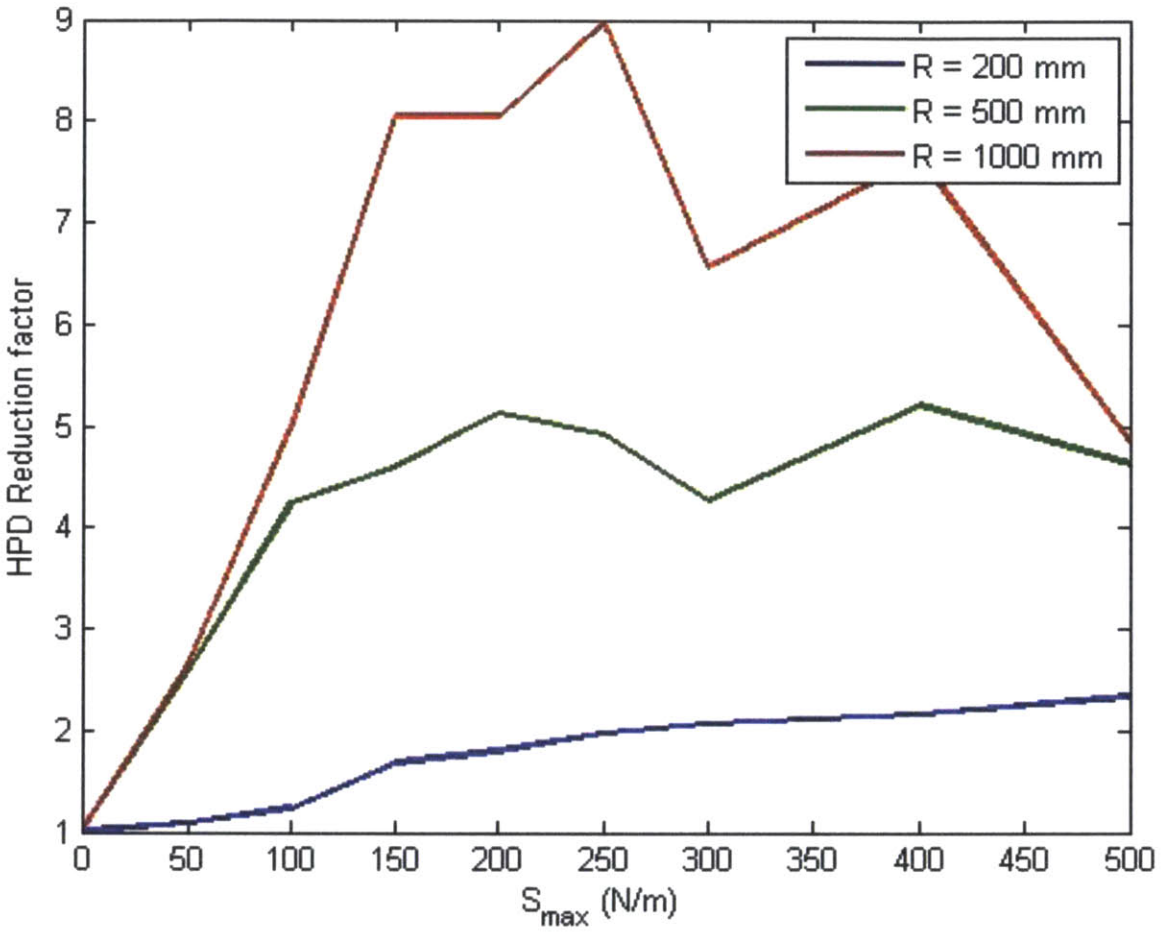

Figure 5.8 HPD reduction factor for different substrate radii and different stress limits.

The correction may also be more complete for thinner glass, such as the 200 μm thickness used for the NuStar Observatory, since for a given magnitude of integrated stress, the change in curvature scales with the square of the thickness. Halving the substrate thickness to 200 μm would be the same as quadrupling the stress limit; for substrates with a small radius of curvature, this could have a significant impact.

6 Conclusions and future work

In this work, we have demonstrated that ion implantation is a feasible method of conducting figure correction of x-ray telescope mirrors. This is an important technology because current methods of making x-ray telescope mirrors are not accurate enough for high-resolution, large effective-area x-ray telescopes. We have shown that ion implantation allows figure correction by inducing a near-surface stress in a substrate; the magnitude and location of this stress may readily be controlled to change the curvature of the substrate as necessary to correct figure errors.

We have shown in Chapter 2 that stress in silicon and glass substrates is a function of ion fluence, and we have discussed the causes of this stress. *In-situ* curvature measurements provide a powerful method of studying the stress induced by ion implantation. We have also introduced the concept of the 'damage thickness,' which suggests a way to increase the stress in silicon substrates beyond what has been observed. Future work should focus on achieving high stress in glass substrates, and on the effects of implanting through reflective layers.

In Chapter 3, we used the data gathered in Chapter 2 to perform figure corrections on silicon substrates. Correction of spherical curvature was successful in many samples, although it is clear that further effort should be expended on understanding which process parameters are most important for repeatability. We also described a masking method of figure correction for non-spherical figure errors, and demonstrated this method by attempting to correct astigmatism in a silicon wafer. While we observed a change in astigmatism only, the magnitude of this change was far too low to fully correct that figure error.

We also demonstrated, in Chapter 4, that ion implantation has no detrimental effect on either shape stability or surface roughness. We conducted x-ray reflectivity measurements using a Cu-Kα x-ray source, and found no significant effect on the x-ray reflectivity curves from ion implantation. This is a

critically-important result, that otherwise would have precluded the use of this method for figure correction of x-ray telescope mirrors. We also measured the stability of the mirror figure over time and after thermal cycling, and found no consistent evidence of relaxation. Both of these issues—surface roughness and figure stability—should be monitored since any change in process parameters, coatings, or substrate material could result in either roughening or figure instability.

Finally, we simulated correction of near-conical mirrors (such as used in a Wolter type I design), and found that these mirrors are indeed possible to correct, even when realistic limits on integrated stress are imposed. This is an important result that suggests that ion implantation may provide significant reduction in figure errors. Further simulations, with a finer mesh, should be conducted. In addition, these studies should be extended to guide the definition of functional requirements for an ion implanter that can correct such mirrors.

Ion implantation has the potential to enable significant advances in x-ray astronomy by enabling the fabrication of highly accurate thin mirrors for high-resolution, large effective-area x-ray observatories. Substantial work remains in implementing ion implantation for figure correction of thin mirror substrates, but this thesis demonstrates that this method is feasible and should be pursued further.

Appendix A MATLAB/ADINA code for figure correction of flat substrates

This appendix includes the functions important to calculating the required stress distribution. Not all functions are included here, since many are used for plotting, re-shaping data, etc. and are not important to understanding the features of this method of solution.

A.1 ADINA substrate input batch file: SiDisk.in

```
database new save=no prompt=no
feprogram adina
heading 'Ion implantation of silicon wafer'
*
control updatethickness=no
master idof=000100
system name=1 type=cylindrical
*
printout input-data=1 displacements=yes velocities=no accelerations=no
print-steps
entries block first last increment
1 1 1 1
dataend

*
* Define geometry
*
coordinates point system=1
entries name r theta xl
1       0       0       0
2       .05     300     0
3       .05     90      0
4       .05     240     0
dataend
*
*line arc name=1 mode=1 2 3 center=1
*line arc name=2 mode=1 4 3 center=1
*line arc name=3 mode=1 4 2 center=1
line straight name=1 p1=1 p2=2
*
*surface patch name=1 1 2 3 0
surface revolved name=1 mode=axis line=1 angle=300 system=1 axis=xl
surface revolved name=2 mode=axis line=3 angle=60 system=1 axis=xl
transformation translation name=3 mode=system dx=0.00020193
surface transformed name=3 parent=1 transformation=3 pcoincide=yes
surface transformed name=4 parent=2 transformation=3 pcoincide=yes
*
sfthickness
entries name thick
1 2.66e-7
2 2.66e-7
3 0.000403595
4 0.000403595
```

```
dataend
*
printnodes surfaces
entries surface
1
2
dataend

*
* Apply boundary conditions
*
fixity XYZT
'x-translation'
'y-translation'
'z-translation'
dataend
fixboundary points XYZT
1
dataend
*
fixity XT
'x-translation'
dataend
fixboundary points XT
2
4
dataend

*
* Define material
*
material elastic 1 e=1.8e11 nu=0.27 alpha=2.6e-6
*
* Define element groups
*
kinematics displacements=small
egroup shell name=1 material=1 thickness=2.66e-7
egroup shell name=2 material=1 thickness=.000403595
*
* Subdivide surfaces
*
subdivide surface name=1 mode=length size=0.001570796327
2
3
4
dataend
*
* Mesh surfaces
*
gsurface name=1 nodes=4 group=1 meshing=free-form method=delaunay
2
dataend
gsurface name=3 nodes=4 group=2 meshing=free-form method=delaunay
```

```
4
dataend
*meshing=free-form method=delaunay
* Make rigid links between surfaces
*
rigidlink name=1 slavetype=surface slavename=3 mastertype=surface mastername=1 option=1
rigidlink name=2 slavetype=surface slavename=4 mastertype=surface mastername=2 option=1
*
* Save file
*
adina file='SiDisk.dat'
database save permfile='SiDisk.idb'
```

A.2 ADINA temperature input batch file: SiDiskTemps.in *(abbreviated)*

```
database open file='SiDisk.idb' save=no
printout input-data=4 displacements=yes velocities=no accelerations=no
delete apply temperatures
apply temperature
entries node factor
1 9.444560e+01
2 7.944567e+01
3 6.566542e+01
...
...
3057 -1.170116e+01
3058 2.237555e+01
3059 -8.945255e+00
dataend
adina file='SiDisk.dat'
database save permfile='SiDisk.idb'
```

A.3 MATLAB script: controlscript.m

```
% controlscript.m
% by Brandon Chalifoux
% Last updated: 8/1/2013
%
% Calls all sub-functions to run batch files in ADINA for a set of test
% functions. Then solves least-squares problem to find best-fit stress
% distribution to match desired surface figure.

%% Initialize ADINA and get node locations
clear all; clc
nodes = ADINA_init;
N=66; % number of zernikes to use when describing shapes
M=20; % number of zernikes to test for

%% repeat for each zernike input
for i=1:M
   tic
```

```
    % Generate temperature batch file
    gen_tBatch(i, 1, nodes, 'SiDiskTemps.in');

    % Run solution
    data = ADINA_run(nodes);

    % scale results and decompose to get b coefficients
    b(:,i) = decomp_data(data,N);
    toc
end

%% plot input-output for zernike i
i = 12;
% plot input dose
figure;
subplot(1,5,1)
plot_zern(i,1,['Dose distribution Noll = ' num2str(i)]);
view(2)

% plot input in zernike space
subplot(1,5,2)
b_in = zeros(M,1); b_in(i) = 1;
plot([1:M],b_in,'o')

% plot output shape
subplot(1,5,4)
plot_zern([1:N]',b(:,i)',['Resulting shape Noll = ' num2str(i)]);
view(2)

% plot output in zernike space
subplot(1,5,5)
plot([1:N],b(:,i),'o')

%%
% define desired surface shape
noll = [5 6]';
mag = [-.223 .394]'*1e-6;
r_b = [0 1 1]';
theta_b = [0 -pi/3 -2*pi/3]';
% Define the desired surface shape, matching boundary conditions
[c noll_ref mag_ref] = def_refshape(noll,mag,N,r_b,theta_b);
figure;

% Plot the desired surface shape
[Y_ref Z_ref X_ref] = plot_zern(noll_ref,mag_ref,'Reference shape');

% solve least squares problem to determine 'a' vector
a = (b'*b)\b'*c;

% construct input stress function
gen_tBatch([1:length(a)],a,nodes, 'SiDiskTemps.in');
```

```
% Run solution
data_out = ADINA_run(nodes);

% scale results and decompose to get b coefficients
% This should be close to c coefficients
b_out = decomp_data(data_out,N);
figure;
[Y_out Z_out X_out] = plot_zern([1:N]',b_out','Deformed shape');

%Calculate rms error and plot error
RMS_error = sqrt(mean(mean((X_out(isfinite(X_out))-X_ref(isfinite(X_ref))).^2)));
error_title = ['Shape error for noll = ', mat2str(noll'),': RMS error = ', num2str(RMS_error)];
plot_zern([1:N]',(b_out-c)',error_title);

% Plot zernike coefficients
figure;
hold on; plot(b_out,'o'); plot(c,'x');
title (['Zernike coefficients for noll = ', mat2str(noll')]);
figure;
plot(a,'o'); title(['Best fit stress field for noll = ', mat2str(noll')]);

figure;
[Y_in Z_in T_in] = plot_zern([1:M]',-a','Implant temperature');

% Calculate dose
figure;
A = 1.3172e-3;
B = 1.3560e5;
E = 1.8e11; nu = 0.27; alpha = 2.6e-6;

Dose = A*(E*alpha/(1-nu)*T_in).^2.*sign(T_in) + B*E*alpha/(1-nu)*T_in;
surf(Y_in,Z_in,Dose)
title('Implant Dose (ions/cm^2)');
xlabel('Y'); ylabel('Z'); zlabel('Dose');
disp(['Implanted dose = ' num2str(max(max(Dose)))]);

%% plot input-output for final solution
% plot input dose
figure;
subplot(1,5,1)
plot_zern(noll_ref,mag_ref,['Desired shape']);
view(2)

% plot input in zernike space
subplot(1,5,2)
plot([1:N],c,'o')

% plot dose distribution
subplot(1,5,3)
plot([1:M],a,'o')
```

```
% plot output shape
subplot(1,5,4)
plot_zern([1:N]',b_out','Resulting shape');
view(2)

% plot output in zernike space
subplot(1,5,5)
plot([1:N],b_out,'o')
```

A.4 MATLAB function: ADINA_Init.m

```
% ADINA_init.m
% by Brandon Chalifoux
% Last updated: 8/1/2013
%
% Initializes ADINA by running a batch file with no stress input, in order
% to get node locations

function nodes = ADINA_init()

clear all
clc
fclose('all');
files = ['SiDisk.idb', 'SiDisk.dat', 'SiDisk.out'];
for i=1:length(files)
  if exist(files(i))==2
    delete(files(i));
  end
end

% Run ADINA to load finite element model
!c:\adina88\x64\aui.exe -b -m 20mb SiDisk.in
while exist('SiDisk.idb')==0, end

% Run ADINA and wait for output to be printed
!c:\adina88\x64\adina.exe -b -s -mm 100mw -t 1 SiDisk.dat
while exist('SiDisk.out')==0, end

% Read node locations from .out file
fid = fopen('SiDisk.out');
C = textscan(fid, '%f %d %d %d %d %d %d %d %d %d %d %d %d %d %f %f %f %d %d', 6118, 'Delimiter',' ',
'MultipleDelimsAsOne',1, 'HeaderLines',792, 'CollectOutput',1);
nodes = [C{1,1}, C{1,3}(:,1:3)];
r = [2:2:6118]';
[nodes,PS]=removerows(nodes,'ind',r);
fclose(fid);

end
```

A.5 MATLAB function: ADINA_run.m

```
% ADINA_run.m
% by Brandon Chalifoux
% Last updated: 8/1/2013
%
% Runs ADINA using main SiDisk.in and SiDiskTemps.in batch files to get
% shape response from a stress input

function data = ADINA_run (nodes)
% Run Solution with defined temperature loading

% Run temperature batch file and wait until .dat file is ready
if exist('SiDisk.dat')==2, delete('SiDisk.dat'); end
!c:\adina88\x64\aui.exe -b -m 20mb SiDiskTemps.in
while exist('SiDisk.dat')==0, end

% Run ADINA and wait for output to be printed
!c:\adina88\x64\adina.exe -b -s -mm 100mw -t 1 SiDisk.dat
while exist('SiDisk.out')==0, end


% Read result data
% tic
%%%%%% should automate detection of proper nodes and data %%%%%%%
fid = fopen('SiDisk.out');
C = textscan(fid, '%f %f %f %f %f %f %f %s %s', 42, 'Delimiter',' ', 'MultipleDelimsAsOne',1, 'HeaderLines',176,
'CollectOutput',1);
data=[C{1,1}(:,1:7)];
for i = 1:64
   C = textscan(fid, '%f %f %f %f %f %f %f %s %s', 47, 'Delimiter',' ', 'MultipleDelimsAsOne',1, 'HeaderLines',11,
'CollectOutput',1);
   data=[data; C{1,1}(:,1:7)];
end
C = textscan(fid, '%f %f %f %f %f %f %f %s %s', 9, 'Delimiter',' ', 'MultipleDelimsAsOne',1, 'HeaderLines',11,
'CollectOutput',1);
data=[data; C{1,1}(:,1:7)];
fclose(fid);

% update node Y and Z positions
data(:,3) = data(:,3) + nodes(:,3);
data(:,4) = data(:,4) + nodes(:,4);

end
```

A.6 MATLAB function: gen_tBatch.m

```
% gen_tBatch.m
% by Brandon Chalifoux
% Last updated: 8/1/2013
%
```

```
% Generates a temperature batch file, SiDiskTemps.in, which is read by ADINA
% to apply stress to the surface of the substrate

function gen_tBatch(noll, mag, nodes, filename)
%GEN_TBATCH Generate temperature load input batch file for use with ADINA
% GEN_TBATCH(NOLL, MAG NODES, FILENAME) generates a batch file to apply
% temperature load in ADINA based on a sum of input Zernike functions
% defined by NOLL and MAG.
%
% NOLL is a vector of Noll indices of Zernike functions, and MAG is a
% vector of the magnitude of each function. Temperature values are
% determined at the nodes specified by NODES, a Nx4 array from the FE
% model: [node x y z].
%
% The batch file is written to FILENAME, which is a string.
% checks
% check filename. If it doesn't end in '.in', append '.in'.
% Open existing file if it exists. If not, make new file.
header = {'database open file="SiDisk.idb" save=no';
   'printout input-data=4 displacements=yes velocities=no accelerations=no';
   'delete apply temperatures';
   'apply temperature';
   'entries node factor'};
footer = {'dataend';
   'adina file="SiDisk.dat"';
   'database save permfile="SiDisk.idb"'};
T = zeros(size(nodes,1),2);
T(:,1) = nodes(:,1);
[theta r] = cart2pol(nodes(:,3),nodes(:,4));
r = r / max(r); %scale so r <= 1
% Set up noll index
if max(noll) > 105
   error(['The maximum number of coefficients allowed for ',order,' is 105, but max. specified=',int2str(M)]);
else
   n = [0, 1, 1, 2, 2, 2, 3, 3, 3, 3, 4, 4, 4, 4, 4, 5, 5, 5, 5, 5, 5, 6, 6, 6, 6, 6, 6, 6, 7, 7, 7, 7, 7, 7, 7, 7, 8, 8, 8, 8, 8, 8, 8, 8,
9, 9, 9, 9, 9, 9, 9, 9, 9,10,10,10,10,10,10,10,10,10, 10, 10,11,11,11,11,11,11,11,11,11,11, 11,
11,12,12,12,12,12,12,12,12,12, 12,12, 12,12,13,13,13,13,13,13,13,13,13,13, 13, 13, 13, 13];
   m = [0, 1,-1, 0, 2,-2,-1, 1,-3, 3, 0,-2, 2,-4, 4, 1,-1, 3,-3, 5,-5, 0, 2,-2, 4,-4, 6,-6,-1, 1,-3, 3,-5, 5,-7, 7, 0,-2, 2,-4, 4,-6,
6,-8, 8, 1,-1, 3,-3, 5,-5, 7,-7, 9,-9, 0, 2,-2, 4,-4, 6,-6, 8,-8, 10,-10,-1, 1,-3, 3,-5, 5,-7, 7,-9, 9,-11, 11, 0,-2, 2,-4, 4,-6, 6,-8,
8,-10,10,-12,12, 1,-1,-3, 3, 5,-5, 7,-7, 9,-9, 11,-11, 13,-13];
end

for i = 1:length(noll)
   T(:,2) = T(:,2) + mag(i)*zernfun(n(noll(i)),m(noll(i)),r,theta);
end
fid = fopen(filename,'w');
fprintf(fid,'%s\r\n',header{:});
fprintf(fid,'%d %d\r\n',T');
fprintf(fid,'%s\r\n',footer{:});
fclose(fid);

end
```

Appendix B: MATLAB/ADINA code for figure correction of near-conical substrates

This appendix includes the functions important to calculating the required stress distribution. Not all functions are included here, since many are used for plotting, re-shaping data, etc. and are not important to understanding the features of this method of solution. In addition, SiDiskTemps.in, ADINA_init.m, ADINA_run.m, and gen_tBatch.m are largely the same as in Appendix A, and are not repeated here. However, there some notable differences between the code here and that for flat substrates. In particular, influence functions did not rely on Legendre or Zernike Polynomials for test functions, but instead stress applied at one node only. In addition, constrained least squares problems are solve here instead of unconstrained least squares problems.

B.1 ADINA substrate input batch file: SiDisk.in

```
database new save=no prompt=no
feprogram adina
heading 'Ion implantation of D263 segmented Wolter I'
*
control updatethickness=no
master idof=000000
system name=1 type=cylindrical mode=1 AX=0 AZ=1
*
printout input-data=1 displacements=yes velocities=no accelerations=no
print-steps
entries block first last increment
1 1 1 1
dataend

*
* Define geometry
* ALL DIMENSIONS IN METERS
*
coordinates point system=1
entries name r theta xl
* Axis points
1       0       0       0
2       0       0       0.100
3       0       0       -0.100
* Substrate centerline points
4       0.20175 0       0
5       0.20175 28.65   0
6       0.20175 -28.65  0
7       0.200   0       0.100
8       0.200   28.65   0.100
9       0.200   -28.65  0.100
10      0.2035  0       -0.100
```

```
11      0.2035  28.65   -0.100
12      0.2035  -28.65  -0.100
* Implant layer points
13      0.20195 0       0
14      0.20195 28.65   0
15      0.20195 -28.65  0
16      0.2002  0       0.100
17      0.2002  28.65   0.100
18      0.2002  -28.65  0.100
19      0.2037  0       -0.100
20      0.2037  28.65   -0.100
21      0.2037  -28.65  -0.100
dataend
*
* Substrate lines
line arc name=1 mode=2 5 6 4
line straight name=2 6 9
line arc name=3 mode=2 9 8 7
line straight name=4 8 5

line straight name=5 5 11
line arc name=6 mode=2 11 12 10
line straight name=7 12 6

* Implant layer lines
line arc name=8 mode=2 14 15 13
line straight name=9 15 18
line arc name=10 mode=2 18 17 16
line straight name=11 17 14

line straight name=12 14 20
line arc name=13 mode=2 20 21 19
line straight name=14 21 15

* Substrate mid-surfaces
surface patch name=1 1 2 3 4
surface patch name=2 1 5 6 7

* Implant layer surfaces
surface patch name=3 8 9 10 11
surface patch name=4 8 12 13 14

*
sfthickness
entries name thick
1 0.000399
```

```
2 0.000399
3 0.000001
4 0.000001
dataend
*
printnodes surfaces
entries surface
1
2
dataend

*
* Create and apply boundary conditions
*
* Create boundary conditions
fixity XYZT
'x-translation'
'y-translation'
'z-translation'
dataend

fixity YT
'y-translation'
dataend

* Apply boundeary conditions
fixboundary points XYZT
4
dataend

fixboundary points YT
5
7
dataend

*
* Define material
*
material elastic 1 e=72.9e9 nu=0.208 alpha=1.086e-5

*
* Define element groups
*
kinematics displacements=small
egroup shell name=1 material=1 thickness=0.000399 printvectors=2
egroup shell name=2 material=1 thickness=0.000001 printvectors=2
```

```
*
* Subdivide surfaces
*
subdivide surface name=1 mode=divisions ndiv1=40 ndiv2=40
1
2
3
4
dataend

*
* Mesh surfaces
*
gsurface name=1 nodes=4 group=1
1
2
dataend
gsurface name=3 nodes=4 group=2
3
4
dataend

*
* Make rigid links between surfaces
*
rigidlink name=1 slavetype=surface slavename=3 mastertype=surface mastername=1 option=1
rigidlink name=2 slavetype=surface slavename=4 mastertype=surface mastername=2 option=1

*
* Save file
*
adina file='WolterOptic.dat'
database save permfile='WolterOptic.idb'
```

B.2 MATLAB script: controlscript.m *(abbreviated)*

```
% controlscript.m
% by Brandon Chalifoux
% Last updated: 8/10/2014
%
% Calls all sub-functions to run batch files in ADINA for a set of test
% functions. Does not solve least-squares problems; only collects influence
% function results.

%% Compute results for R200
cd('R200');
% Initialize ADINA and get node locations
clear all;
clc
fileName = 'WolterOptic';
nodes = ADINA_init(fileName);
nodes_substrate = nodes(1:size(nodes,1)/2,:);
nodes_implant = nodes(size(nodes,1)/2+1:size(nodes,1),:);
L = 0.200; % length of optic, m

% Input each test function
% Currently set up for measuring influence functions to gaussian
% distributions
 M=81; % number of nodes along z direction
N=41; % number of nodes along theta direction
drLibrary = zeros(M*N,M*N);
tictocVect = zeros(length(nodes_implant(:,1)),1);
mag = 1; % Set magnitude of stress input, N/m
% Apply test function at each node
for i = 1:length(nodes_implant(:,1))
   tic
   % Generate temperature batch file
   gen_tBatch(i, mag, nodes_implant, 'WolterOpticStress.in');
   % Run solution
   data = ADINA_run(nodes_substrate,fileName);
   drLibrary(:,i) = ((data(:,8)+data(:,2)).^2+(data(:,9)+data(:,3)).^2).^.5-(data(:,8).^2+data(:,9).^2).^.5;
   tictocVect(i) = toc;
   disp(['t' num2str(i) '=' num2str(tictocVect(i))])
end
disp('finding pinv of drLibrary...')
pinv_drLibrary = pinv(drLibrary);
tavg = mean(tictocVect);
% Save workspace!
save('WolterR200M41N81.mat');

% Define desired shape and calculate required stress distribution, for multiple stress constraints
% define desired shape change
SmaxVect = [50 100 150 200 250 300 400 500 1000];
for j = 1:length(SmaxVect)
   load('WolterR200M41N81.mat','drLibrary','nodes_substrate','nodes_implant','fileName','L');
   % Define legendres for desired shape change
   c = zeros(16,16);
```

```
    c(3,1) = 1.5e-6*0.2122;
    c(1,3) = -1e-6*0.2122;
    c(3,2) = 1e-6*0.2122;
    % Define boundary nodes (dirichlet boundary conditions)
    boundNodes = [0 0; 0 1; 1 0];
    cDesShape = defDesShape(c,boundNodes);
    cVect = reshape(cDesShape',[],1);
    % Calculate desired figure change
    drDes = calcLegendre(cVect,nodes_substrate);

    % solve unconstrained least squares problem for initial guess of
    % constrained least squares
    stressLS0 = pinv_drLibrary*drDes;

    % Solve using constrained least squares
    Smax = SmaxVect(j); % N/m
    ub = Smax*ones(M*N,1);
    lb = -ub;
    options = optimoptions(@lsqlin,'TolFun',1e-32,'MaxIter',1000);
    tic
    stressLS = lsqlin(drLibrary,drDes,[],[],[],[],lb,ub,stressLS0/100,options);
    disp(['t_lsqlin = ' num2str(toc)])

    % Input best fit stress to model to check results
    % Generate temperature batch file
    gen_tBatch(0, stressLS, nodes_implant, 'WolterOpticStress.in');

    % Run solution
    data = ADINA_run(nodes_substrate,fileName);

    % Calculate slope (dR/dx) of the resulting shape raw data
    [DRres, slopeRes] = calc_res(data,L,201);
    [Xdes, THETAdes, DRdes] = calcLegendreGrid(cVect);
    xbound = 0.95;
    tbound = 0.95;
    valid = Xdes(1:200,:)<=xbound & THETAdes(1:200,:)<=tbound & ~isnan(slopeRes);
    slopeDes = diff(DRdes')./diff(Xdes')*2/L*180/pi*3600'; %arcsec
    RMSSlopeDes = sqrt(mean((slopeDes(valid)).^2));
    RMSSlopeRes = sqrt(mean((slopeRes(valid)).^2));
    RMSSlopeError = sqrt(mean((slopeDes(valid)-slopeRes(valid)).^2));
    HPDresidual = RMSSlopeError*4*sqrt(2)*0.68;
    HPD_reductionfactor = RMSSlopeError/RMSSlopeDes;
    izbounds = [1.05*min(min(DRdes*1e6)) 1.05*max(max(DRdes*1e6))];
    lbounds = [min(cVect) max(cVect)]*1.05;
    %Save workspace
    saveFileName = ['WolterR200M41N81_Smax' num2str(SmaxVect(j)) '.mat'];
    save(saveFileName);
    pause(1);
end
```

..... Repeat for R500 and R1000 .....

B.3 Matlab script: FindLeastSquaresFit.m *(abbreviated)*

```
% controlscript.m
% by Brandon Chalifoux
% Last updated: 8/10/2014
%
% Loads data containing influence functions, and solves constrained least-
% squares problem, for different integrated stress constraint magnitudes.
% Saves the results for plotting later.

SmaxVect = [50 100 150 200 250 300 400 500 1000];
%% R = 200 mm
cd('R200');
for idx = length(SmaxVect)-1:-1:1
   load(['WolterR200M41N81_Smax' num2str(SmaxVect(idx+1)) '.mat']);
   % Define legendres for desired shape change
   c = zeros(16,16);
   c(3,1) = 1.5e-6*0.2122;
   c(1,3) = -1e-6*0.2122;
   c(3,2) = 1e-6*0.2122;
   % Define boundary nodes (dirichlet boundary conditions)
   boundNodes = [0 0; 0 1; 1 0];
   cDesShape = defDesShape(c,boundNodes);
   cVect = reshape(cDesShape',[],1);
   % Calculate desired figure change
   drDes = calcLegendre(cVect,nodes_substrate);

   % solve unconstrained least squares problem for initial guess of constrained
   stressLS0 = stressLS;

   % Solve using constrained least squares
   Smax = SmaxVect(idx); % N/m
   ub = Smax*ones(M*N,1);
   lb = -ub;
   options = optimoptions(@lsqlin,'TolFun',1e-32,'MaxIter',1000);
   tic
   stressLS = lsqlin(drLibrary,drDes,[],[],[],[],lb,ub,stressLS0,options);
   disp(['t_lsqlin = ' num2str(toc)])

   % Input best fit stress to model to check results
   % Generate temperature batch file
   gen_tBatch(0, stressLS, nodes_implant, 'WolterOpticStress.in');

   % Run solution
   data = ADINA_run(nodes_substrate,fileName);

   % Calculate slope (dR/dx) of the resulting shape raw data
   [DRres, slopeRes] = calc_res(data,L,201);

   [Xdes, THETAdes, DRdes] = calcLegendreGrid(cVect);
   xbound = 0.95;
   tbound = 0.95;
```

```
    valid = Xdes(1:200,:)<=xbound & THETAdes(1:200,:)<=tbound & ~isnan(slopeRes);
    slopeDes = diff(DRdes')./diff(Xdes')*2/L*180/pi*3600'; %arcsec
    RMSSlopeDes = sqrt(mean((slopeDes(valid)).^2));
    RMSSlopeRes = sqrt(mean((slopeRes(valid)).^2));
    RMSSlopeError = sqrt(mean((slopeDes(valid)-slopeRes(valid)).^2));
    HPDresidual = RMSSlopeError*4*sqrt(2)*0.68;
    HPD_reductionfactor = RMSSlopeError/RMSSlopeDes;
    izbounds = [1.05*min(min(DRdes*1e6)) 1.05*max(max(DRdes*1e6))];
    lbounds = [min(cVect) max(cVect)]*1.05;
    %Save workspace
    saveFileName = ['WolterR200M41N81_Smax' num2str(SmaxVect(idx)) '_2.mat'];
    save(saveFileName);
    pause(1);
end
```

..... *Repeat for R500 and R1000* .....

Appendix C: LabView diagrams for *in-situ* curvature measurement device

This appendix shows only the front panels of the curvature measurement tool main control system. This system was developed in LabView, and unfortunately publishing the block diagram is difficult due to the size.

C.1 LabView main front panel: Initialization

The device is initialized by the user locating and marking the 5 centroids, which are displayed in the image pane (black in this image). The centroids are recorded and averaged over 1-100 images. The user may then begin recording data.

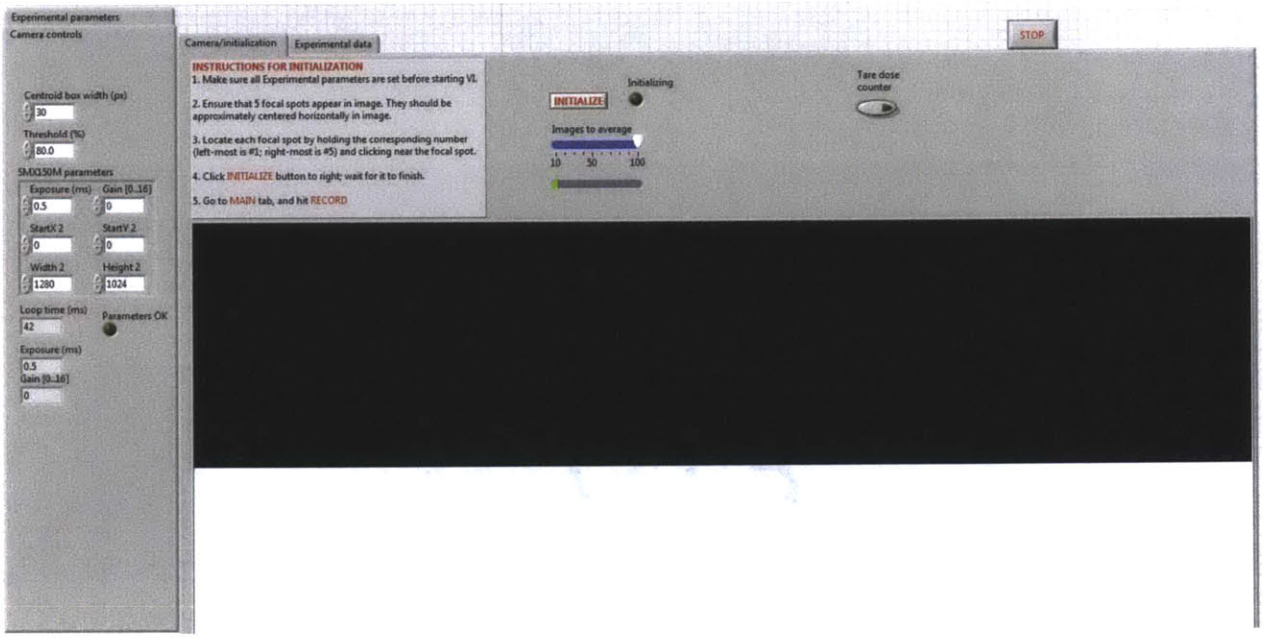

C.2 LabView main front panel: Experimental Data

The user records data from this panel, storing data in a .txt file. Raw images are recorded, and calculated parameters such as integrated stress, ion fluence, flux, etc. are recorded. The panel plots integrated stress as a function of time, for real-time debugging and monitoring.

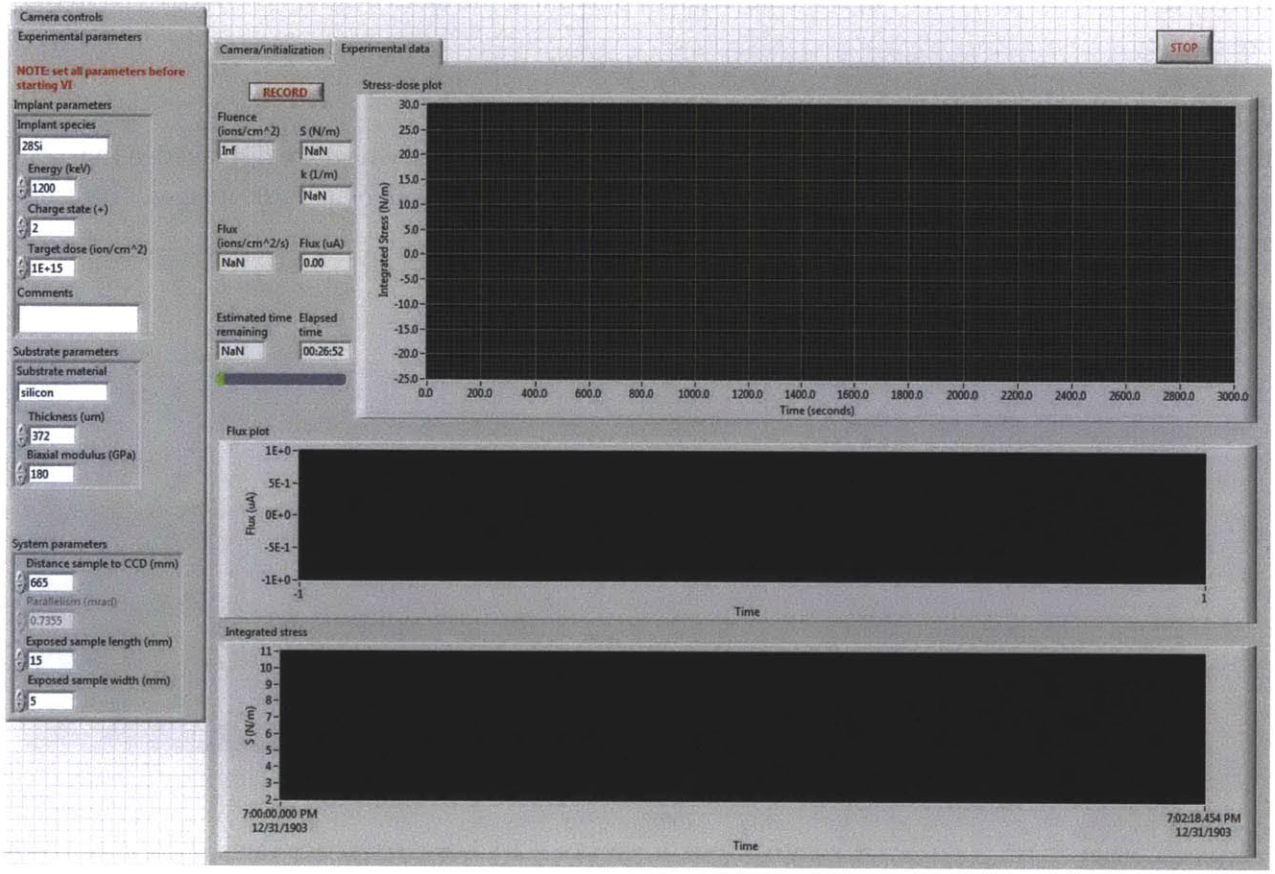

References

[1] S. L. O'Dell, R. J. Brissenden, W. N. Davis, R. F. Elsner, M. S. Elvis, M. D. Freeman, T. Gaetz, P. Gorenstein, M. V. Gubarev, D. Jerius, M. Juda, J. J. Kolodziejczak, S. S. Murray, R. Petre, W. Podgorski, B. D. Ramsey, P. B. Reid, T. Saha, D. A. Schwartz, S. Trolier-McKinstry, M. C. Weisskopf, R. H. T. Wilke, S. Wolk, and W. W. Zhang, "High-resolution x-ray telescopes," in *Proceedings of SPIE*, 2010, vol. 7803, p. 78030H.

[2] M. C. Weisskopf, H. D. Tananbaum, L. P. Van Speybroeck, and S. L. O'Dell, "Chandra X-ray Observatory (CXO): overview," in *Proceedings of SPIE*, 2000, vol. 4012, pp. 2–16.

[3] W. W. Zhang, M. P. Biskach, P. N. Blake, V. T. Bly, J. M. Carter, K. W. Chan, J. A. Gaskin, M. Hong, B. R. Hohl, W. D. Jones, J. J. Kolodziejczak, L. D. Kolos, J. R. Mazzarella, R. S. McClelland, K. P. McKeon, T. M. Miller, S. L. O'Dell, R. E. Riveros, T. T. Saha, M. J. Schofield, M. V. Sharpe, and H. C. Smith, "High resolution and high throughput x-ray optics for future astronomical missions," in *Proceedings of SPIE*, 2013, vol. 8861, p. 88610N.

[4] W. W. Zhang, M. P. Biskach, P. N. Blake, K. W. Chan, T. C. Evans, M. L. Hong, W. D. Jones, L. D. Kolos, J. M. Mazzarella, R. S. McClelland, S. L. O'Dell, T. T. Saha, and M. V. Sharpe, "Lightweight and high angular resolution x-ray optics for astronomical missions," in *Proceedings of SPIE*, 2011, vol. 8147, p. 81470K.

[5] S. Romaine, S. Basso, R. J. Bruni, W. Burkert, O. Citterio, G. Conti, D. Engelhaupt, M. J. Freyberg, M. Ghigo, P. Gorenstein, M. Gubarev, G. Hartner, F. Mazzoleni, S. O'Dell, G. Pareschi, B. D. Ramsey, C. Speegle, and D. Spiga, "Development of a prototype nickel optic for the Constellation-X hard x-ray telescope: IV," in *Proceedings of SPIE*, 2006, vol. 6266, p. 62661C.

[6] M. J. Collon, M. Ackermann, R. Günther, A. Chatbi, G. Vacanti, M. Vervest, A. Yanson, M. W. Beijersbergen, M. Bavdaz, E. Wille, J. Haneveld, M. Olde Riekerink, A. Koelewijn, C. van Baren, P. Müller, M. Krumrey, V. Burwitz, G. Sironi, and M. Ghigo, "Making the ATHENA optics using silicon pore optics," in *Proceedings of SPIE*, 2014, vol. 9144, p. 91442G.

[7] A. Winter, E. Breunig, P. Friedrich, and L. Proserpio, "Progress on indirect glass slumping for future x-ray telescope optics," in *Proceedings of SPIE*, 2014, vol. 9144, p. 91441C.

[8] R. E. Riveros, V. T. Bly, L. D. Kolos, K. P. McKeon, J. R. Mazzarella, T. M. Miller, and W. W. Zhang, "Fabrication of single crystal silicon mirror substrates for X-ray astronomical missions," in *Proceedings of SPIE*, 2014, vol. 9144, p. 914445.

[9] E. Sung, B. Chalifoux, M. L. Schattenburg, and R. K. Heilmann, "Non-touch thermal air-bearing shaping of x-ray telescope optics," in *Proceedings of SPIE*, 2013, vol. 8861, p. 88610R.

[10] B. Chalifoux, R. K. Heilmann, and M. L. Schattenburg, "Shaping of thin glass X-ray telescope mirrors using air bearing slumping and ion implantation," in *Proceedings of SPIE*, 2014, vol. 9144, p. 91444D.

[11] K. K. Madsen, F. A. Harrison, H. An, S. E. Boggs, F. E. Christensen, R. Cook, W. W. Craig, K. Forster, F. Fuerst, B. Grefenstette, C. J. Hailey, T. Kitaguchi, C. Markwardt, P. Mao, H. Miyasaka, V. R. Rana, D. K. Stern, W. W. Zhang, A. Zoglauer, D. Walton, and N. J. S. Westergaard, "The nuclear spectroscopic telescope array (NuSTAR) high-energy X-ray mission," in *Proceedings of SPIE*, 2014, vol. 9144, p. 91441P.

[12] S. Romaine, R. Bruni, P. Gorenstein, S. Park, P. Reid, B. Ramsey, and T. Kester, "Platinum as a release layer for thermally formed optics for IXO," in *Proceedings of SPIE*, 2010, vol. 7732, p. 77323T.

[13] W. W. Zhang, M. P. Biskach, V. T. Bly, J. M. Carter, K. W. Chan, J. A. Gaskin, M. Hong, B. R. Hohl, W. D. Jones, J. J. Kolodziejczak, L. D. Kolos, J. R. Mazzarella, R. S. McClelland, K. P. McKeon, T. M. Miller, S. L. O'Dell, R. E. Riveros, T. T. Saha, M. J. Schofield, M. V. Sharpe, and H. C. Smith,

"Affordable and lightweight high-resolution x-ray optics for astronomical missions," in *Proceedings of SPIE*, 2014, vol. 9144, p. 914415.
[14] M. Akilian, "Methods of improving the surface flatness of thin glass sheets and silicon wafers," Ph.D. Thesis, Massachusetts Institute of Technology, 2008.
[15] A. M. Z. Al Husseini, "Design and modeling of a third generation slumping tool for X-ray telescope mirrors," M.S. Thesis, Massachusetts Institute of Technology, 2011.
[16] E. Sung, "Horizontal non-contact slumping of flat glass," M.S. Thesis, Massachusetts Institute of Technology, 2013.
[17] K.-W. Chan, W. W. Zhang, D. Windt, M.-L. Hong, T. Saha, R. McClelland, M. Sharpe, and V. H. Dwivedi, "Reflective coating for lightweight x-ray optics," in *Proceedings of SPIE*, 2012, vol. 8443, p. 84433S.
[18] F. E. Christensen, A. C. Jakobsen, N. F. Brejnholt, K. K. Madsen, A. Hornstrup, N. J. Westergaard, J. Momberg, J. Koglin, A. M. Fabricant, M. Stern, W. W. Craig, M. J. Pivovaroff, and D. Windt, "Coatings for the NuSTAR mission," in *Proceedings of SPIE*, 2011, vol. 8147, p. 81470U.
[19] S. L. O'Dell, C. Atkins, T. W. Button, V. Cotroneo, W. N. Davis, P. Doel, C. H. Feldman, M. D. Freeman, M. V. Gubarev, J. J. Kolodziejczak, A. G. Michette, B. D. Ramsey, P. B. Reid, D. Rodriguez Sanmartin, T. T. Saha, D. A. Schwartz, S. Trolier-McKinstry, R. H. T. Wilke, R. Willingale, and W. W. Zhang, "Toward active x-ray telescopes," in *Proceedings of SPIE*, 2011, vol. 8147, p. 81471Q.
[20] M. Nastasi, J. Mayer, and J. K. Hirvonen, *Ion-Solid Interactions: Fundamentals and Applications*. Cambridge ; New York: Cambridge University Press, 2004.
[21] J. F. Ziegler, J. P. Biersack, and U. Littmark, *The stopping and range of ions in solids*. New York, 1985.
[22] C. R. Forest, C. R. Canizares, D. R. Neal, M. McGuirk, and M. L. Schattenburg, "Metrology of thin transparent optics using Shack-Hartmann wavefront sensing," *Opt. Eng.*, vol. 43, no. 3, pp. 742–753, 2004.
[23] M. Akilian, C. R. Forest, A. H. Slocum, D. L. Trumper, and M. L. Schattenburg, "Thin optic constraint," *Precis. Eng.*, vol. 31, no. 2, pp. 130–138, Apr. 2007.
[24] G. G. Stoney, "The Tension of Metallic Films Deposited by Electrolysis," *Proc. R. Soc. Lond. Ser. Contain. Pap. Math. Phys. Character*, vol. 82, no. 553, pp. 172–175, May 1909.
[25] M. . Hopcroft, W. D. Nix, and T. W. Kenny, "What is the Young's Modulus of Silicon?," *J. Microelectromechanical Syst.*, vol. 19, no. 2, pp. 229–238, Apr. 2010.
[26] "D263 Thin Glass, D 263 T speciality glass, D 263 T eco." [Online]. Available: http://www.pgo-online.com/intl/katalog/D263.html. [Accessed: 12-Aug-2014].
[27] "N-BK7, Optical glass | BK7 Bor-Crown glass." [Online]. Available: http://www.pgo-online.com/intl/katalog/BK7.html. [Accessed: 12-Aug-2014].
[28] P. A. Flinn, D. S. Gardner, and W. D. Nix, "Measurement and Interpretation of stress in aluminum-based metallization as a function of thermal history," *IEEE Trans. Electron Devices*, vol. 34, no. 3, pp. 689–699, 1987.
[29] C. A. Volkert, "Stress and plastic flow in silicon during amorphization by ion bombardment," *J. Appl. Phys.*, vol. 70, no. 7, pp. 3521–3527, Oct. 1991.
[30] J. A. Floro, E. Chason, and S. R. Lee, "Real Time Measurement of Epilayer Strain Using a Simplified Wafer Curvature Technique," *Mater. Res. Soc. Symp. Proc.*, vol. 406, pp. 491–496, 1996.
[31] J. Yuan, I. V. Verner, S. K. Maksimov, and J. W. Corbett, "Study of Amorphization Process in Silicon Irradiated by Different Ions Using In Situ Stress-Measurement and TEM Techniques," *Mater. Res. Soc. Symp. Proc.*, vol. 235, pp. 33–38, 1992.
[32] J. Yuan and J. W. Corbett, "Dose-rate dependence of the stress in Ar+ ion-implanted silicon," *Radiat. Eff. Defects Solids*, vol. 124, no. 3, pp. 265–270, 1992.

[33] J. Z. Yuan, R. Hartmann, I. V. Verner, and J. W. Corbett, "Temperature Dependence of Ion-Beam-Induced In-Plane Stress in Silicon," *Mater. Res. Soc. Symp. Proc.*, vol. 268, pp. 307–311, 1992.
[34] C. Fitz, W. Fukarek, A. Kolitsch, and W. Möller, "An instrument for in-situ stress measurement in thin films during growth," *Surf. Coat. Technol.*, vol. 128–129, pp. 474–478, Jun. 2000.
[35] E. P. EerNisse, "Sensitive technique for studying ion-implantation damage," *Appl. Phys. Lett.*, vol. 18, no. 12, pp. 581–583, 1971.
[36] B. Chalifoux, E. Sung, R. K. Heilmann, and M. L. Schattenburg, "High-precision figure correction of x-ray telescope optics using ion implantation," in *Proceedings of SPIE*, 2013, vol. 8861, p. 88610T.
[37] C. A. Volkert and A. Polman, "Radiation-enhanced plastic flow of covalent materials during ion irradiation," in *Mater. Res. Soc. Symp. Proc. 235*, 1992, pp. 3–14.
[38] F. F. Morehead and B. L. Crowder, "A model for the formation of amorphous Si by ion bombardment," *Radiat. Eff.*, vol. 6, no. 1, pp. 27–32, 1970.
[39] E. P. EerNisse, "Compaction of ion-implanted fused silica," *J. Appl. Phys.*, vol. 45, no. 1, pp. 167–174, Jan. 1974.
[40] E. Snoeks, T. Weber, A. Cacciato, and A. Polman, "MeV ion irradiation-induced creation and relaxation of mechanical stress in silica," *J. Appl. Phys.*, vol. 78, no. 7, pp. 4723–4732, Oct. 1995.
[41] H. Trinkaus, "Dynamics of viscoelastic flow in ion tracks: origin of plastic deformation of amorphous materials," *Nucl. Instrum. Methods Phys. Res. B*, vol. 146, no. 1–4, pp. 204–216, Dec. 1998.
[42] A. Ellison and I. A. Cornejo, "Glass Substrates for Liquid Crystal Displays," *Int. J. Appl. Glass Sci.*, vol. 1, no. 1, pp. 87–103, Mar. 2010.
[43] G. W. Arnold, "Ion implantation effects in alkali-borosilicate glasses," *Radiat. Eff.*, vol. 98, no. 1–4, pp. 55–61, 1986.
[44] T. L. Aldcroft, D. A. Schwartz, P. B. Reid, V. Cotroneo, and W. N. Davis, "Simulating correction of adjustable optics for an x-ray telescope," in *Proceedings of SPIE*, 2012, vol. 8503, p. 85030F–85030F.
[45] J. D. Plummer, *Silicon VLSI Technology: Fundamentals, Practice, and Modeling*, 1 edition. Upper Saddle River, NJ: Prentice Hall, 2000.
[46] K. Oyoshi, S. Hishita, K. Wada, S. Suehara, and T. Aizawa, "Roughness study of ion-irradiated silica glass surface," *Appl. Surf. Sci.*, vol. 100–101, pp. 374–377, Jul. 1996.
[47] T. M. Mayer, E. Chason, and A. J. Howard, "Roughening instability and ion-induced viscous relaxation of SiO2 surfaces," *J. Appl. Phys.*, vol. 76, no. 3, pp. 1633–1643, Aug. 1994.
[48] G. H. Bu-Abbud, D. L. Mathine, P. Snyder, J. A. Woollam, D. Poker, J. Bennett, D. Ingram, and P. P. Pronko, "Roughness studies of ion beam processed molybdenum surfaces," *J. Appl. Phys.*, vol. 59, no. 1, pp. 257–262, Jan. 1986.
[49] X. Hu, D. G. Cahill, and R. S. Averback, "Nanoscale pattern formation in Pt thin films due to ion-beam-induced dewetting," *Appl. Phys. Lett.*, vol. 76, no. 22, pp. 3215–3217, May 2000.
[50] R. C. Welch, J. R. Smith, M. Potuzak, X. Guo, B. F. Bowden, T. J. Kiczenski, D. C. Allan, E. A. King, A. J. Ellison, and J. C. Mauro, "Dynamics of Glass Relaxation at Room Temperature," *Phys. Rev. Lett.*, vol. 110, p. 265901, 2013.
[51] K.-W. Chan, W. W. Zhang, M. V. Sharpe, J. R. Mazzarella, R. S. McClelland, M. P. Biskach, T. T. Saha, L. D. Kolos, and M.-L. Hong, "Preserving accurate figures in coating and bonding mirrors for lightweight x-ray telescopes," in *Proceedings of SPIE*, 2014, vol. 9144, p. 914440.
[52] S. Rekhson, "Models of relaxation in glass," *J. Non-Cryst. Solids*, vol. 95–96, Part 1, pp. 131–147, Dec. 1987.
[53] O. S. Narayanaswamy, "Stress and Structural Relaxation in Tempering Glass," *J. Am. Ceram. Soc.*, vol. 61, no. 3–4, pp. 146–152, 1978.
[54] S. Timoshenko, *Theory Of Plates & Shells*. Tata Mcgraw Hill.

[55] S. T. Smith, *Foundations of Ultra-Precision Mechanism Design*, Reprint edition. Yverdon, Switzerland: CRC Press, 1994.
[56] P. Glenn, "Set Of Orthonormal Surface Error Descriptors For Near-Cylindrical Optics," *Opt. Eng.*, vol. 23, no. 4, pp. 234384–234384–, 1984.
[57] W. A. Podgorski, J. Bookbinder, D. A. Content, W. N. Davis, M. D. Freeman, J. H. Hair, S. M. Owens, R. Petre, P. Reid, T. T. Saha, J. W. Stewart, and W. W. Zhang, "Constellation-X spectroscopy x-ray telescope optical assembly pathfinder image error budget and performance prediction," in *Proceedings of SPIE*, 2004, vol. 5168, pp. 318–333.